A Study of the Internal Proper Motions of 6.7 GHz Methanol Masers Associated with High-mass Star Forming Regions

by

Koichiro Sugiyama

Submitted to Yamaguchi University

For the Degree of Doctor of Philosophy

Supervisor : Professor Kenta Fujisawa

Graduate School of Science Engineering

Yamaguchi University

March 2011

Abstract

High-mass stars (eight times or more heavier than the solar mass) have key roles to contribute evolution and energetics of interstellar mediums. The process of high-mass star formation, however, has been poorly understood since observations for high-mass star forming regions (HMSFRs) are actually challenging due to their far distances, heavy obscuration by dense dust around the young stellar objects (YSOs), and rapidity of evolution. Interstellar maser emission detected at around YSOs has become a useful tool to study the process of star formation. Most of the maser emission appear as compact regions "spots" with sizes of the order of several astronomical unit (AU). Thus, the maser spots can be observed using Very Long Baseline Interferometer (VLBI) technique, which provides an ultra-high spatial resolution of a few milliarcsecond scales, consequently the internal proper motion of spots. Study of the internal proper motions of individual maser spots is the only tool we have to obtain information on the dynamical motions in star-forming regions on a velocity scale of a few km sec^{-1}. Of the various interstellar masers, especially the methanol maser transition at 6.7 GHz has a number of advantages for investigations of HMSFRs as follows: 1) has been detected in only HMSFRs; 2) has a long lifetime and is relatively stable; 3) often appears at an early evolutionary phase before the formation of an ultra-compact (UC) HII region. Therefore, internal proper motion measurement of the methanol masers can provide unique information relating to the processes of high-mass star formation.

We have conducted multi-epoch VLBI observations of the 6.7 GHz methanol masers in three high-mass star forming regions Cepehus A (Cep A), W75 North (W75 N), and Onsala 1 (ON 1) using the Japanese VLBI Network (JVN) over two years. The obtained spatial distributions of the maser spots extended with a scale of 1000-2000 AU, and the morphology was classified into two types: 1) an arched or an elliptical structure in Cep A and W75 N; 2) an widely separated structure in the ON 1.

We detected internal proper motions of the maser spots of all three sources. For Cep A, the detected motions are along the elliptical structure, which was roughly perpendicular to a radio continuum jet. We estimated a rotational velocity of 1.0 ± 1.0 km s^{-1} with an infall velocity of 2.5 ± 1.1 km s^{-1} by applying a simple rotating with expansion/infall disk model. This is the first detection of infall motions around a high-mass YSO. The infalling pressure can exceed the radiation pressure if the gas density at the masing site is larger than 10^7 cm^{-3}. For W75 N, a linear radial velocity gradient was seen along the arched structure, which fit a simple rotational disk. From the internal proper motions of the W75 N, a simple rotational velocity of 1.3 ± 0.7 km s^{-1} without expansion/infall by using the same disk model in the case of the Cep A methanol masers was derived. The internal proper motions of the ON 1 methanol maser spots showed outward motions in roughly the north-south direction with a relative velocity $\sim$5 km s^{-1}. Their motion is similar to that of hydroxyl masers in ON 1 as well as the spatial distributions. The both masers seem to trace the expanding UC HII region. The motion of the methanol maser, on the other hand, can be explained as that the methanol masers are associated with a molecular outflow observed by multi molecular lines, because the direction and velocity of the methanol masers were similar to those of the molecular lines.

The difference of the internal proper motions detected in the 6.7 GHz methanol maser and the sites associated with this maser for each source could be related to the evolutionary phase of high-mass YSOs. We discussed the relation on the basis of superposition of the maser on radio continuum emissions: (i) the elliptical structure and the infall motions like the Cep A methanol masers are observed at the earliest phase, and are embedded in the dense gas and dust, (ii) the same structure but the simple rotational motions like the W75 N methanol masers are observed at the second phase at which UC Hɪɪ region was not yet formed, (iii) the separated structure and the outward motions like the ON 1 methanol masers are observed at the evolved phase, at which UC Hɪɪ region has been formed and the disk might be already destroyed. These results indicate that the 6.7 GHz methanol masers trace the two or three evolutionary phases of high-mass YSOs, and the proper motions depend on the evolutionary phase.

Contents

Chapter 1

Introduction

1.1 High-mass Star Formation

Star-forming regions are generally divided into two classes in terms of a central mass of the formed star. The star showing a central mass over eight times heavier than the solar mass ($M_\odot \sim 2 \times 10^{30}$ kg) is named as "High-Mass Star" (HMS), while the one showing the central mass lighter than the border mass ($< 8M_\odot$) is named as "Low-Intermediate Mass Star" (LIMS). LIMSs occupy at the most of the mass of our Galaxy, but the major contributor to the luminosity and the metallicity of the Galaxy is not LIMSs but HMSs. HMSs also have a significant role to make stars of next generation. An expanding HII region, which is an ionization medium formed by strong UV radiations from HMSs at the main-sequence phase, is a trigger of new star formation. In the last stage of HMSs after the red (super-)giant star, it pushes and compresses gases around the HMSs by the supernova explosion. The compressed gases forms stars. These processes are called as feedback loop. Since HMSs have key roles to contribute an evolution of interstellar mediums (ISMs), investigations about HMSs are necessary for getting to know the evolution of not only our Galaxy but also extra galaxies (summarized in [194]Zinnecker & Yorke 2007, and references therein).

1.1.1 Possible Scenarios of High-mass Star Formation

Since high-mass star formation affects star-forming rate, number densities of low-mass stars, and a birth of new stars at stage of next generation, processes of high-mass star formation (HMSF) should be well understood. But actually the processes are poorly understood.

About a process of a low-mass star is well known as a accretion through a rotating disk, whose theory was established by [150]Shu & Adams (1987). In the beginning of the star formation, a dense ($\geq 10^9$ cm^{-3}) core is formed at center of a molecular could, which is called as a molecular cloud core. The core grows through taking gases surrounding the core by self gravitation, and then become to be a young stellar object (YSO), which is bright by a potentiall energy from an accretion of interstellar mattars. Since the accreting gases have an angular momentum, the gases accrete to a central YSO not directly straight but with a rotation making an accretion disk. An accretion rate is generally thought to be 10^{-6}-10^{-5} $M_\odot$ yr^{-1}. In the rotating accretion disk, magnetic fields are frozen in the direction perpendicular to the disk plane, and then the magnetic fields are twisted by the rotation of the disk. A portion of the gases are ejected along the direction of the twisted magnetic fields, which are called as a bipolar jet or an outflow. At the same time, the gas flows bring an extra angular momentum, which is difficult to maintain by self gravitation, out of the YSO systems. The central YSO contracts by self gravitation, and then the potential energy is converted to a thermal energy to make the YSO heater. At the end of the formation, nuclear reactions switch on in the center of the YSO, and the star reaches the zero-age main sequence (ZAMS).

However, above accretion model is difficult to explain a high-mass star formation with following reasons. The Kelvin-Helmholts time scale $T_{\rm KH}$ [yr], which indicates an evolutionary time scale of inside structure in a HMS, is described as follows:

$$T_{\rm KH} \simeq \frac{GM_*^2}{R_* L_*} \simeq 3 \times 10^7 \left(\frac{M_*}{M_\odot}\right)^2 \left(\frac{L_*}{L_\odot}\right)^{-1} \left(\frac{R_*}{R_\odot}\right)^{-1} \qquad (1\text{-}1)$$

where G is the gravitational constant, M_*, L_*, R_* are the mass, luminosity, and radius of gases forming a star, respectively. Also, $M_\odot, L_\odot, R_\odot$ are the mass ($= 1.9891 \times 10^{30}$ kg), luminosity ($= 3.85 \times 10^{26}$ W), and radius ($= 6.960 \times 10^8$ m) of the sun, respectively. Assumed that a mass of the star is over 10 $M_\odot$, $T_{\rm KH}$ become to be less than 4×10^4 yr, which is from tenth to handredth compared to that of the LIMSs. On the other hand, the free-fall time scale $T_{\rm ff}$ [yr], which indicates a time scale of gravitational contractions, is described as follows:

$$T_{\rm ff} = \sqrt{\frac{\pi}{G\rho_0}} \simeq 1.1 \times 10^8 \left(\frac{n_{\rm H_2}}{\rm cm^{-3}} \right)^{-1/2} \tag{1-2}$$

where ρ_0 and $n_{\rm H_2}$ is the gas density and the hydorogen-molecule number density of a molecular cloud core, respectively. Using the typical number densities 3×10^4-10^7 cm^{-3} in high-mass star forming regions (HMSFRs: e.g., [173]Turner 1984; [46]Downes 1987), $T_{\rm ff}$ become to be 3×10^4-6×10^5 yr. As a result of above estimations, it leads to be $T_{\rm ff} > T_{\rm KH}$. This result suggests that mass accretions should still continue after reaching ZAMS in HMSFRs. However, under a condition of $L_*/M_* \geq 700\ L_\odot\ M_\odot^{-1}$, a powerful stellar radiation is predicted to inhibit accretion and thus limit the growth of their mass ([151]Shu et al. 1987). This condition appears with a central mass $M \geq 7\ M_\odot$. Therefore, a high-mass star having a central mass $M_* \geq 8\ M_\odot$ is difficult to make through the traditional accretion model as mentioned above.

In the recent decade, theoretical models for the processes of high-mass star formation have been established as mainly possible two scenarios: 1) the traditional accretion model but its accretion rate sufficiently large to exceed radiation pressure, that is $10^{-3}\ M_\odot$ yr^{-1} (two or three magnitudes larger than that for low-mass stars); 2) the merging of several low-mass stars that had been already formed. In the first scenario, the large accretion rate could be achieved under interstellar conditions with turbulence in high-mass molecular clouds (e.g, [107][108]McKee & Tan 2002, 2003; [93]Krumholz et al. 2007). Also, a rapid rotation may sufficiently reduce the luminosity of the star in the equatorial plane, which is called as mid-plane ([191]Yorke & Sonnhalter 2002). On the other hand, in the second scenario most of high-mass stars are well known to be found in stellar clusters ([31]Clarke, Bonnell & Hillenbrand 2000; [98]Lada & Lada 2003). For forming high-mass stars through the merging of low-mass stars, minimum stellar densities of $\geq 10^4$ star pc^{-3} (1 pc = 3.26 ly) are needed in individual HMSFR (Bonnell et al. 1998, 2004). Such high densities are typical only of the central regions of large clusters such as the Orion Nebula Cluster.

Observations at optical wavelength are necessary to verify which theories are correct for the processes of high-mass star formations. But observations for HMSFRs are actually challenging due to many reasons as follows. Firstly, all of HMSFRs except for a few sources locate at distant places further than 1 kpc. High spatial resolutions better than 1 arcsec therefore are required to observe individual locations of high-mass star formation, which are typically ~1000 astronomical unit (AU: ~ 1.5×10^{11} m). Secondary, since high-mass YSOs spend in a deeply embedded molecular cloud during most of a forming period, there are heavy obscurations by dense dust around the YSOs. Finally, the lifetime of high-mass stars is short of 10^6-10^7 yr, and then observable sources are much lower than those in the case of low-mass stars.

For a recent half decade, there has been several results toward HMSFRs with sub-arcsecond spatial resolutions at infrared and radio wavelengths, which are relatively lower extiction and obscurations than that at optical wavelength. About the accreting through the rotating disk scenario, molecular line observations at around 1 mm wavelength mainly provide information for existences of the rotating disks (e.g., [29]Cesaroni et al. 2005; [129]Patel et al. 2005; [13]Beltran et al. 2006). For example, [13]Beltran et al. (2006) observed a HMSFR G24.78+0.08, where is at a distance of 7.7 kpc, using the IRAM Plateau de Bure Interferometer, and showed a spatial distribution of the $\rm CH_3CN$ line emissions at 1.4 mm wavelength, as shown in figure 1-1 (left-panel). The spatial resolution of the observation achieved sub-arcsecond of $1.2'' \times 0.5''$ at position angle (PA) of $-174°$. The overall distribution was extended to the direction perpendicular to the bipolar outflow axis observed by ^{13}CO line emissions. Also, the radial velocity gradient could be seen

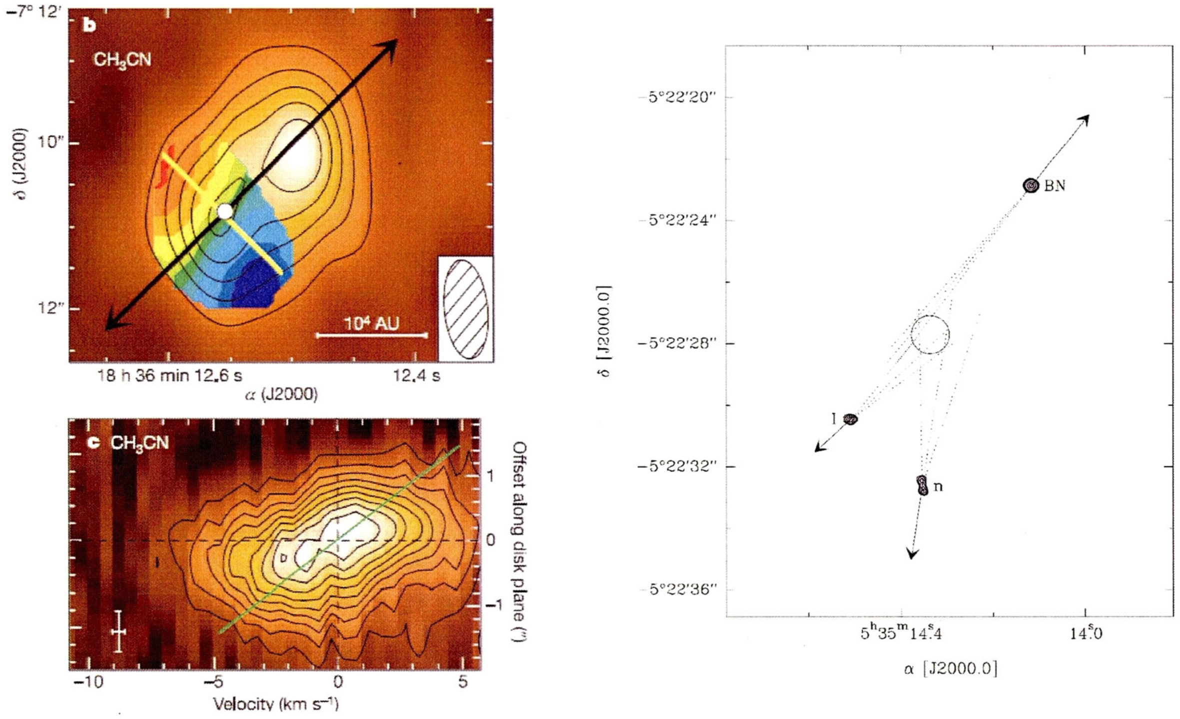

Figure 1-1: Left-panel: CH$_3$CH line emissions in HMSFR G24.78+0.08 ([13]Beltran et al. 2006). Upper:Spatial distribution with contours and colors, which indicate intensities and radial velocities, respectively. A synthesized beam is described at the bottom right. The black arrows outline the direction of a bipolar outflow, and a predicted disk plane is denoted by the yellow line. The white filled circle marks the position of the hyper-compact HII region; Lower:Position-Velocity diagram. The positional cut is made along the plane of the disk, position angle = −135° described using the yellow line in left-panel. The radial velocity gradient is indicated by the green line, which could be thought to correspond to a rotation. Right-panel: Absolute proper motions of BN, source I, and source n objects in HMSFR Orion KL ([75]Gomez et al. 2005). Arrows show the direction, and their lengths are propotional to the tangential velocities. The dotted lines encompass their past positions About 500 years ago, all three sources must have been located in the small circle predicted that the merging was occured.

along the extended structure, which possibly indicates a rotation of an accretion disk, although the size of this molecular disk was ∼ 10 times larger than the maximum size of disks around low-mass YSOs. Recently, interferometric observations at near infrared wavelengths (NIR) using the Very Large Telescope Interferometer (VLTI) provided an high-spatial resolution image with AU scale of hot material in HMSFR IRAS 13481−6124, and showed an elongated structure with a size $\sim 13 \times 19$ AU with PA of 120° ([92]Kraus et al. 2010). This structure was perpendicular to the large-scale outflow axis (PA∼ 30°), which is suggesting that the VLTI image could be a compact dusty disk with dust temparatures ranging from 1000 to 2000 K. That outflow was well collimated (∼ 6°) that was consistent with other interferometric results of radio molecular lines at the earliest evolutionary phase of HMSF, and it is probably though to be due to interactions with disk winds ([14]Beuther & Shepherd 2005, and references therein).

On the other hand, about the merging scenario there are a few indirectly results in the Orion Trapezium and Becklin-Neugebauer/Kleinman-Low (BN/KL) regions using centimeter radio continuum emissions ([75]Gomez et al. 2005; [139]Rodriguez et al. 2005). They used the Very Large Array (VLA) archival data achiving high-spatial resolutions at these wavelengths, which correspond to ones higher than 300 milliarcsecond (mas), and then tried to measure absolute proper motions over a period of 15 years for high-mass stars BN, source I, and source n radio continuum objects. All three objects appear to be moving away from a common point where they must all have been located about 500 years ago, as shown in figure 1-1 (right-panel). They thought that this result suggested that all three objects were originally part of a multiple high-mass stellar system that recently disintegrated as a result of a close dynamical interaction. But there are no observational evidences in detecting actual sites of merging between multiple low-mass stars.

As discussed above, the first scenario, that is the accretion through the rotating disk around high-mass YSOs, recently has become to be popular on the basis of the molecular line observations at radio wavelengths. However, it is so difficult to directly detect the rotation and infall caused by accreting matters as internal proper motions, because the dynamical motions with the rotation and infall are expected as $\sim$10 km s^{-1} at a maximum, which corresponds to internal proper motions of $\sim$2 milliarcsecond per year (mas yr^{-1}) at a typical distance to HMSFRs of 1 kpc. It is impossible to detect the proper motions using the interferometric technique as introduced above, whose spatial resolutions are a few hundred mas in well situations and wavelengths.

1.1.2 Maser Emissions in High-mass Star Forming Regions

The microwave amplification by stimulated emission of radiation (maser, refered in appedix A) is detected at around both YSOs and evolved stars such like asymptotic giant branch (AGB) stars. This interstellar maser emission, e.g., from H_2O and CH_3OH molecules, has become a useful tool to study high-mass star formation. Most of the maser emission appear as compact regions "spots" with sizes of the order of several AU (e.g., [109]Menten 1991b, and refered in chapter 2). Thus, the maser spots can be observed using Very Long Baseline Interferometer (VLBI) technique, which provides an ultra-high spatial resolution of a few milliarcsecond (mas) scales. Observations of the maser emissions showing compact sizes using VLBI arrays make high-mass YSOs at distances further than 1 kpc possible to be divided into individual objects. The maser emission also provides velocity information both to the line of sight cause by Doppler effects and on the sky plane observed as proper motions.

The water and hydroxyl masers are detected not only HMSFRs but also LMSFRs ([187]Wilson & Barrett 1972). This makes selectively observations of HMSFRs difficulty. Most of the water maser detected in SFRs are well known by internal proper motion studies to be associated with shock regions formed by interactions between interstellar mediums and an outflow ejected from a central star (e.g., [68][69]Genzel et al. 1981a, b). This maser therefore is unsuitable for measuring internal proper motions of a rotation and an infall that could be observed on the accretion disk. Most of the hydroxyl masers detected in HMSFRs are well known by internal motion studies to be associated with expanding HII regions (e.g, [16]Bloemhof et al. 1992; [59]Fish & Reid 2007). This maser is also unsuitable for measuring internal motions on the accretion disk due to the associated site as well as detected at a well-evolved phase.

The methanol maser emission, especially the one detectable at 6.7 GHz frequency band, has been detected only in HMSFRs so far ([118]Minier et al. 2003; [190]Xu et al. 2008). This character makes the selectively observations of HMSFRs so easy. This maser has a long lifetime at least four years and is relatively stable (e.g., [72]Goedhart et al. 2004; [52]Ellingsen 2007). Thus, it's easy to conduct multi-epoch VLBI observations with more than one year gaps. Understanting associating sites of the methanol maser especially at 6.7 GHz has a key role to find out the process of high-mass star formation. However, the associating site of this maser is unclear mainly whether the maser emissions trace a disk or an outflow. A main reason of the unclear is that there are only a few sources which could detect internal proper motions for the 6.7 GHz methanol maser ([141]Rygl et al. 2010; [142][143]Sanna et al. 2010a, b).

1.2 6.7 GHz Methanol Maser

1.2.1 Methanol Masers

The maser emission from interstella methanol molecules was detected at 25 GHz in the well-known HMSFRs Orion-KL, which is the closest HMSFRs ([4]Barrett et al. 1971). There are many methanol transition at various frequencies, as described in table 1-1. These methanol transitions have been classified into two classes on the basis of associated regions ([9]Batrla et al. 1987; [110]Menten 1991a): in some sources, maser emissions were projected against the hydroxyl maser, an infrared (IR) source, and an ultra-compact (UC) HII region; in other sources, maser emissions were not overlaied on the other emissions. This was an external manifestation of different excitation mechanisms: collisional and radiative excitation operates Class I and Class II maser emission, respectively (e.g., [35]Cragg et al. 1992; [155]Sobolev et al. 1997). Especially, the spot size and the associating sites of the 6.7 GHz methanol maser were described in detail in section 1.2.2, 1.2.4, and chapter 2. The characteristics of both Class I and II are summarized in table 1-2. [110]Menten (1991a) mentioned that none of the transitions that is masing in Class I sources is masing in Class II sources and vice versa. But in the recent half decade, the classification has become to be ambiguity. [183]Voronkov et al. (2005) detected the Class II methanol maser at 6.7 GHz in Orion Molecular Clound 1, in which the Class I methanol maser at 25.0 and 95.2 GHz had been already detected. [50]Ellingsen (2005) detected the Class I methanol maser at 95.2 GHz toward 25/62 the 6.7 GHz methanol maser sources classified to Class II (detection rate ~40%). [39]Cyganowski et al. (2009) conducted imaging observations of the 6.7 GHz (Class II) and the 44.1 GHz (Class I) methanol masers toward Extended Green Objects (EGOs: [38]Cyganowski et al. 2008), which have been thought to be active outflows ejected from high-mass YSOs at an earlier evolutionary phase. As a result of the observations for 22 EGO sources, the detection rate of both masers was more than 70% (16/22), although extended scales of spatial distribution were quite different that the spatial scale of the Class I maser were 10 times or more wider than that of the Class II maser, as shown in figure 1-2.

The Class II methanol masers are represented at 6.7 and 12.2 GHz frequencies. The 6.7 GHz methanol maser is emitted in the transition of $5_1 \rightarrow 6_0 A^+$, which means the rotational transition from $(J, K) = (5, 1)$ to $(J, K) = (6, 0)$ around A^+ rotational axis (refered in figure 1-4). The rest frequency is known as 6668.5192 ±0.0008 MHz ([18]Breckenridge & Kukolich 1995). The interstellar methanol maser emissions at 6.7 GHz were discoverd by [109]Menten (1991b) in 1991, and then the maser emissions have been detected by target surveys toward hydroxyl maser sources ([103][104]MacLeod et al. 1992a, b; [67]Gaylard & MacLeod 1993; [26]Caswell et al. 1995a) and infrared astronomical satellite (IRAS) sources ([145]Schutte et al. 1993; [176][177]van der Walt et al. 1995, 1996; [185]Walsh et al. 1997; [106]MacLeod et al. 1998a; [153]Slysh et al. 1999; [165]Szymczak et al. 2000), and unbiased surveys concentrated to the Galactic plane (latitude $| b | \leq 1.0°$: [23][24]Caswell 1996a, b; [53]Ellingsen et al. 1996; [131]Pestalozzi

Table 1-1: Methanol maser transition at various frequencies (refered from [124]Müller et al. 2004).

Class	Frequency (GHz)
I	9.9, 25.0, 25.8, 26.8, 27.4, 28.1, 28.9, 29.6, 30.3, 36.1, 44.1, 84.5, 95.2, 104.3, 132.9, 146.6, 229.8
II	**6.7**, 12.2, 20.0, 23.1, 29.0, 37.7, 38.2, 38.4, 86.6, 86.9 107.0, 108.8, 156.6, 156.8, 157.2

Table 1-2: Characteristics of Class I and II methanol masers.

Parameter	Class I	Class II
HII, IR, hydroxyl maser	non-association	association (but distant from UC HII region of 1–5 arcsec offset)[8]
Associating site	edge of outflow[1,4]	disk or outflow
Excitation mechanism	collision[2]	IR radiation[5,10,11,12]
Emission (spot) size	a few hundred AU[6,7]	several AU[3,9,13]
Brightness temperature	10^6-10^8 K	$>10^{10}$ K

References — (1) Plambeck & Menten (1990); (2) Cragg et al. (1992); (3) Menten et al. (1992); (4) Liechti & Wilson (1996) (5) Sobolev et al. (1997); (6) Kogan & Slysh (1998); (7) Lonsdale et al. (1998); (8) Walsh et al. (1998) (9) Moscadelli et al. (1999); (10) Cragg et al. (2001); (11) Sutton et al. (2001); (12) Cragg et al. (2005); (13) Sugiyama et al. (2008).

et al. 2002; [166]Szymczak et al. 2002). [130]Pestalozzi et al. (2005) complied 519 methanol maser sources at 6.7 GHz in our Galaxy as the published catalog. In the catalog, it was described such like figure 1-3 that most of the 6.7 GHz methanol maser sources were distributed on the galactic plane. Recently, a high-sensitivity unbiased survey (an rms noise level of ~ 85 mJy, $35.2° \leq l \leq 53.7°$, $\mid b \mid \leq 0.41°$) using the Arecibo 305-m radio telescope detected 48 new methanol sources ([128]Pandian et al. 2007) The methanol multibeam survey (MMB) using 7-beam system proving wide field installed the Parkes 64-m radio telescope detected more than 300 new sources in southern hemisphere (e.g., [32]Cohen et al. 2007). A portion of the MMB survey results has been compiled in [27]Caswell et al. (2010) and [77]Green et al. (2010) ($345° \leq l \leq 20°$, $\mid b \mid \leq 2°$). The number of the 6.7 GHz methanol maser sources is expected to be more than 1000 sources in our Galaxy.

1.2.2 Observational Characteristics

The 6.7 GHz methanol maser is the strongest emission in various methanol transitions, and the secondest bright emission in the masers including the water maser. The methanol maser at 6.7 GHz is typically 10 times brighter than the maser at 12.2 GHz ([25]Caswell et al. 1995b). The strongest source in the 6.7 GHz methanol maser emissions showes the luminosity $\sim 5.0 \times 10^{-4}$ $L_\odot$ ($L_\odot$: the solar luminosity $\simeq 3.85 \times 10^{26}$ W). The spot size of this maser in most of methanol sources is known to be compact with sizes of several AU ([111]Menten et al. 1992; [119]Moscadelli et al. 1999; [160]Sugiyama et al. 2008a, in detail discussed in chapter 2), and then its characteristic makes brightness temparature much higher, although in some sources the methanol maser emissions at 12.2 GHz had structures not only compact but also extended named as the core/halo structure ([116]Minier et al. 2002). These characteristics suggest that this maser is suitable to observe using the VLBI technique, therefore its spatial distribution can be gotten to know with an ultra-high spatial resolution of a few mas scales.

1.2.3 Evolutionary Phase of High-mass YSOs

The 6.7 GHz methanol masers have been detected only in HMSFRs, that is no detection toward any LIMSFRs and evolved stars ([118]Minier et al. 2003; [190]Xu et al. 2008). In an evolutionary phase of high-mass YSOs, interferometric observations with the Australian Telescope Compact Array (ATCA) provided clear pictures ([135]Phillips

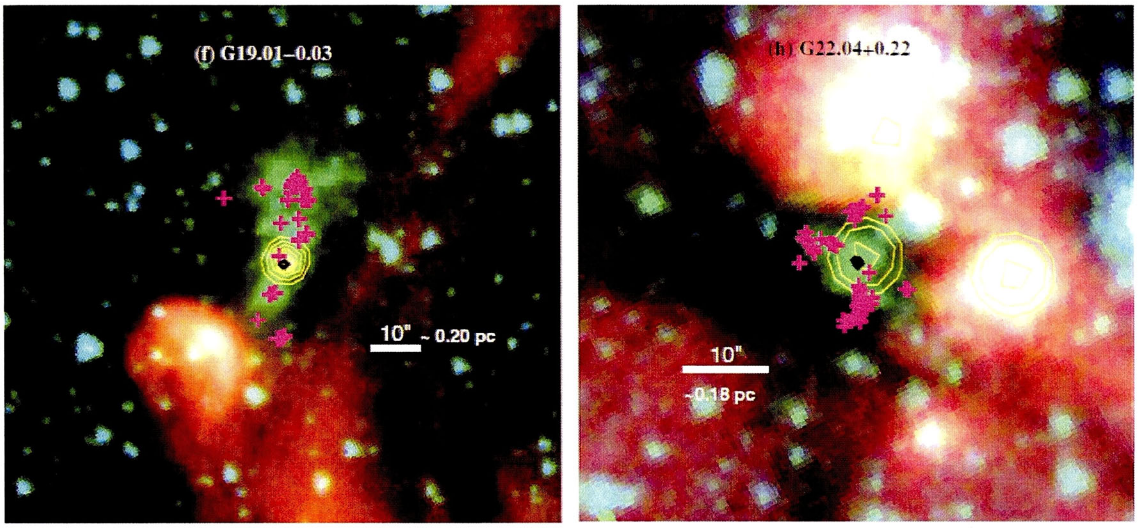

Figure 1-2: Spatial distribution of the 6.7 GHz (diamonds) and 44.1 GHz (magenta crosses) methanol maser superposed on the EGOs (extraced from [39]Cyganowski et al. 2009). The red, green, and blue colors show the mid-IR images 8.0, 4.5, and 3.6 μm, respectively, obtained with the Spitzer Space Telescope's Infrared Array Camera (IRAC). Yellow contours show the 24 μm emissions observed with mid-IR point source galactic plane survey (MIPSGAL).

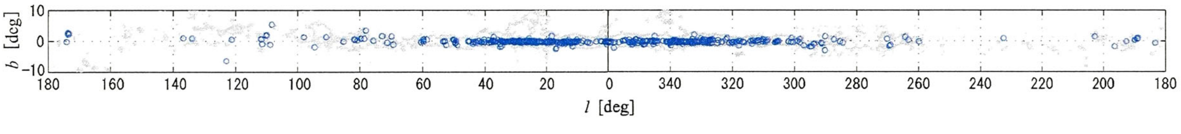

Figure 1-3: Detected 6.7 GHz methanol maser sources (blue circles) in our Galaxy (extracted from [130]Pestalozzi et al. 2005). The gray contours are the 1% CO emission from [40]Dame et al. (1987).

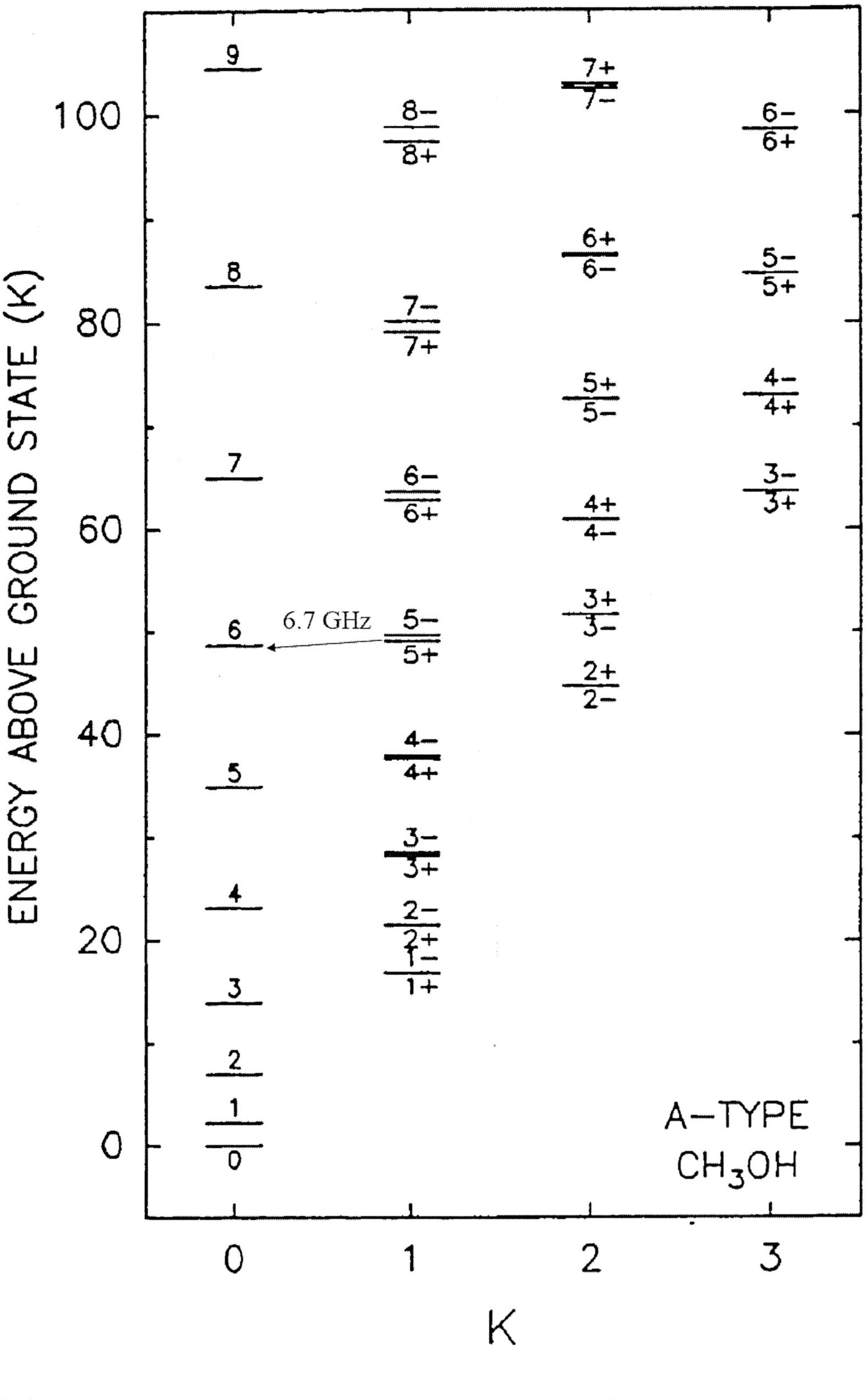

Figure 1-4: The energy level of the methanol transition around A^+ rotational axis (extracted from [110]Menten et al. 1991a). A vertical axis is rotational quantum number J, and a horizontal axis is projected component K to the A axis. An Arrow shows the transition of $5_1 \rightarrow 6_0A^+$ at 6.7 GHz.

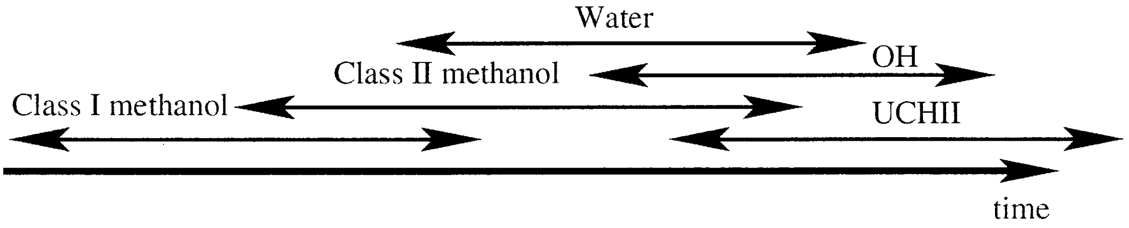

Figure 1-5: A scheme of an evolutionary phase of high-mass YSOs related to each maser (extracted from [54]Ellingsen et al. 2007).

et al. 1998; [184]Walsh et al. 1998). They showed spatial relations between the methanol masers and radio continuum emissions, which correspond to free-free emissions from UC Hii regions, and most of the methanol emissions were not associated with observable continuum emissions. These results suggested that the methanol maser is observable before the UC Hii region phase and is probably destroyed as the UC Hii region develops. An UC Hii region is produced by a well-evolved state embedded in the region, and is defined as a extended size less than 0.1 pc ([96]Kurtz & Franco 2002). The 6.7 GHz methanol masers are well known to be projected to dense hot molecular cores (HMCs) and infrared dark clouds (IRDC), which are tracers of early high-mass YSOs ([117]Minier et al. 2001a; [51]Ellingsen 2006). On the other hand, the water masers in some sources were associated with mid-IR sources, which were a relatively evolved phase ([19]Breen et al. 2007). [15]Beuther et al. (2002) superposed the distributions of the 6.7 GHz methanol masers on those of the 22.2 GHz water masers, the millimeter dust continuum, the centimeter continuum, and mid-infrared sources in massive star-forming regions with absolute positional accuracies of ∼1 ″. The results supported the suggestion that the methanol masers appear at an earlier phase than the water masers. The 6.7 GHz methanol maser often appears earlier phase than the water maser in the evolution of a high-mass YSO (summarized in [54]Ellingsen et al. (2007) and in figure 1-5), although [138]Reid (2007) suggested that the water masers trace an earlier phase than the methanol masers in some sources.

1.2.4 Spatial Distribution and Associating Sites

Many interferometric observations for the 6.7 GHz methanol masers have been conducted so far. Most of their observations were achieved with spatial resolutions of ∼1 arcsec. They showed linear spatial structure and linear radial velocity gradient along that structure as common characteristics of the 6.7 GHz methanol masers in ∼40% sources, although in remaining ∼60% sources the 6.7 GHz methanol maser spots were randomly distributed. In the recent half decade, the VLBI observations, which achive spatial resolutions of a few mas ∼1000 times higher than that with former interferometers, become to increase, and then these morphology have been interpreted using several explanations as follows.

Accretion disk?

The linear spatial structure and linear radial velocity gradient were generally interpreted as an edge-on Keplarian rotating disk around a high-mass YSO, as shown in figure 1-7 (left-panel). This interpretation is consistent with strong maser emissions caused by well stimulated along the line of sight on long path lengths. These characteristics were discoverd by [127]Norris et al. (1993), and they suggested the above interpretation. Then, [115]Minier et al. (2000) also suggested the same interpretation with the VLBI

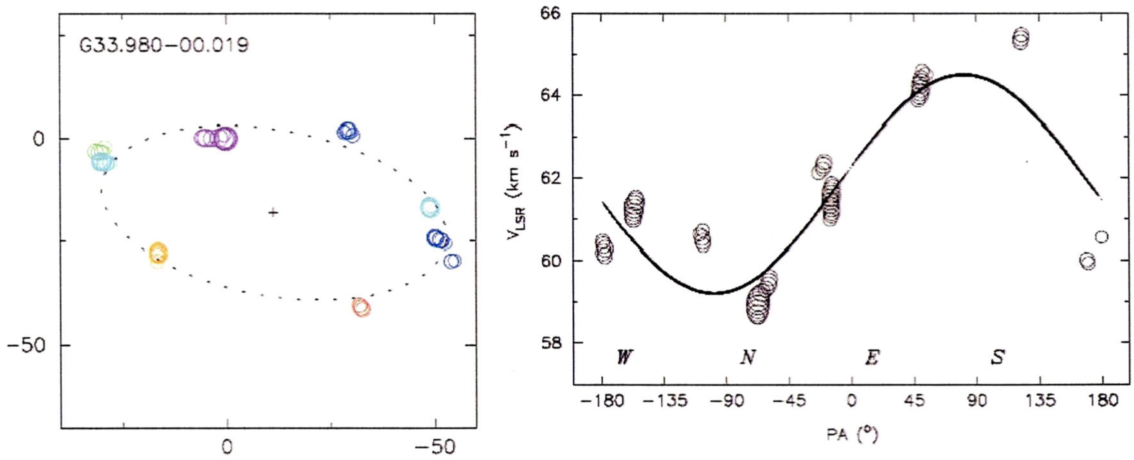

Figure 1-6: A spatial distribution and a radial velocity field of the 6.7 GHz methanol maser spots in HMSFR G 33.980−00.019 (extracted from [7]Bartkiewicz et al. 2009). Left-panel:the spatial distribution using color circles, where the sizes of circles are proportional to the logarithm of the intensities of each maser spot, and the colors relate to the radial velocities. The best-fit ellipse and its center are described by a dotted curve and a cross, respectively; Right-panel:radial velocity field versus azimuth angle measured from the major axis of the ellipse. The sinusoidal line represents the best-fit kinematical model of a rotating and expanding disk.

observations using the European VLBI Network (EVN), one of which is shown in figure 1-7 (right-panel). The linear structure and velocity gradient were seen remarkabely in HMSFR NGC7538 IRS1 ([114][115]Minier et al. 1998, 2000; [132][133]Pestalozzi et al. 2004, 2006). However, the central masses estimated from the Keplarian rotation model were not reached to high-mass, that is eight times or more than the solar mass, in most of observed sources: 0.001-0.26 $M_\odot$ ([115]Minier et al. 2000).

Recently, [7]Bartkiewicz et al. (2009) represented statistical VLBI imaging results of the 6.7 GHz methanol masers, and showed elliptical spatial structures occured in ~30% sources (9/31) including the clear ring structure discovered in G 23.657−0.127 by [5]Bartkiewicz et al. (2005a). These results were interpreted that the 6.7 GHz methanol masers showing eilliptical morphology were associated with disks accompanying expansion or infall using the following equation 1-3 to the position and radial velocity of the maser spots:

$$V_{\rm lsr} = \frac{x'}{a} \sin i \cdot V_{\rm rot} + \frac{y'}{a} \tan i \cdot V_{\rm exp} + V_{\rm sys} \tag{1-3}$$

where $V_{\rm lsr}$ is the radial velocity of the maser spot, $V_{\rm rot}$, $V_{\rm exp}$, $V_{\rm sys}$ is the rotation, expansion, and systemic velocity of each source, respectively. And x', y' are the central position, a the radius of the major axis, and i the inclination angle of the ellipse structure. The fitting expample for G 33.980−00.019 is shown in figure 1-6. They noted that in general the expansion or infall velocity was higher than the rotation component ($V_{\rm exp}$: −2.88 - +3.96 km s^{-1}, $V_{\rm rot}$: −1.26 - +8.64 km s^{-1}).

Outflow?

As mentioned above, ~60% methanol maser sources observed with interferometer having an arcsec resolution showed random spatial distributions. [135]Phillips et al. (1998) represented 17 out 45 sources (38%) with the linear structure and velocity gradient, while [184]Walsh et al. (1998) represented 36 out 97 (38%) with the same characteristics. But the remaning sources at least had no linear velocity gradient. The remaning sources

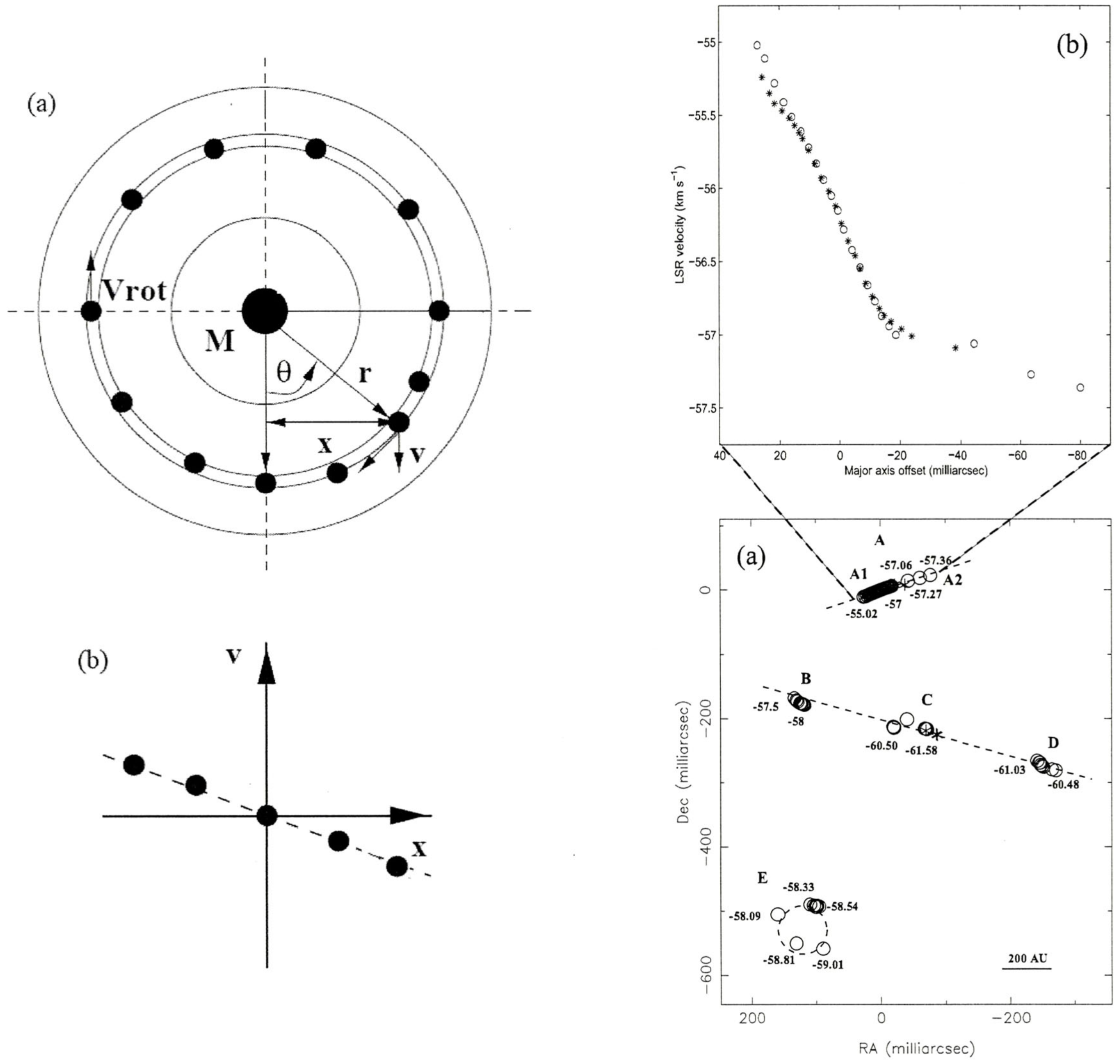

Figure 1-7: Left-panel:the edge-on Keplarian rotating disk model (extracted from [115]Minier et al. 2000). (a) a rotating disk around a YSO. The figure is seen from the face-on direction; (b) position versus radial velocity diagram. These postions of maser spots are projected on the x axis; Right-panel:the 6.7 GHz methanol maser emissions in HMSFR NGC7538 (extracted from [115]Minier et al. 2000). (a) spatial distribtuion using circles (6.7 GHz) and asterisks (12.2 GHz) symbols; (b) position-velocity diagram. White and black circles correspond to maser spots at 6.7 GHz and 12.2 GHz, respectively.

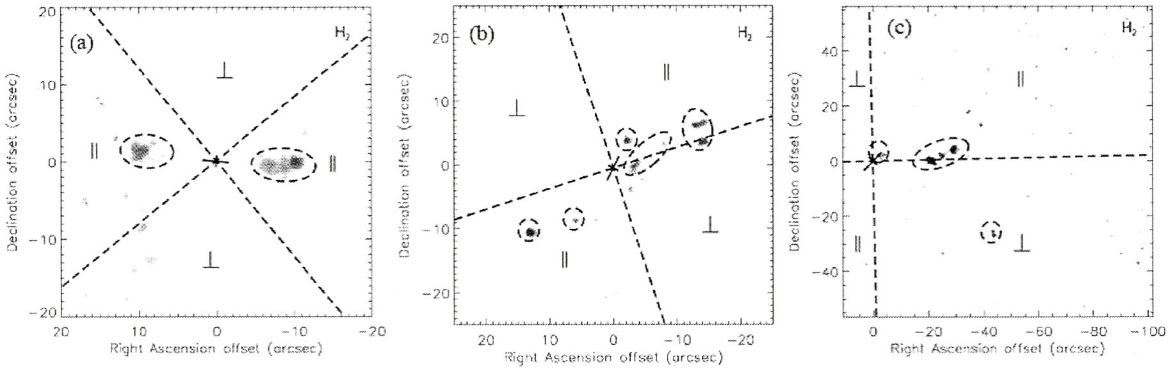

Figure 1-8: Spatial relations between the 6.7 GHz methanol masers and the H_2 emission at 2.12 μm (extracted from [43]De Buizer 2003). (a) G 320.23−0.28; (b) G 318.95−0.20; (c) G 313.77−0.86.

were interpreted as being associated with low-velocity shock regions. [43]De Buizer (2003) showed interesting spatial relation between the 6.7 GHz methanol masers and the H_2 emission at 2.12 μm, which are well known to be a shock tracer. That result was that the linear spatial structures were parallel to the direction of the H_2 emission in 16 out 18 sources, as shown in figure 1-8. This suggested that in the parallel sources the 6.7 GHz methanol masers were thought to trace an outflow, although a clear parallel case was seen in only one source, G 320.23−0.28. [120]Moscadelli et al. (2002) detected internal proper motions of the 12.2 GHz methanol maser spots (classified in Class II methanol masers as well as the 6.7 GHz ones) in HMSFR W3(OH), and the motions correponded to expanding motions with amplitudes of 1–7 km s^{-1}. The expansion motions were interpreted as a conical outflow model.

Other morphology

There are other interpretation toward the linear structure and velocity gradient as introduced above, and other morphology.

[45]Dodson et al. (2004) interpreted the linear structure using the planar shock model in a rotating molecular cloud. In the model, the methanol masers were excited on a parallel shock wave, and the shock wave propagated nearly perpendicular to the line of sight. The linear velocity gradient was thought to be caused by inclination between the shock front and the rotation axis of the molecular cloud.

[70]Goddi et al. (2007) conducted superposition the 6.7 GHz methanol maser spots on the 22.2 GHz water maser and radio cotinuum maps with a high absolute postional accuracy of a few mas in HMSFR AFGL5142, as shown in figure 1-9. Since the 6.7 GHz methanol maser spots located at nearer to a YSO compared to the water maser spots and the methanol spots occured in front of the radio cotinuum, which was optically thick at 6.7 GHz, showed red-shifted radial velocities to the systemic velocity, they interpreted that the AFGL5142 methanol maser was associated with an infall caused by accreting matter through the rotating disk.

[122]Moscadelli et al. (2007) superposed the 6.7 GHz methanol maser spots on line emissions observed in CH_3CN and CO lines in HMSFR G 24.78+0.08. They showed the G 24,78+0.08 methanol masers were associated with rotating toroids observed by the CH_3CN line, which had one magnitude larger sizes (~10000 AU) and masses ($>100\ M_\odot$) than that in the case of a rotating disk, as shown in figure 1-10. These toroids with large spatial scales are thought to be diagnostic in O spectral type stars.

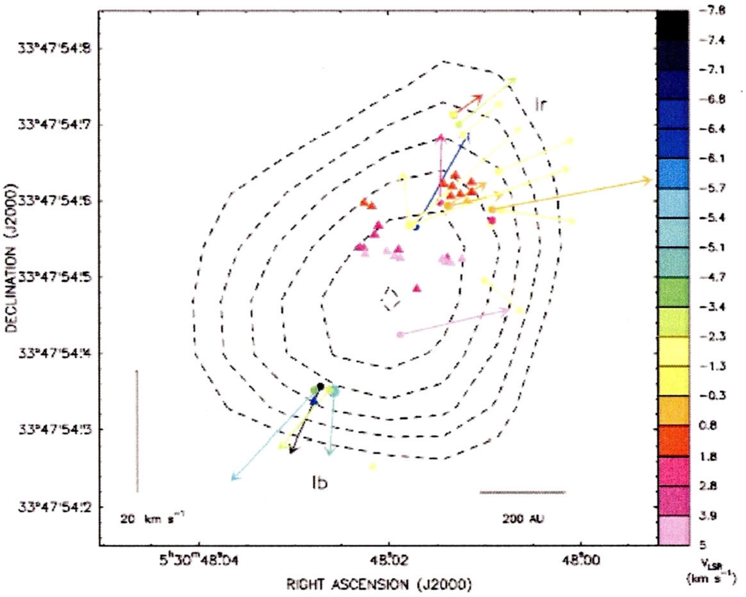

Figure 1-9: The spatial distribution of the 6.7 GHz methanol maser spots (triangles) with the water maser spots (circles) in HMSFR AFGL5142 (extracted from [70]Goddi et al. 2007). Colors corresponding to radial velocities of each maser spot. Arrows represent internal proper motions of the water maser spots. Contours show radio continuum emissions at 22 GHz.

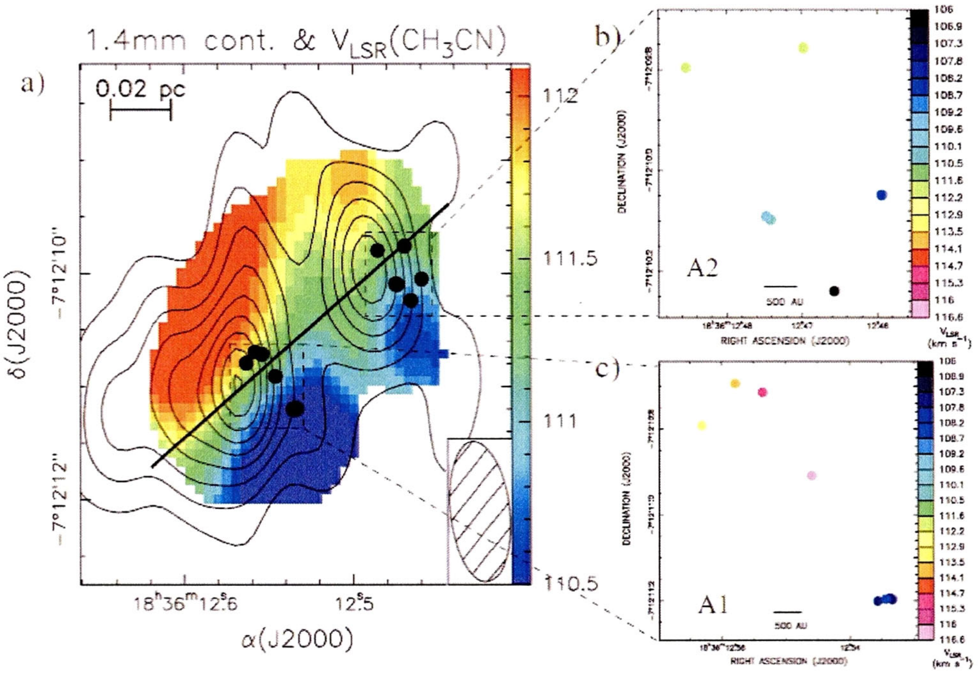

Figure 1-10: (a) The spatial distribution of the 6.7 GHz methanol maser spots (circles) in HMSFR G 24.78+0.08 superposed on CH_3CN line emissions (extracted from [122]Moscadelli et al. 2007). Contours represent radio continuum emissions at 1.4 mm; (b) blow-up in A2 region; (c) blow-up in A1 region.

1.3 Aim of Our Study

As mentioned above, in the recently half decade the accretion scenario through the rotating disk that could be around high-mass YSOs has become to be popular as the process of high-mass star formation on the basis of mainly the molecular line observations. Next step is naturally thought to directly detect the rotation and infall caused by accreting matters as internal propre motions. The internal proper motion measurements of the methanol maser emissions at 6.7 GHz using VLBI technique could provide directly motion information of rotation and expansion/infall of the disk around high-mass YSOs. There are only a few cases that could detect internal proper motions of the 6.7 GHz methanol masers so far. Our challenging multi-epoch VLBI observations would provide three-dimentional dynamics around high-mass YSOs as well as information of associating sites of this maser itself, that is whether the methanol maser is associated with a disk or a shock formed by an outflow.

We selected three HMSFRs as monitoring sources: Onsala 1 (ON 1), W75 North (W75 N), and Cepheus A (Cep A). The 6.7 GHz methanol maser emissions in these sources are bright enough to be observed with a VLBI technique, locate in northern hemisphere (declination > 30°) to make our observation using the Japanese VLBI Network (JVN) easy. This is the established network with 50–2560 km baselines across the Japanese islands ([63]Fujisawa 2008), and consists of thirteen antennas, including four radio telescope of the VLBI Exploration of Radio Astrometry (VERA: [90]Kobayashi et al. 2003, shown in figure 1-11 left-panel). The 6.7 GHz receivers have been installed at six antennas, which are Yamaguchi 32-m, Usuda 64-m, and the VERA four telescopes since 2009, as shown in figure 1-11 (right-panel). One of which sources, Cep A, are thought to have a rotating disk around a high-mass YSO by molecular line observations. Cep A could be the best candidate to detect internal rotating with expansion/infall motions in our observations. These sources also have other probes: the water and hydroxyl masers, molecular lines, radio (cm, mm and sub-mm) cotinuum emissions, and IR sources. These properties can provide significant information about the associating sites of the maser itself by superposing on a image of the methanol maser as well as detection internal proper mtotions, and about evolutionary phases of each high-mass YSO associated with the methanol masers.

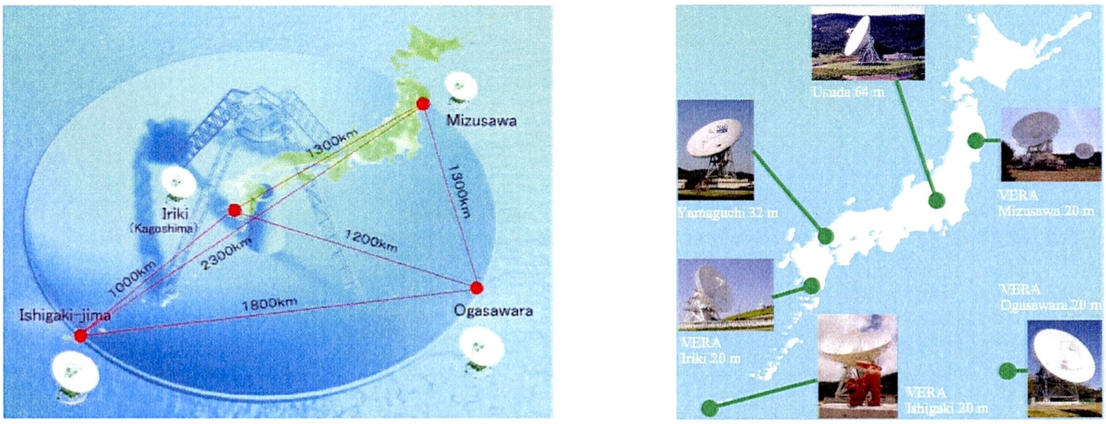

Figure 1-11: Left-panel:the VERA array (extracted from the VERA home-page[195]); Right-panel:the JVN array at 6.7 GHz.

Chapter 2

VLBI Survey Observations with the JVN at 6.7 GHz

We have conducted the VLBI monitoring observations for the 6.7 GHz methanol maser sources using the JVN since 2005. But there are only three radio telescopes of the JVN that the 6.7 GHz receivers were installed in 2005: Yamaguchi 32-m, VERA-Mizusawa 20-m, and VERA-Ishigaki 20-m, which formed the longest baseline of ~2300 km (~50 Mλ at 6.7 GHz) corresponding to a fringe spacing of ~4 mas. We had to made feasibility assessment to verify the imaging capability of this network.

We should be care about a size of the 6.7 GHz methanol maser spots and being resolved out with our longest baseline. [116]Minier et al. (2002) discussed the size and structure of an individual masing region in detail based on their 6.7 nd 12.2 GHz observations. They showed that the majority of the masing regions consist of a compact maser core surrounded by extended emission (halo). The core and halo sizes were derived as 2-20 AU and 12-290 AU, respectively. Until 2005, studies of the spot size had been made for only a few cases at 6.7 GHz, and the number of sources imaged with a baseline of $\geq$50 Mλ at 6.7 GHz was only two ([111]Menten et al. 1992; [5]Bartkiewicz et al. 2005a). Therefore, we also had to confirm the detectability of the 6.7 GHz methanol masers with our longest baseline of ~50 Mλ.

We made a snap-shot imaging survey toward thirteen sources associated with HMSFRs listed in table 2-1: W3(OH), Mon R2, S 255, W 33A, IRAS 18151−1208, G 24.78+0.08, G 29.95−0.02, IRAS 18556+0136, W 48, OH 43.8−0.1, ON 1, Cep A and NGC 7538. These target sources were bright and had widespread velocity range. The $5_1 \rightarrow 6_0A^+$ methanol transition at 6668.518 MHz was observed on 2005 September 26 from 5:00 to 21:00 UT using three telescopes (Yamaguchi 32 m, VERA-Mizusawa 20 m, VERA-Ishigaki 20 m) of the JVN. The maximum fringe spacing was 9.1 mas (Yamaguchi–Mizusawa, 22 Mλ) and the minimum was 4.1 mas (Mizusawa–Ishigaki, 50 Mλ). Right-circular polarization was received at Yamaguchi with system noise temperature of 220 K, while linear polarization was received at Mizusawa and Ishigaki stations with system noise temperatures of 120 K. The data were recorded on magnetic tapes using the VSOP-terminal system at a data rate of 128 Mbps with 2-bit quantization and 2 channels, and correlated at the Mitaka FX correlator [149]Shibata et al. (1998). From the recorded 32 MHz bandwidth, 8 MHz (6664 MHz to 6672 MHz) was divided into 1024 channels and used for data analysis, yielding a velocity resolution of 0.35 km s^{-1}. Scans of 15 minutes duration were made for 2-4 times on each target source at different hour angles in order to improve uv-coverages. The number of scans for each source is shown in table 2-2. Strong continuum sources, NRAO 530, 3C 454.3, and 3C 84, were observed every two hours for bandpass and delay calibration.

The data were reduced using the Astronomical Image Processing System (AIPS; [78]Greisen 2003). Processes of the data reduction are described in chapter 4. We have searched maser spots over an area of 4.0″ × 4.0″ with the Difmap software ([146]Shepherd 1997). Structure models were made by model-fitting with point sources and self-calibration algorithms iteratively. The phase solutions of self-calibration were applied to all the other channels.

2.1 Results

All of the targets, except for S 255, were detected. The six out of twelve sources detected in this JVN observation were the first VLBI results at 6.7 GHz at that time (published in 2008: [160]Sugiyama et al. 2008a). Observational results are summarized in table 2-2: column 1 is source name, column 2 number of observational scans, column 3-4 parameters of synthesized beam, column 5 rms of image noise in a line-free channel, column 6 reference velocity channel used in fringe-fitting and self-calibration, column 7

Table 2-1: The sample of 6.7 GHz methanol masers (information was published in 2008).

Source	Coordinates(J2000.0) RA (h m s)	Dec (° ′ ″)	Ref.	S_{p} (Jy)	d (kpc)	VLBI obs.
W3(OH)	02 27 03.820	61 52 25.40	10	3294	1.95	1
Mon R2	06 07 47.867	−06 22 56.89	4	104	0.83	6, 7
S 255	06 12 54.024	17 59 23.01	6	79	1.59	6, 7
W 33A	18 14 39.52	−17 51 59.7	14	297	4.0	...
IRAS 18151−1208	18 17 58.07	−12 07 27.2	14	119	3.0	8
G 24.78+0.08	18 36 12.57	−07 12 11.4	*	84	7.7	12
G 29.95−0.02	18 46 03.741	−02 39 21.43	6	182	9.0	...
IRAS 18556+0136	18 58 13.1	01 40 35	13	191	2.19	...
W 48	19 01 45.5	01 13 28	3	733	3.27	6
OH 43.8−0.1	19 11 53.987	09 35 50.308	2	51	2.8	...
ON 1	20 10 09.1	31 31 34	13	107	2.57	...
Cep A	22 56 17.903	62 01 49.65	14	371	0.70	...
NGC 7538	23 13 45.364	61 28 10.55	6	256	2.65	5, 6, 7, 9, 11

Column 1: source name; Column 2–3: coordinates in J2000.0; Column 4: reference of coordinates; Column 5: peak flux densities from the single-dish observation by Yamaguchi 32 m telescope; Column 6: source distance; Column 7: published VLBI observations at 6.7 GHz.

References — (1) Menten et al. (1992); (2) Kurtz et al. (1994); (3) Caswell et al. (1995); (4) Walsh et al. (1998); (5) Minier et al. (1998); (6) Minier et al. (2000); (7) Minier et al. (2001); (8) Voronkov et al. (2002); (9) Pestalozzi et al. (2004); (10) Etoka et al. (2005); (11) Pestalozzi et al. (2006); (12) Moscadelli et al. (2007); (13) Joint IRAS Science W.G. 1988; (14) Fringe rate mapping in our observations (accuracy of position is from 100 to 300 mas).

* The coordinate of this source is not used for this data reduction. This coordinate is obtained from the observations made in the following year. It is coincident with the coordinate in the catalog listed by [130]Pestalozzi et al. (2005).

Table 2-2: Observational Results

Source	N_{scan}	$\theta_{\mathrm{maj}} \times \theta_{\mathrm{min}}$ (mas × mas)	$P.A.$ (deg)	σ (Jy beam^{-1})	v_{ref} (km s^{-1})	N_{spot}	$S^{\mathrm{p}}_{\mathrm{VLBI}}/S^{\mathrm{p}}$ (%)	S_{VLBI}/S (%)
W3(OH)	3	5.5 × 2.3	131	0.24	−45.46	48	31	45
Mon R2	2	19.3 × 2.1	140	0.30	10.64	8	24	33
S 255	2	19.4 × 2.1	144	...	...	...	...	
W 33A	3	12.6 × 2.5	138	0.37	39.69	19	45	51
IRAS 18151−1208	3	10.9 × 2.5	138	0.63	27.83	13	84	208
G 24.78+0.08	3	9.5 × 2.4	135	0.28	113.43	21	33	27
G 29.95−0.02	2	19.5 × 2.2	139	0.46	96.10	14	86	78
IRAS 18556+0136	3	9.4 × 2.5	135	0.32	28.57	6	37	36
W 48	3	12.2 × 3.0	99	0.67	42.45	24	68	91
OH 43.8−0.1	2	16.2 × 2.2	139	0.36	39.48	9	18	30
ON 1	4	4.3 × 2.5	112	0.23	−0.07	7	4	27
Cep A	4	4.1 × 2.6	87	0.62	−2.56	30	86	65
NGC 7538	4	3.9 × 2.5	95	0.20	−56.10	20	69	30

Column 1: source name; Column 2: number of scans; Column 3: FWMHs of major and minor axes of synthesized beam; Column 4: position angle of major axis of beam; Column 5: rms of image noise in a line-free channel; Column 6: reference velocity channel; Column 7: number of the detected maser spots; Column 8: flux ratio of the correlated to the total-power spectra at the peak channel of total spectra; Column 9: flux ratio of the correlated to the total-power spectra of the integrated spectra.

number of the detected maser spots in our snap-shot observations, and column 8-9 flux ratios of the correlated to the total-power spectral at the peak channel of total spectra and that of the integrated spectra, respectively. The channel-velocity maps of the detected sources and descriptions for each source are refered in appendix C. The correlated (CLEANed component) spectra and total-power spectra of the 6.7 GHz methanol masers for all of target sources are shown in figure 2-1, 2-2. The spatial distributions of maser spots show various morphology, such as linear (Cep A, NGC 7538), ring like structure (W 48), largely separated clusters (W3(OH), W 33A, G 24.78+0.08, G 29.95−0.02, IRAS 18556+0136, OH 43.8−0.1, ON 1, Cep A).

The rms of the image noise in a line-free channel ranges from 200 to 670 mJy beam^{-1}. The minimum detectable sensitivities of 7σ were in the range of 1.4 to 4.7 Jy beam^{-1}. The maximum dynamic range was 196 for W3(OH). The projected baseline ranged from 11 to 50 Mλ for all sources, except for W 33A, IRAS 18151−1208, and G 24.78+0.08 (7 to 50 Mλ). The ratio of the correlated flux densities at the longest baseline of 50 Mλ to that at zero-baseline (total-power) was 20 % on average.

2.2 Spot Size

We discuss the size of methanol maser spots at 6.7 GHz. We detected twelve out of thirteen methanol masers at 6.7 GHz with the longest baseline being 50 Mλ of our array. The integrated flux densities of the correlated spectra account for ~50 % of the total flux, and some of them account for more than 90 %. This high detection rate, flux recovery, and small fringe spacing of 4 mas suggest that most of the methanol maser emission has compact structures. This result is consistent with a previous study for W3(OH) by [111]Menten et al. (1992). We also showed that the correlated flux density at 50 Mλ is typically 20 % of the total flux density. The size of the maser spot inferred from the flux ratio varies from 2 to 30 AU (at a distance from 0.70 to 9 kpc of the sources). This is consistent with the core size of 2 to 20 AU obtained by [116]Minier et al. (2002). We could testified that the compact core component could be at least detected even with the longest baseline of the JVN ~50 Mλ.

At that time, new 6.7 GHz receivers had planned to be installed at other three telescopes: Usuda 64-m, VERA-Iriki 20-m, and VERA-Ogasawara 20-m. The Usuda telescope is the largest one and has the highest sensitivity in Japan, and then would be expected to improve image sensitivities. The VERA-Iriki 20-m telescope has a key role to make short-baselines of the JVN, especially with Yamaguchi 32-m telescope correspond to ~300 km (~7 Mλ), and then would be expected to prevent “resolved out”. The VERA-Ogasawara 20-m telescope is a key station to make a better UV-coverage (a basis of a synthesized beam). The diffuse halo components would be also able to detect the improved JVN array at 6.7 GHz.

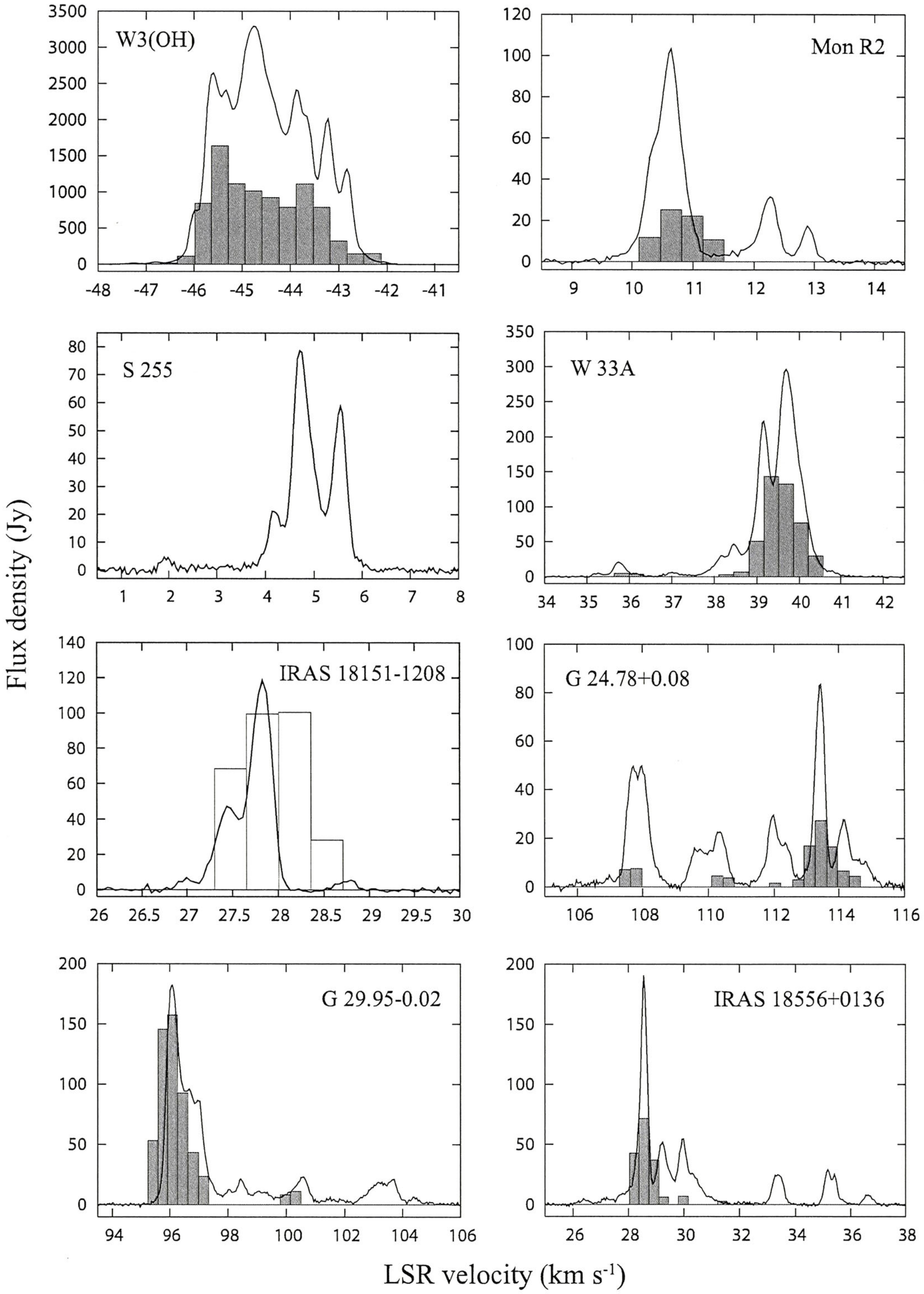

Figure 2-1: The correlated CLEANed component spectrum (block) and total-power spectrum (solid curve) of the 6.7 GHz methanol masers for all of sources.

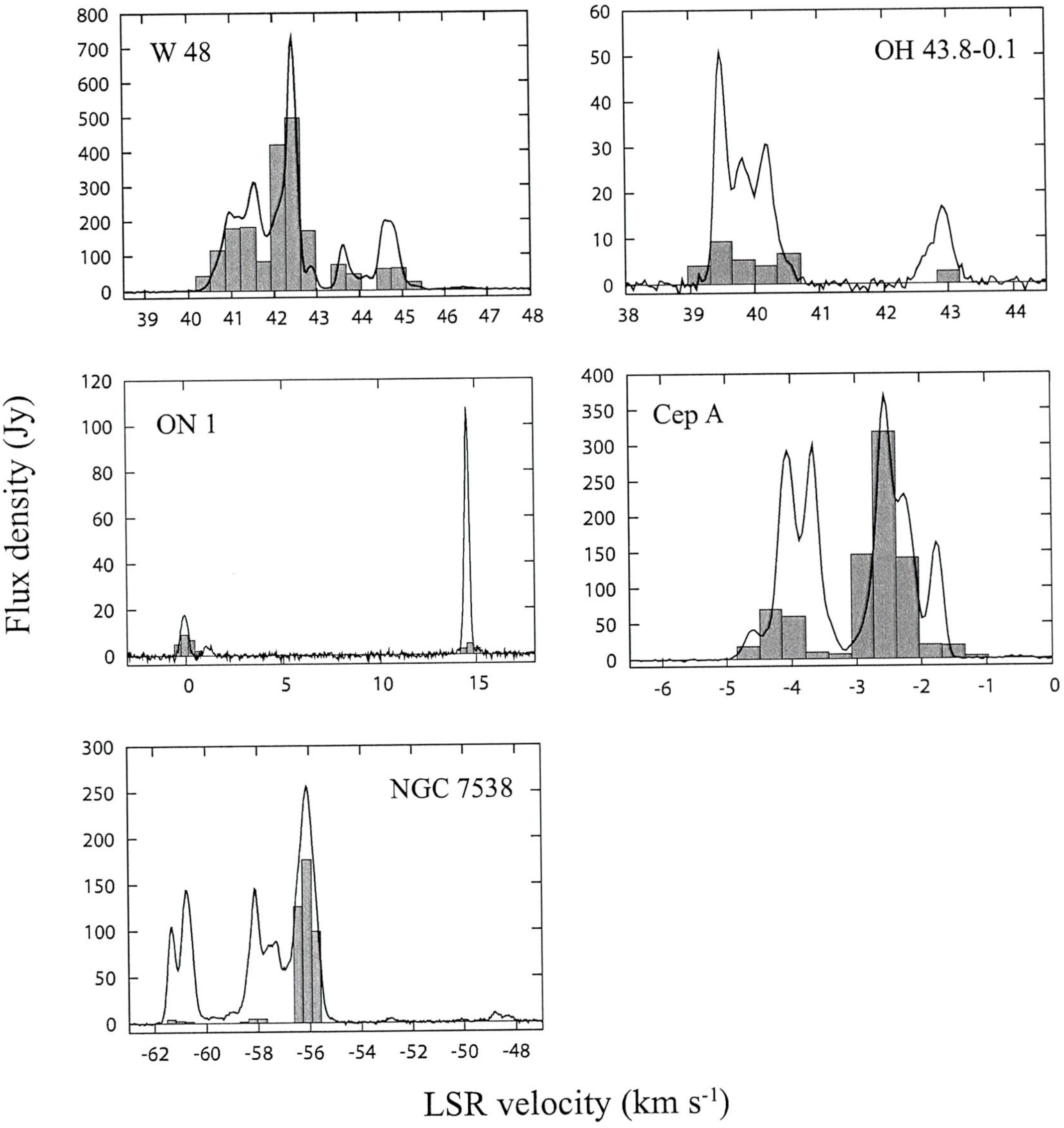

Figure 2-2: continued

Chapter 3

Sources for the Study of Internal Proper Motion

We obtained the VLBI image observed with the JVN in 2005 as already introduced in chapter 2. However, the image quality of this previous JVN observation did not allow the detailed investigation of the structure and exactly measuring internal proper motions because of poor uv-coverage and sensitivity. Also, only three telescopes in the JVN that 6.7 GHz receivers had been installed prevented self-calibration about amplitude corrections. We had to re-observe and conduct monitoring VLBI observations since 2006. Observational stations that new 6.7 GHz receivers would be installed had been increased in the JVN from 2006. We observed some 6.7 GHz methanol maser sources including the 2005 target sources, and ON 1, W75 N, and Cep A have been monitored more than two times. These three target sources to detect internal proper motions are described below in Right Ascension order.

3.1 Onsala 1 (ON 1)

(The following description for ON 1 is extracted from the published paper in 2011 [162].)

The HMSFR ON 1 is located at a distance of $2.57^{+0.34}_{-0.27}$ kpc ($1''$ corresponds to 2570 AU) based on trigonometric parallax measurement of the 6.7 GHz methanol masers ([141]Rygl et al. 2010). Although a distance of 1.8 kpc has been used for ON 1 by several authors (e.g., [105]MacLeod et al. 1998b; [95]Kumar et al. 2004; [125]Nagayama et al. 2008), we adopt the distance of 2.57 kpc in this paper. The radio continuum emission at 8.4 GHz showed an UC Hii region ([3]Argon et al. 2000). The submillimeter array (SMA) observations detected five continuum emission sources at 345 GHz (defined as SMA1–5) within a field of $\sim 5''$ ([157]Su et al. 2009, as shown in figure 3-1 left-panel). [157]Su et al. (2009) mentioned that the SMA1 and 3 are hard to distinguish from the UC Hii region observed by the 8.4 GHz radio continuum emission. Therefore, at least four YSOs exist within an area of only $5''$ (corresponding to ~13000 AU), that is the SMA2, 4, 5, and the UC Hii region. The water masers at 22.2 GHz in this area consist of two clusters ([47]Downes et al. 1979), WMC 1 and 2 (defined in [125]Nagayama et al. 2008, as shown in figure 3-1 right-panel). [125]Nagayama et al. (2008) showed that the water masers in WMC 1 were associated with a bipolar outflow on the basis of an east-west elongated structure and their internal proper motions. A corresponding large-scale outflow was observed by the CO $J = 2{-}1$ line ([95]Kumar et al. 2004) and H_2 emission at 2.12 μm ([94]Kumar et al. 2003). Some bipolar outflows exist; one of them, traced by $H^{13}CO^+$ $J = 1{-}0$ and SiO $J = 2{-}1$ line emission, shows outflows in the northeast-southwest direction at a position angle (PA) of $\sim 44°$ ([95]Kumar et al. 2004). The ground-state hydroxyl masers at 1.665 and 1.667 GHz in this area are associated with the UC Hii region ([126]Nammahachak et al. 2006). A monitoring observation showed the expansion of the hydroxyl masers at ~5 km s^{-1}, and the masers were thought to trace the expansion of the UC Hii region ([59]Fish & Reid 2007).

The 6.7 GHz methanol masers in ON 1 have two widely separated spectral features at velocities of ~15 km s^{-1} ($V_{\rm lsr} \sim 0$, 15 km s^{-1}: [109]Menten 1991b; [165]Szymczak et al. 2000). The systemic velocity of this region based on the CS $J = 2{-}1$ line is 11.6 ± 3.1 km s^{-1} ([20]Bronfman et al. 1996). A different systemic velocity of 5.1 ± 2.5 km s^{-1} is observed using the H76α recombination line ([193]Zheng et al. 1985). In either case, the systemic velocity is observed between the two methanol maser features. Since the kinematics of ON 1 were observed using various line emissions, including those of water and hydroxyl masers, this source is suitable for investigating the associated sites and evolutionary phases of the methanol masers.

Interferometric observations of the methanol masers in this region have been performed using the multi-element radio-linked interferometer network (MERLIN) by [76]Green et al. (2007). They succeeded in mapping only red-shifted features ($V_{\rm lsr}$ = 14.46 to

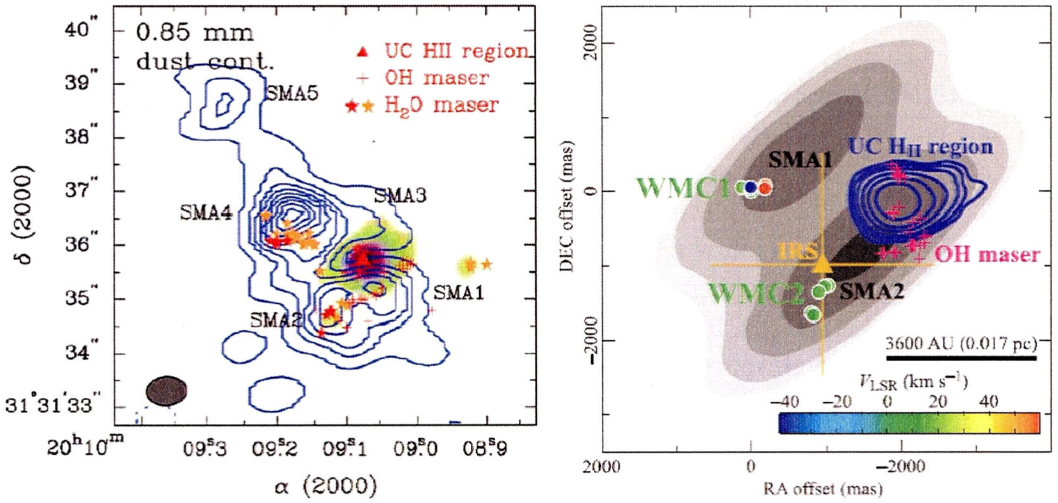

Figure 3-1: HMSFR ON 1. Left-panel:contour plots of 345 GHz continuum imaged observed with the SMA (extracted from [157]Su et al. 2009). The superposed color image is the VLA 22 GHz continuum in logarithmic scale, and the triangle represents the center position of the UC HII region. The crosses mark the position of hydroxyl masers detected by [126]Nammahachak et al. (2006). The red stars represent the positions of the water masers reported by [125]Nagayama et al. (2008), while the orange stars also show the position of the water masers but being not published. The dark ellipse located at left corner corresponds to the synthesized beam formed with the SMA; Right-panel:spatial distribution of the water maser spots superposed on an 8.4 GHz radio continuum image (blue contours) of the UC HII region (extracted from [125]Nagayama et al. 2008). This continuum is almost same to the color image in the left-panel. The gray-scale image shows the 345 GHz radio continuum representing dust emission detected by [158]Su et al. (2004). The crosses show the hydroxyl maser distribution ([60]Fish et al. 2005) and the triangle indicates the 10 μm infrared source position ([94]Kumar et al. 2003).

15.57 km s^{-1}) because the bandwidth did not cover both the features. VLBI observations for the ON 1 methanol masers, which covered both the features, were conducted using the JVN ([160]Sugiyama et al. 2008a) and the EVN ([141]Rygl et al. 2010).

3.2 W75 North (W75 N)

The W75 N is one of HMSFRs in North area of the Cygnus X region ([144]Schneider et al. 2006) located at a distance of 2 kpc (1″ corresponds to 2000 AU), and has an integrated far-infrared (FIR) luminosity of $1.4 \times 10^5 L_\odot$ forming mid- to early-B stars (e.g., [168]Torrelles et al. 1997). A large-scale greater than 3 pc molecular outflow was detected at different frequencies along a PA of 66° (e.g., [147]Shepherd et al. 2003) Mainly three radio continuum sources have been detected using the VLA at 22 GHz within $\sim 1.5''$ area, which were named as VLA 1–3 ([168]Torrelles et al. 1997, as shown in figure 3-2 left-panel) embedding B1, B2, and B1 spectral type stars, respectively ([148]Shepherd et al. 2004). [148]Shepherd et al. (2004) detected millimeter continuum emissions at 43 GHz toward VLA 2 and 3, whose emissions are thought to be due to a mixture of warm dust and ionized gas emissions. The water masers are mainly associated with the VLA 1 and 2 separated with a size of 0.7″ corresponding to 1400 AU ([168]Torrelles et al. 1997). The water maser spots associated with the VLA 1 were distributed along the elongated structure as well as the 22 GHz continuum emission with a size of $\sim$1″. On the other hand, the VLA 2 water maser spots surrounded the spatially unresolved continuum emission at 22 GHz with a size of $\sim 0.2''$. [171]Torrelles et al. (2003) detected internal proper motions for each water maser. The VLA 1 water masers showed a bipolar motion

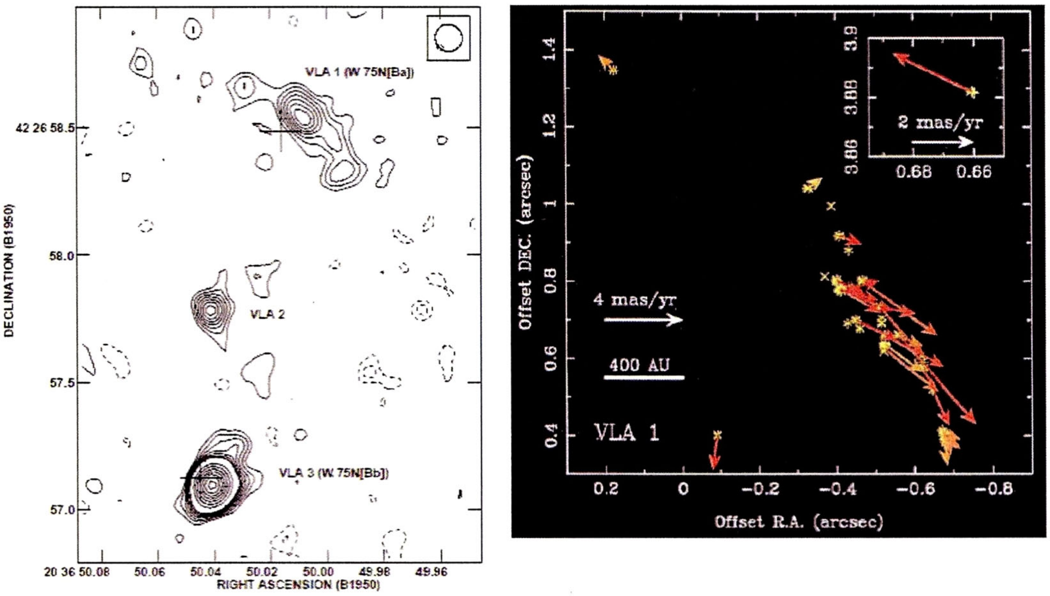

Figure 3-2: HMSFR W75 N. Left-panel:radio continuum contour image at 22 GHz (extracted from [168]Torrelles et al. 1997). Crosses indicate the position of the two 8.4 GHz continuum sources named as W75 N(Ba) and W75 N(Bb) by [84]Hunter et al. (1994). The synthesized beam is shown in right-top corner; Right-panel:internal proper motions of the water maser spots represented by arrows (its lengths represent the motion vectors) associated with the VLA 1 (extracted from [171]Torrelles et al. 2003).

parallel to the elongated radio continuum structure, and the motion was well-collimated with an opening angle (OP) $< 10°$, as shown in figure 3-2 right-panel. In contrast, the VLA 2 water masers represented an spherical-outward motion from the central source in the VLA 2 radio continuum source, and the motion showed $\sim$ 30 km s^{-1} higher than the motion of the VLA 1 water maser. The hydroxyl masers in W75 N are well known to often indicate flux flare phenomenon, and the flare spots took place $\sim 0.15''$ west from the VLA 2 (e.g., [2]Alakoz et al. 2005; [152]Slysh et al. 2010). Ohter most of the hydroxyl maser spots are associated with VLA 1, forming an elongated arc structure in roughly north-south direction with a velocity gradient, which can be modelled by a rotating disk ([154]Slysh et al. 2002).

In the methanol maser spectrum at 6.7 GHz in W75 N, there are at least seven spectral features (e.g., [109]Menten 1991b). A VLBI observation of this methanol maser was conducted with the EVN ([115]Minier et al. 2000), and the distribution was associated with the VLA 1 ([117]Minier et al. 2001a). But the image could not represent weak emission at $V_{\rm lsr} \sim +9.4$ km s^{-1}. Recently a new image covering the spectral feature at $V_{\rm lsr} \sim +9.4$ km s^{-1} observed with the EVN was represented by [163]Surcis et al. (2009).

3.3 Cepheus A (Cep A)

The Cep A is one of the closest HMSFRs to the solar system at a distance of 0.70±0.04 kpc ($1''$ corresponds to 700 AU) based on trigonometric parallax measurement of the 12.2 GHz methanol masers ([123]Moscadelli et al. 2009). There is an infall gas with the velocity of 0.23±0.07 km s^{-1} observed with a large beam size ($\sim 30''$: [89]Klaassen & Wilson 2007; [159]Sun & Gao 2009). Some radio continuum sources were detected by [82]Hughes & Wouterloot (1984) with the VLA at 5 GHz, and these sources were named as HW1–7. The methanol masers at 12.2 GHz in Cep A have been observed with the VLBA ([115]Minier et al. 2000) and the distribution was associated with the Cep A-HW2 object. The HW2 object is the brightest radio continuum source, and that luminosity is

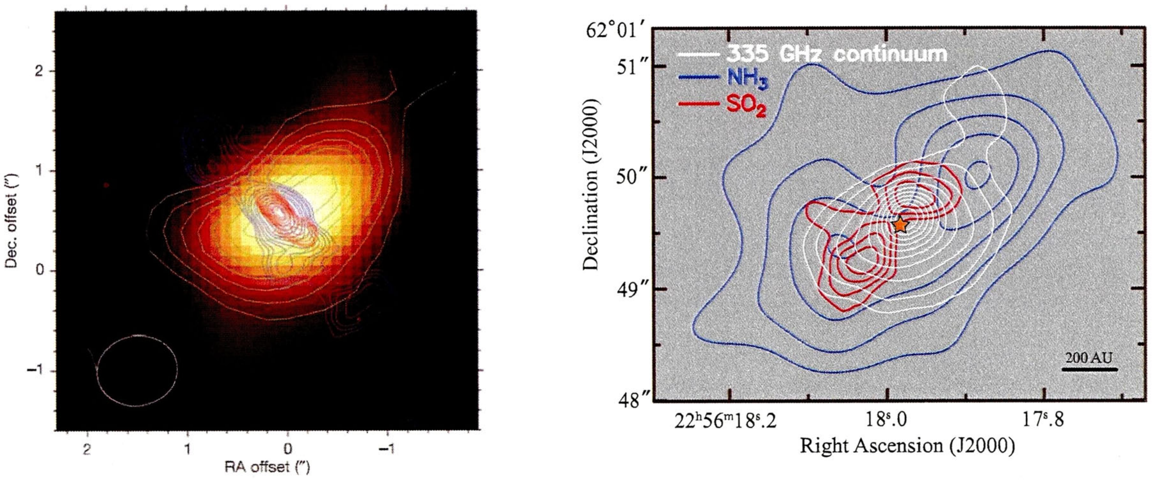

Figure 3-3: HMSFR Cep A-HW2. Left-panel:dust continuum emission at 327 GHz and the integrated intensity in the CH_3CN line emission are shown in the color image and the white contour, respectively (extracted from [129]Patel et al. 2005). The SMA beam size is shown in left-lower corner. Blue and red contours show the 8.4 and 22 GHz continuum emissions, respectively, which are from a well-collimated jet ([167]Torrelles et al. 1996); Right-panel:the integrated NH_3 (blue contours) and SO_2 (red contours) emission superposed on the 335 GHz continuum emissions shown as white contours (modified from [169]Torrelles et al. 2007). The 335 GHz continuum emission is almost overlaied on the 327 GHz dust emission in the left-panel. A star symbol indicates the position of the peak of 43 GHz continuum emission, which is thought to be the location of an exciting source ([37]Curiel et al. 2006).

thought to be about half of the bolometric luminosity of the entire region ([140]Rodríguez et al. 1994; [83]Hughes et al. 1995), while the entire luminosity is about $2.5 \times 10^4 L_\odot$ ([56]Evans et al. 1981). The HW2 object has a radio continuum jet along a PA of 45° with high-velocity of ~500 km s^{-1} ([140]Rodríguez et al. 1994; [83]Hughes et al. 1995; [167][170]Torrelles et al. 1996, 1998; [37]Curiel et al. 2006). Based on submillimeter observations of both dust and CH_3CN line emissions, a flattened disklike structure was found ([129]Patel et al. 2005, as shown in figure 3-3 left-panel). The structure has a size of about 1000 AU which is perpendicular to the jet, and an enclosed mass was estimated as $19 \pm 5 M_\odot$. It has been revealed that NH_3 and SO_2 line emissions coincided with the CH_3CN disk, although the SO_2 structure was about 2 times smaller ([169]Torrelles et al. 2007; [86]Jiménez-Serra et al. 2007, as shown in figure 3-3 right-panel). The 22.2 GHz water masers associated with the HW2 observed by [167]Torrelles et al. (1996) were distributed in an elongated structure perpendicular to the radio jet, which possibly traces the circumstellar disk around the HW2 object with a size similar to the SO_2 disk. The hydroxyl masers were distributed surrounding the HW2 object ([113]Migenes et al. 1992; [6]Bartkiewicz et al. 2005b), and those internal proper motions were mainly directed away from the central source.

The 6.7 GHz methanol maser in Cep A consists of mainly five spectral features (e.g., [109]Menten 1991b), and these features are grouped into two groupes: redshifted ($V_{\rm lsr} = -1.9$ and -2.7 km s^{-1}) and blueshifted ($V_{\rm lsr} = -3.8$, -4.2, and -4.9 km s^{-1}). [161]Sugiyama et al. (2008b) detected rapid, synchronized, and negative correlated variations of flux densities by daily monitoring observations with the Yamaguchi 32-m radio telescope, that were the redshifted features decreased in flux density to 50% of the initial value while the blueshifed ones rapidly increased within 30 days.

Interferometric observation to the 6.7 GHz methanol maser in Cep A was conducted with the MERLIN ([181]Vlemmings et al. 2010). The VLBI images were also obtained with the JVN ([160][161]Sugiyama et al. 2008a, b) and with the EVN ([172]Torstensson et al. 2010).

Chapter 4

Observations and Data Reduction

Table 4-1: Parameters of VLBI observations using the JVN.

Source	Epoch	Date	Telescopes*	t_{on}	Synthesized beam	
					$\theta_{\mathrm{maj}} \times \theta_{\mathrm{min}}$	PA
		(y/m/d)		(hr)	(mas×mas)	(°)
ON 1	1	2006/09/10	Y, U, M, I	3.4	6.3×3.2	−59
	2	2008/05/10	Y, M, R, O, I	1.5	4.6×3.1	−31
	3	2008/10/26	Y, U, M, R, O, I	0.5	5.0×3.2	−54
W75 N	1	2008/10/26	Y, M, R, O, I	0.8	5.9×3.1	−41
	2	2010/08/29	H, M, R, O, I	1.7	7.6×3.3	+84
Cep A	1	2006/09/09	Y, U, M, I	2.8	9.4×4.3	−70
	2	2007/07/28	Y, M, R, O, I	2.1	9.2×4.3	−43
	3	2008/10/25	Y, M, R, O, I	1.6	7.0×3.9	−79

Column 1: source name; Column 2: epoch number; Column 3: observational year, month, and day; Column 4: telescopes used; Column 5: total on-source time; Column 6–7: FWHMs of major and minor axes, and position angle of synthesized beam made in natural weight;

* Telescope code — Y: Yamaguchi, U: Usuda, M: VERA-Mizusawa, R: VERA-Iriki, O: VERA-Ogasawara, I: VERA-Ishigaki, H: Hitachi (Ibaraki).

The JVN observations were conducted for ON 1, W75 N, and Cep A as described in table 4-1. For ON 1 the observations were made at three epochs: 2006 September 10 from 07:00 to 17:30 UT using four telescopes of the JVN; 2008 May 10 from 15:00 to 22:00 UT using five telescopes; and 2008 October 26 from 06:00 to 13:00 UT using six telescopes. For W75 N the observations were at two epochs: 2008 October 26 from 06:00 to 13:00 UT using five telescopes; and 2010 August 29 from 16:00 to 19:00 UT using five telescopes. For Cep A the observations were at three epochs: 2006 September 9 from 15:00 to 22:00 UT using four telescopes; 2007 July 28 from 14:00 to 22:00 UT using five telescopes; and 2008 October 25 from 13:00 to 18:00 UT using five telescopes. The telescopes used in each observation are shown in table 4-1 with other observational parameters. The projected baselines ranged from 6 Mλ (Yamaguchi–Iriki) to 50 Mλ (Mizusawa–Ishigaki), corresponding to the fringe spacings of 34.4 mas and 4.1 mas at 6.7 GHz, respectively.

We conducted VLBI observations using a phase-referencing technique for ON 1 and Cep A to obtain absolute coordinates with an accuracy of a few mas scale. Unfortunately, there are no suitable continuum sources within 5° from W75 N which are observable with the JVN. A continuum source, J2003+3034 (1.71° from ON 1), whose coordinates were determined with an accuracy of 0.55 mas in the second VLBA calibrator survey (VCS2) catalog ([61]Fomalont et al. 2003), was used as a phase reference calibrator to obtain the absolute coordinates of the methanol masers. We alternately observed the ON 1 methanol masers and the continuum source with a cycle of 5 min (2 min on ON 1 and 1.8 min on the continuum source). ON 1 was sometimes observed continuously for more than 30 min to improve the uv-coverage in the first and second epochs. The total on-source times at each epoch were 3.4, 1.5, and 0.5 hours for ON 1 and 0.4, 0.7, and 0.3 h for J2003+3034, respectively. The phase-referencing observation for ON 1 was succeeded at only third epoch. A continuum source J2302+6405 (2.19° from Cep A), whose coordinate is known with an accuracy of 0.62 mas in the third VLBA Calibrator Survey (VCS3) catalog ([134]Petrov et al. 2005), was used as a phase reference calibrator. We alternately observed the Cep A methanol maser and the continuum source with switching observational mode with a cycle of 5 min (2 min on Cep A and 1.6 min on the continuum source). The total on-source times were 2.8, 2.1, and 1.6 h for Cep A and 0.7, 1.0, and 0.9 h for J2302+6405, respectively. The phase-referencing observation for Cep A was succeeded at only first epoch. Several radio continuum sources, which are listed in table 4-2, were also observed every one and half hours for clock parameter and bandpass calibration.

In 2006 observations, left-circular polarization (LCP) was received at the Yamaguchi and Usuda stations, while linear polarization was received at the Mizusawa and Ishigaki stations. LCP was received at the Yamaguchi, Usuda, Mizusawa, and Ishigaki stations, while at the Iriki and Ogasawara stations, linear polarization was received from 2007. From 2009 observations, all stations could receive LCP. A New 6.7 GHz station, Hitachi (locates in Ibaraki prefecture) 32-m radio telescope that a LCP receiver was installed, has joined from 2010. The data were recorded on magnetic tapes by using a VSOP terminal at a data rate of 128 Mbps with 2-bit quantization and two channels; they were correlated at the Mitaka FX correlator ([149]Shibata et al. 1998). Of the recorded 32 MHz bandwidth, 2 MHz (6668–6670 MHz for ON 1 and Cep A) was divided into 512 channels for obtaining high velocity resolution in the maser reductions, yielding a velocity resolution of 0.18 km s^{-1} in 2006. The same velocity resolution was achieved, but the bandwidth and the number of channels were 4 MHz (6668–6672 MHz for ON 1, 6666–6670 MHz for W75 N and Cep A) and 1024, respectively, since 2008. Single-dish observations were performed using the Yamaguchi 32 m telescope almost simultaneously with each VLBI observation for amplitude correction in the VLBI observations. The spectral resolution of the single dish was four times higher than that of the VLBI, that is 0.044 km s^{-1}.

The VLBI data were reduced using the AIPS ([78]Greisen 2003). Correlator digitization errors were corrected using the task ACCOR. Delay and rate offsets were corrected by the task FRING by using the continuum calibrators. Accuracies of the clock parameter corrections were estimated better than 0.1 mas. Bandpass calibration was performed by the task BPASS. Doppler corrections were performed by running the tasks SETJY and CVEL. Amplitude-gain calibration parameters were derived from the total power spectra of maser lines itself by using the template method in the task ACFIT. For ON 1, W75 North (W75 N) a strong (~270–470 Jy), nearby (~ 11.5°) methanol maser source was used for the amplitude-gain calibration. The primary amplitude unit was converted into janskys (Jy) on the basis of the single-dish spectrum observed using the Yamaguchi telescope by the same method. The conversion accuracy depends on the accuracy of the single-dish observations, ~10%. Fringe fitting was conducted using a strong velocity channel (each local standard of rest (LSR) velocities is listed in column 5 of table 4-2 in the task FRING. The phase and amplitude solutions of self-calibration were calculated in the task CALIB by using the image of the reference channel formed by the task IMAGR. The solutions were applied to all the other channels that contained maser emissions. We formed CLEAN images of each channel that included maser emissions by using the reference maser spot in the task IMAGR with natural weighting over an area of $4.0'' \times 4.0''$. The full width at half maximum (FWHM) and the PA of the synthesized beams are shown in table 4-1. The peak positions and peak intensities of maser spots were derived by fitting an elliptical Gaussian brightness distribution to each spot appearing in each image by using the task JMFIT. We identified maser spots on the basis of the signal-to-noise ratio (SNR) as well as the range of the velocity channels. All the identified spots were more than five times stronger than the rms noise level in the images for each spectral channel (SNR ≥ 5), and all appeared in multiple velocity channels. For Cep A, we searched and imaged maser spots with the Difmap software ([146]Shepherd 1997), because there were many maser spots in each channel and it made forming images complex. Structure models were made by model-fitting with point sources and self-calibration algorithms iteratively. The phase solutions of self-calibration were applied to all the other channels.

In addition to the analyses described above, special amplitude calibrations were necessary until 2009 observational data, because different polarizations (circular/linear) were correlated. Since a visibility amplitude reduces by $1/\sqrt{2}$ in correlation between linear and single circular polarization, the factor was corrected. For the case of linear and linear polarization, the amplitude varies with time depending on parallactic angle between antennas. Amplitude correction factors were calculated for each observational scan and applied to the visibilities. We made a baseline-based correction to each observational scan. The correction procedure was confirmed in some observations at different date by applying the task BLCAL for bright continuum sources. This process indicated that an accuracy of this calibration was ~10 %.

Table 4-2: Observed source parameters.

Source	Correction	Coordinates (J2000.0)		$V_{\rm lsr}$	Ref.*
		RA	Dec		
		(h m s)	° ′ ″	(km s^{-1})	
ON 1	target	20 10 09.0731	+31 31 35.934	0.00	1
J2003+3034	phase	20 03 30.24406	+30 34 30.7888		3
J2010+3322	delay	20 10 49.72330	+33 22 13.8101		3
J2023+3153	delay	20 23 19.01734	+31 53 02.3061		5
J2002+4725	delay	20 02 10.41827	+47 25 28.7735		2
3C454.3	bandpass	22 53 57.74794	+16 08 53.5609		5
NRAO530	bandpass	17 33 02.70579	−13 04 49.5482		5
DA193	bandpass	05 55 30.80561	+39 48 49.1650		5
W75 N	target	20 38 36.417	+42 37 34.85	+7.23	6
J2007+4029	delay	20 07 44.94483	+40 29 48.6041		5
3C418	delay	20 38 37.03474	+51 19 12.6626		5
3C454.3	bandpass	22 53 57.74794	+16 08 53.5609		5
Cep A	target	22 56 17.9042	+62 01 49.577	−2.64	1
J2302+6405	phase	23 02 41.31500	+64 05 52.8485		4
J2322+5057	delay	23 22 25.98218	+50 57 51.9637		5
J0102+5824	delay	01 02 45.76238	+58 24 11.1366		5
3C454.3	bandpass	22 53 57.74794	+16 08 53.5609		5
3C84	bandpass	03 19 48.16014	+41 30 42.1048		5

Column 1: source name; Column 2: purpose of observations (target:target source, phase:phase-referecing source, delay:clock parameter correction, bandpass:bandpass correction); Column 3-4: coordinates in J2000.0; Column 5: reference radial velocity; Column 6: reference of the coordinates.

* Reference — 1:this paper using phase-referencing technique; 2:the VLBA Calibrator survey (VCS1) catalog ([10]Beasley et al. 2002) 3:the second VLBA calibrator survey (VCS2) catalog ([61]Fomalont et al. 2003); 4:the third VLBA calibrator survey (VCS3) catalog ([134]Petrov et al. 2005); 5:the international celestial reference frame (ICRF) catalog ([102]Ma et al. 1998; [57]Fey et al. 2004); 6:Surcis et al. (2009).

Chapter 5

Results

Table 5-1: Result of the VLBI observations using the JVN.

Source	Epoch	$1\,\sigma_{\mathrm{image}}$ (Jy beam^{-1})	N_{spot}	σ_{range} RA (mas)	σ_{range} Dec (mas)
ON 1	1	0.08	36	0.02–0.80	0.01–0.59
	2	0.20	19	0.02–0.51	0.02–0.50
	3	0.32	23	0.03–0.73	0.02–0.50
W75 N	1	0.40	40	0.08–0.75	0.09–0.74
	2	0.15	53	0.05–0.62	0.03–0.50
Cep A	1	0.08	98	0.02–1.25	0.01–0.75
	2	0.10	97	0.04–0.72	0.03–0.81
	3	0.11	72	0.03–1.50	0.02–1.04

Column 1: source name; Column 2: epoch number; Column 3: rms of image noise in a line-free channel; Column 4: number of detected spots; Column 5-6: range of uncertainties for relative positional offsets with respect to the reference maser spot in RA and Dec directions.

We detected each maser spot for all of three sources as listed in table 5-1 using the JVN. Internal proper motions were also detected for ON 1 and Cep A in three epochs, and for W75 N in two epochs. The channel-velocity images and internal proper motions for each source are presented with each spectra in figures 5-1–5-7. For each figure about internal proper motions, we substracted the mean proper-motion vector of the detected maser spots from each individual proper motion, to remove the motion of the reference maser spot and transform to a frame of reference in which the mean proper motion is zero. In table 5-1, relative positional accuracies of the methanol maser spots with respect to the reference spot were also presented, which depend on the SNR and the spatial structure of the spot. The errors of fitting by an elliptical Gaussian were also included in the accuracy. We describe the results on each individual source below in Right Ascension order.

5.1 ON 1

(The following description for results of the methanol maser in ON 1 is extracted from the published paper in 2011 [162].)

5.1.1 Spatial Distributions

We detected 36, 19, and 23 maser spots at epochs 1, 2, and 3, respectively, while the number of independent spots are 41. The peak intensities of the spots ranged from ~0.3 to 30.9 Jy beam^{-1}, and the rms of the image noise ($1\,\sigma$) in a line-free channel was 80, 200, and 320 mJy beam^{-1}, respectively. Given 19 in 36 maser spots at 1st epoch had peak intensities larger than 1 Jy beam^{-1} (corresponds to rms 5, 3 σ of image noise at 2nd, 3rd epochs, respectively), detection rates are almost same above all epochs. Parameters of each maser spot are summarized in table 5-2. There are clearly flux variation for maser spots ID 5, 6, 15, 16, 18 according to accuracies of absolute flux ~10%. The maser emissions were detected even with longer baselines, and the correlated flux accounted for over 90% of the single-dish flux, as shown in figure 5-1.

The spatial distribution of the 6.7 GHz methanol maser spots in ON 1 at each epoch are shown in figure 5-1 with their spectra. The 36, 19, and 23 spots detected at each epoch within an area of ~400 × 1100 mas^2 (~1000 × 2800 AU^2) are plotted as dots with colors corresponding to $V_{\rm lsr}$. The origin of the map corresponds to the position of the reference spot with an LSR velocity of 0.00 km s^{-1}, whose absolute coordinates, obtained using a phase-referencing technique, are α(J2000.0) = 20$^{\rm h}$10$^{\rm m}$09$^{\rm s}$.0731 and δ(J2000.0) = +31°31′35″.934 with an accuracy of 1 mas. The reference spot is also used as a reference for internal proper motion. We define three clusters of maser spots: the north (cluster I), southwest (II: 0″.3 west, 0″.9 south), and south (III: 0″.1 east, 1″.0 south) clusters. Cluster I had a radial-velocity range of $V_{\rm lsr} = -0.52$ to 1.59 km s^{-1}, whereas the other two clusters had ranges of $V_{\rm lsr}$ = 14.24 to 15.12 and 14.24 to 14.77 km s^{-1} for clusters II and III, respectively. Cluster I was blue-shifted and clusters II and III were red-shifted relative to the systemic velocity. The blue-shifted maser spots were separated spatially as well as spectrally from the red-shifted ones.

The overall distribution of the ON 1 methanol masers coincided with that in the image obtained by [141]Rygl et al. (2010). Clusters II and III correspond to C and D defined by [76]Green et al. (2007). They also detected maser spots A and B in their MERLIN image, which are located at 0″.4 west, 0″.8 south and 0″.2 west, 0″.9 south, respectively, with respect to our reference maser spot, but we did not detect them in our VLBI image. The non-detection could be due to a difference of image sensitivities (a noise rms of 80 and 25 mJy beam^{-1} in the JVN and the MERLIN observations, respectively), or/and caused by being resolved out from a difference of spatial resolution (minimum fringe spacing ~4 and ~40 mas in the JVN and the MERLIN, respectively).

5.1.2 Internal Proper Motions

Maser spots detected in different epochs were identified as the same if their LSR velocities coincided within the velocity resolution of 0.18 km s^{-1} and their positions were within 2.7 mas at the first to third epochs (corresponding to a transversal velocity of ~15.5 km s^{-1} at 2.57 kpc, almost equivalent to the range of the radial velocity). On the basis of these criteria, 15 maser spots were identified at all three epochs, three spots were identified at the first and the third epochs, and three spots were identified at the second and the third epochs. The motions of 13 maser spots out of 21 identified spots were significantly larger than the relative positional uncertainties during the observation period. The internal proper-motion vectors are shown in figure 5-2(a), and the positional variations of each maser spot are shown in figure 5-3. The internal proper motions were measured by applying linear motion to the positional offsets on the timeline. The results of the internal proper-motion measurements are also shown in table 5-2.

As seen in figure 5-2(a), the internal proper motions reflected outward motions in roughly the north-south direction. The declination components of the proper motions μ_δ ranged from -0.63 to $+0.64$ mas yr^{-1}, which corresponds to tangential velocities V_y ranging from -7.7 to $+7.8$ km s^{-1}. The averaged north-south velocities were $+0.8\pm1.6$ km s^{-1} for cluster I ($V_{\rm I}$) and -4.2 ± 0.7 km s^{-1} for clusters II and III ($V_{\rm II,III}$) (north is positive). The difference between these velocities, $V_{\rm I} - V_{\rm II,III}$, is 5.0 km s^{-1}.

The outward motions in roughly the north-south direction clearly suggest that a rotating disk is unlikely to be the site associated with the 6.7 GHz methanol masers in ON 1. A simple explanation for the outward motion is that these masers are associated with an expanding shell or a bipolar outflow if we assume that the motion can be explain by mono-phenomenon. The north-south velocity $V_{\rm I} - V_{\rm II,III}$ of 5.0 km s^{-1} is comparable to the typical motion velocities of OH masers associated with an expanding shell ([16]Bloemhof et al. 1992; [59]Fish & Reid 2007). On the other hand, the direction of the outward motion is similar to that of the H^{13}CO^{+} and SiO outflows ([95]Kumar et al. 2004), which was roughly distributed in the north-south direction.

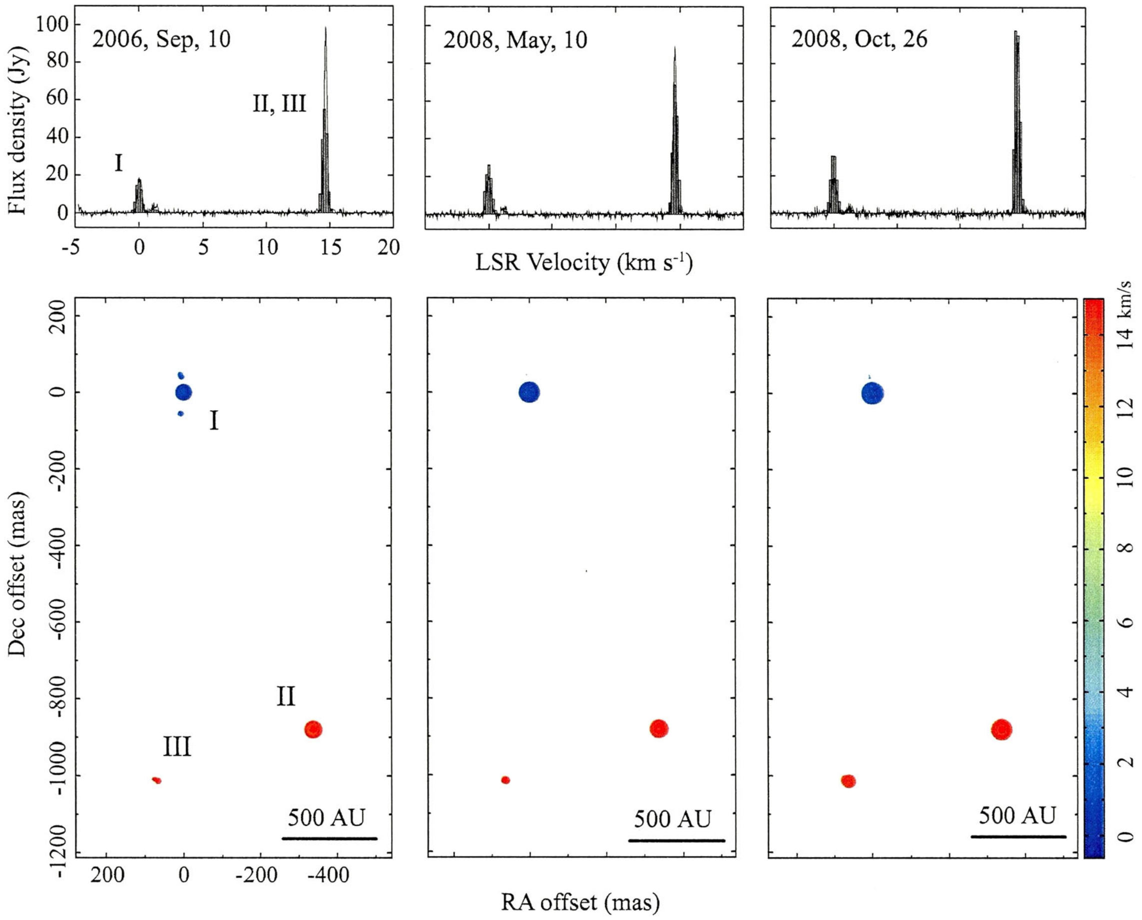

Figure 5-1: The 6.7 GHz methanol maser emissions in ON 1. Left-panel:maser spectra (upper) and spatial distribution (lower) in the first epoch. In the spectra, filled block and solid curve is CLEANed component spectrum and total spectrum, repsectively. In the distribution, size and color of the spot shown as filled circles indicates its peak intensity in logarithmic scale and its radial velocity (see color index at the right), respectively. The labels I, II, and III indicate each maser cluster. The origin of this map corresponds to the absolute coordinate of the 6.7 GHz methanol maser (α(J2000.0) = $20^{\rm h}10^{\rm m}09^{\rm s}.0731$, δ(J2000.0) = $+31^\circ31'35''.934$) measured by our observation; Middle-panel:same as left-panel but in the second epoch; Right-panel:same as left-panel but in the third epoch.

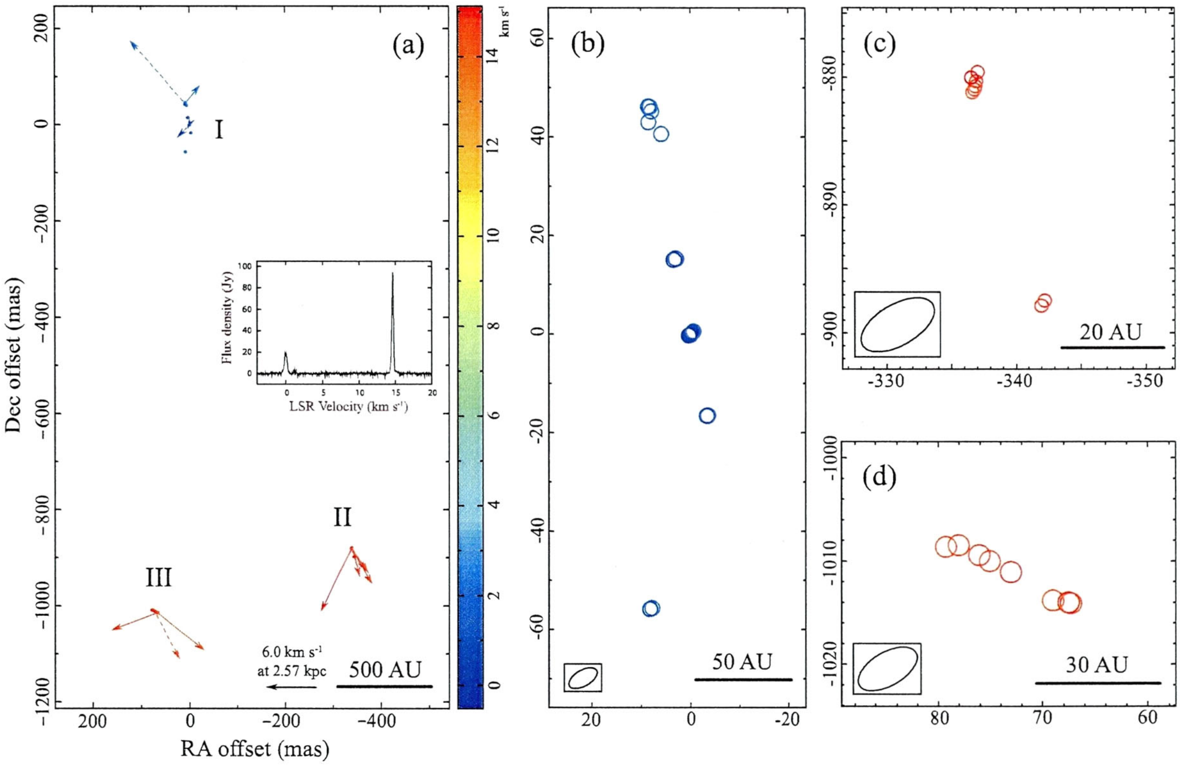

Figure 5-2: (a) Spatial distribution and internal proper motions of the 6.7 GHz methanol maser spots (filled circle and arrow) of ON 1. The color indicates its radial velocity (see color index at the right). The origin of this map corresponds to the absolute coordinates $\alpha(\mathrm{J2000.0}) = 20^{\mathrm{h}}10^{\mathrm{m}}09^{\mathrm{s}}.0731$ and $\delta(\mathrm{J2000.0}) = +31^{\circ}31'35''.934$. Arrows show proper motion of spots, and their lengths are proportional to the tangential velocities. The spatial and velocity scales are shown in the lower corner. The solid arrows show the motions detected at all three epochs, while the dashed arrows show ones detected in only two (first and third) epochs. The spectrum of the ON 1 methanol maser by single-dish observation using Yamaguchi 32 m telescope is also shown in the middle frame. The velocity resolution is 0.044 km s^{-1}, which is four times smaller than that of the VLBI observations (0.18 km s^{-1}). (b)–(d) Blow-up figures of cluster I, II, and III, respectively. Open circles show the methanol maser spots in a fixed scale. Each ellipse at bottom-left corner in each figure corresponds to a synthesized beam.

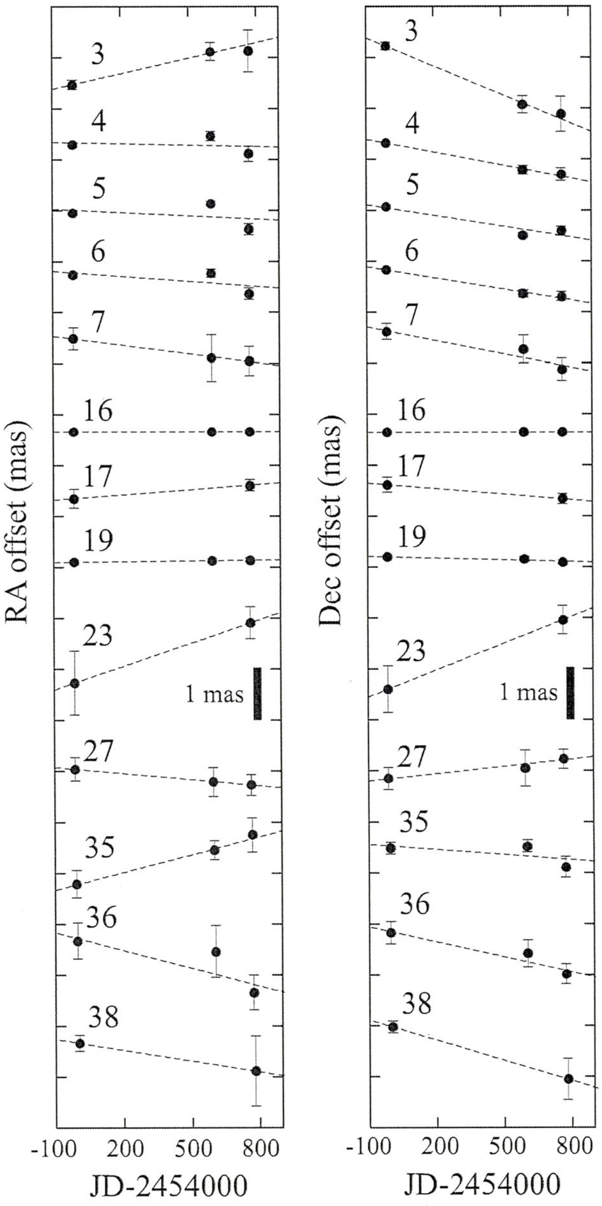

Figure 5-3: The positional variation in each direction (RA and Dec) of the methanol maser spots of ON 1 during the observation period. Numbers are the spot ID in table 5-2. The dash lines indicate a linear fit.

Table 5-2: Parameters of the 6.7 GHz methanol maser spots in ON 1 including information of the internal proper motion.

ID	LSR	Relative offset				Proper motion						Peak intensity		
	velocity	RA	σ_α	Dec	σ_δ	μ_α	$\sigma\mu_\alpha$	V_x	μ_δ	$\sigma\mu_\delta$	V_y	1st	2nd	3rd
	(km s^{-1})	(mas)				(mas yr^{-1})		(km s^{-1})	(mas yr^{-1})		(km s^{-1})	(Jy beam^{-1})		
(1)	(2)	(3)	(4)	(5)	(6)	(7)	(8)	(9)	(10)	(11)	(12)	(13)	(14)	(15)
							Cluster II							
1	14.77	−342.21	0.33	−897.43	0.24	...	...	...	...	...	...	0.42	...	...
2	14.59	−341.97	0.27	−897.83	0.18	...	...	...	...	...	...	1.67	...	...
3	14.94	−337.03	0.09	−879.56	0.08	0.31	0.11	3.76	−0.63	0.10	−7.68	3.57	4.69	2.88
4	14.77	−336.91	0.03	−880.29	0.03	−0.09	0.38	−1.05	−0.29	0.01	−3.53	12.37	14.69	14.20
5	14.59	−336.85	0.03	−880.68	0.02	−0.15	0.41	−1.84	−0.23	0.08	−2.76	15.77	17.20	26.31
6	14.41	−336.78	0.05	−880.93	0.03	−0.17	0.22	−2.13	−0.24	0.02	−2.98	7.79	8.23	18.51
7	14.24	−336.63	0.22	−881.16	0.16	−0.21	0.16	−2.55	−0.35	0.12	−4.30	1.37	1.59	5.14
8	15.12	−336.53	0.61	−879.99	0.41	...	...	...	...	...	...	0.42	...	...
							Cluster I							
9	−0.17	−3.52	0.34	−16.48	0.17	...	...	...	...	...	...	0.92	...	...
10	0.18	−3.48	0.36	−16.61	0.17	...	...	...	...	...	...	0.76	...	...
11	0.00	−3.29	0.30	−16.55	0.15	...	...	...	...	...	...	1.08	...	...
12	−0.70	−0.72	0.31	0.19	0.38	...	...	...	...	...	...	...	...	1.83
13	0.53	−0.61	0.26	0.60	0.18	...	...	...	...	...	...	0.74	2.08	1.77
14	0.36	−0.40	0.06	0.39	0.05	...	...	...	...	...	...	3.46	7.94	6.17
15	0.18	−0.21	0.02	0.18	0.02	...	...	...	...	...	...	9.19	18.83	17.85
16*	0.00	0.00	0.02	0.00	0.01	0.00	...	0.00	0.00	...	0.00	13.17	25.81	30.93
17	−0.52	0.07	0.19	−0.14	0.15	0.12	0.10	1.50	−0.13	0.08	−1.62	1.10	...	5.89
18	−0.17	0.22	0.02	−0.16	0.02	...	...	...	...	...	...	10.82	20.85	18.01
19	−0.35	0.39	0.04	−0.25	0.03	0.02	0.00	0.24	−0.04	0.02	−0.54	4.85	9.56	7.82
20	0.00	2.92	0.29	15.25	0.18	...	...	...	...	...	...	0.80	...	...
21	0.18	3.07	0.34	15.34	0.23	...	...	...	...	...	...	0.57	...	...

Table 5-2: Continued.

ID	LSR	Relative offset				Proper motion						Peak intensity		
	velocity	RA	σ_α	Dec	σ_δ	μ_α	$\sigma\mu_\alpha$	V_x	μ_δ	$\sigma\mu_\delta$	V_y	1st	2nd	3rd
	(km s^{-1})	(mas)				(mas yr^{-1})		(km s^{-1})	(mas yr^{-1})		(km s^{-1})	(Jy $beam^{-1}$)		
(1)	(2)	(3)	(4)	(5)	(6)	(7)	(8)	(9)	(10)	(11)	(12)	(13)	(14)	(15)
22	−0.17	3.39	0.31	15.05	0.16	...	...	...	...	...	...	0.72	...	...
23	1.06	5.88	0.63	40.63	0.46	0.55	0.33	6.77	0.64	0.25	7.81	0.42	...	0.94
24	0.88	6.54	0.43	40.73	0.32	...	...	...	...	...	...	...	...	0.66
25	1.06	7.79	0.45	−55.65	0.25	...	...	...	...	...	...	0.43	...	...
26	1.23	7.92	0.30	45.21	0.28	...	...	...	...	...	...	0.72	1.10	1.08
27	1.41	8.23	0.23	46.16	0.22	−0.15	0.14	−1.83	0.18	0.13	2.17	0.77	1.27	1.28
28	0.88	8.23	0.47	−55.85	0.27	...	...	...	...	...	...	0.39	...	...
29	1.06	8.51	0.59	43.02	0.43	...	...	...	...	...	...	0.49	...	...
30	1.59	8.57	0.43	46.19	0.41	...	...	...	...	...	...	0.38	...	...
						Cluster III								
31	14.41	63.44	0.29	−1015.34	0.23	...	...	...	...	...	...	...	1.55	7.81
32	14.24	63.76	0.33	−1015.13	0.32	...	...	...	...	...	...	...	1.13	4.60
33	14.59	64.04	0.17	−1014.96	0.12	...	...	...	...	...	...	...	3.35	5.32
34	14.59	67.34	0.29	−1014.07	0.13	...	...	...	...	...	...	2.35	3.19	...
35	14.41	67.56	0.27	−1013.99	0.12	0.45	0.17	5.52	−0.18	0.23	−2.15	2.62	3.21	6.21
36	14.24	69.02	0.35	−1013.80	0.22	−0.48	0.23	−5.85	−0.38	0.14	−4.63	1.01	1.09	4.03
37	14.77	73.07	0.65	−1011.05	0.28	...	...	...	...	...	...	1.20	...	...
38	14.41	75.09	0.16	−1009.99	0.12	−0.26	0.33	−3.19	−0.48	0.20	−5.90	2.18	...	3.93
39	14.59	76.10	0.57	−1009.41	0.26	...	...	...	...	...	...	1.07	...	...
40	14.24	78.06	0.41	−1008.45	0.19	...	...	...	...	...	...	0.98	...	...
41	14.41	79.29	0.41	−1008.61	0.30	...	...	...	...	...	...	0.62	...	...

Column 1: spot identification number (in RA order); Column 2: LSR velocity; Columns 3–6: relative positional offsets with respect to the reference maser spot and uncertainties in the first epoch; Columns 7–12: internal proper motions, fitting errors, and tangential velocities for the right ascension and declination directions, respectively; Columns 13–15: peak intensities at each epoch.

* Reference spot for relative position and velocity. The absolute coordinates of the spot are given in the text.

5.2 W75 N

5.2.1 Spatial Distributions

We detected 40 and 53 maser spots at epochs 1 and 2, respectively, while the number of independent spots are 62. The peak intensities of the spots ranged from ~1.2 to 30.7 Jy beam^{-1}, and the rms of the image noise (1 σ) in a line-free channel was 400 and 150 mJy beam^{-1}, respectively. Although the image noise are different between two epochs, the maser spots that could not be detected at first epoch are bright enough to detect at second epoch, and vice versa. These can be due to flux variations represented in total-power spectra (figure 5-4), which are especially shown for spectral features at $V_{\rm lsr}$ from 3.25 to 6.24 km $^{-1}$. They may be also a simple change of physically or/and excitation conditions in masing gases, which is called as "Christmas-tree effect". Parameters of each maser spot are summarized in table 5-3. The correlated flux accounted for 60–70% of the single-dish flux.

The spatial distribution of the 6.7 GHz methanol maser spots in W75 N at each epoch are shown in figure 5-4 with their spectra. The 40 and 53 spots detected at each epoch within an area of ~300 × 1000 mas^2 (~600 × 2000 AU^2) are plotted as dots with colors corresponding to $V_{\rm lsr}$. The origin of the map corresponds to the position of the reference spot with an LSR velocity of 7.30 km s^{-1}, whose absolute coordinates α(J2000.0) = $20^{\rm h}38^{\rm m}36^{\rm s}.417$ and δ(J2000.0) = $+42^\circ 37' 34''.85$ obtained by [163]Surcis et al. (2009). The reference spot is also used as a reference for internal proper motion. We define three clusters of maser spots as well as the EVN image obtained by [163]Surcis et al. (2009): the north (I: $0''.1$ west, $0''.4$ north), origin (II), and south (III: $0''.1$ west, $0''.5$ south) clusters. Cluster I had a radial-velocity range of $V_{\rm lsr}$ = 3.25 to 6.24 km s^{-1}, whereas the other two clusters had ranges of $V_{\rm lsr}$ = 6.77 to 7.65 and 9.05 to 9.76 km s^{-1} for clusters II and III, respectively. Cluster I, II, and III correspond to the identification A, B, and C defined by [163]Surcis et al (2009). We note that ID 61 and 62 spots are also included in cluster II, although these spots are separated ($0''.3$ south) from the main cluster located at the origin.

Cluster I shows an arched structure elongated in the northeast(NE)-southwest(SW) direction. The overall distribution also represents an arched or ellipse morphology elongated in the north-south direction. The ellipse structure shows a linear velocity gradient along the declination direction. This characteristic is shown in the spatial distribution of the hydroxyl masers associated with the VLA 1 ([154]Slysh et al. 2002; [152]Slysh et al. 2010) The size of these distribution is about $1''$ corresponding to 2000 AU, and the radial velocity range of the methanol maser ($3.25 \leq V_{\rm lsr} \leq 9.76$ km s^{-1}) is covered from that of the hydroxyl maser ($3.70 \leq V_{\rm lsr} \leq 12.45$ km s^{-1} refered from [154]Slysh et al. 2002). The water masers associated with the VLA 1 also show similar size of the spatial elongation, but the radial velocity is clearly shifted from those of the methanol and hydroxyl masers ($9.3 \leq V_{\rm lsr} \leq 21.9$ km s^{-1}: [168]Torrelles et al. 1997).

5.2.2 Internal Proper Motions

For W75 N, we have succeeded VLBI observations with the JVN in only two epochs, and 30 maser spots were identified within the LSR velocity resolution of 0.18 km s^{-1}. The 17 maser spots out of 30 identified spots moved significantly larger than fitting errors in both the right ascension and declination directions. The internal proper motions were measured by applying linear motion to the positional offsets on the timeline. The internal proper-motion vectors are shown in figure 5-5, and the results of the internal proper-motion measurements are described in table 5-3. We note that the proper motions in cluster II could be in only two spots identified as ID 50 (the reference spot) and 61.

As seen in figure 5-5, the internal proper motions were classified into two groups: maser spots in cluster I were smoothed in the cluster, and the spots in cluster III moved in roughly the west direction. The averaged tangential velocities were $(V_{\mathrm{I}x}, V_{\mathrm{I}y}) = (-0.3 \pm 1.9, 2.1 \pm 1.7)$ km s^{-1} for cluster I, and $(V_{\mathrm{III}x}, V_{\mathrm{III}y}) = (-4.4 \pm 0.8, 0.8 \pm 0.7)$ km s^{-1} for cluster III (east and north are positive). The difference of the tangential velocity in right ascension direction $V_{\mathrm{I}x} - V_{\mathrm{III}x}$ of 4.1 ± 2.0 km s^{-1} is roughly equal to the half value of the radial velocity range ~3.3 km s^{-1}, while the difference of those in declination direction $V_{\mathrm{I}y} - V_{\mathrm{III}y}$ of 1.3 ± 1.8 km s^{-1} is much smaller than the radial velocity range.

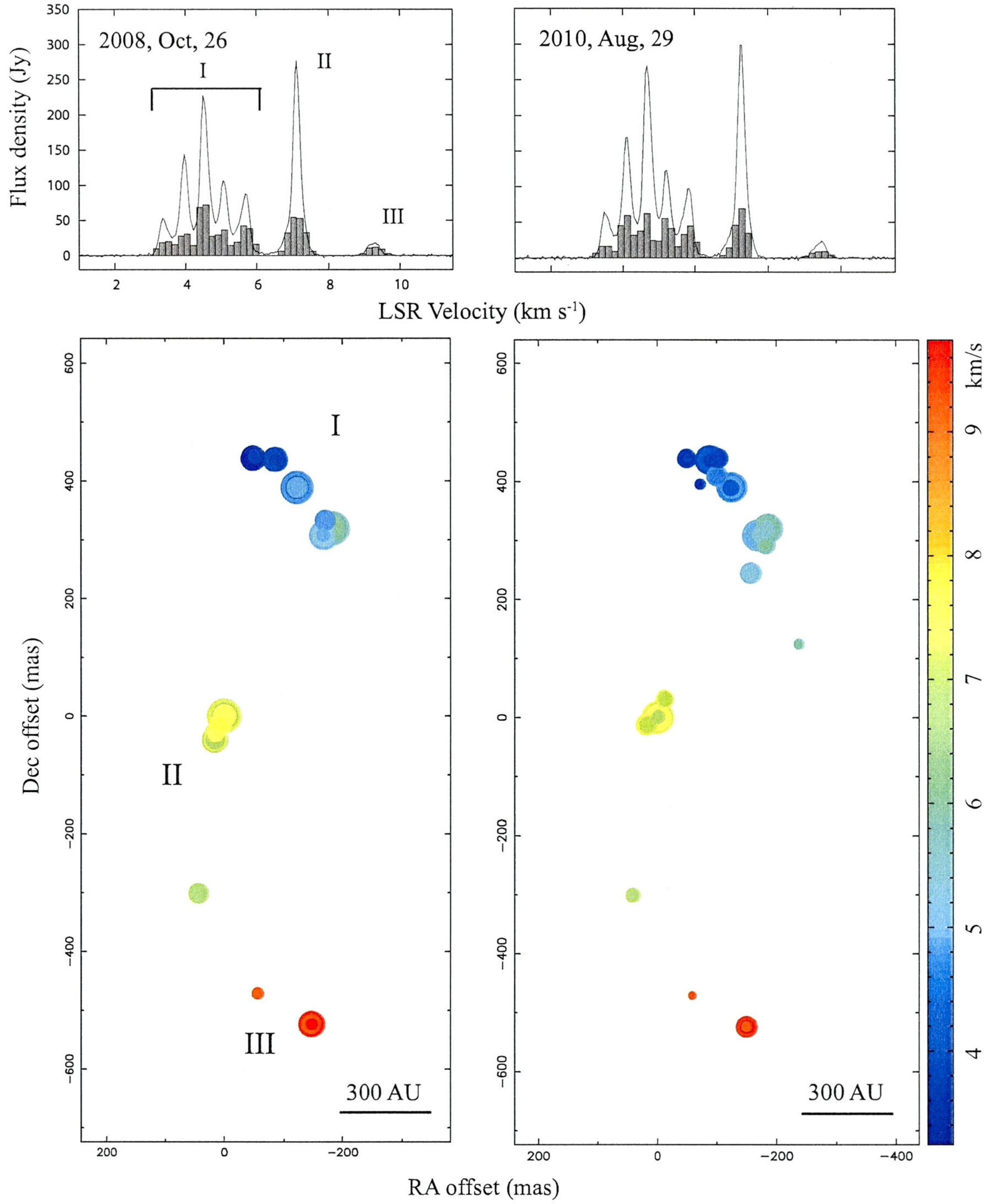

Figure 5-4: The 6.7 GHz methanol maser emissions in W75N. Left-panel:maser spectra (upper) and spatial distribution (lower) in the first epoch. In the spectra, filled block and solid curve is CLEANed component spectrum and total spectrum, repsectively. In the distribution, the spot size and color indicates its peak intensity in logarithmic scale and its radial velocity (see color index at the right), respectively. The labels I, II, and III indicate each maser cluster. The origin of this map corresponds to the absolute coordinate of the 6.7 GHz methanol maser (α(J2000.0) = $20^{h}38^{m}36^{s}.417$, δ(J2000.0) = $+42^{\circ}37'34''.85$) measured by [163]Surcis et al. (2009); Right-panel:same as left-panel but in the second epoch.

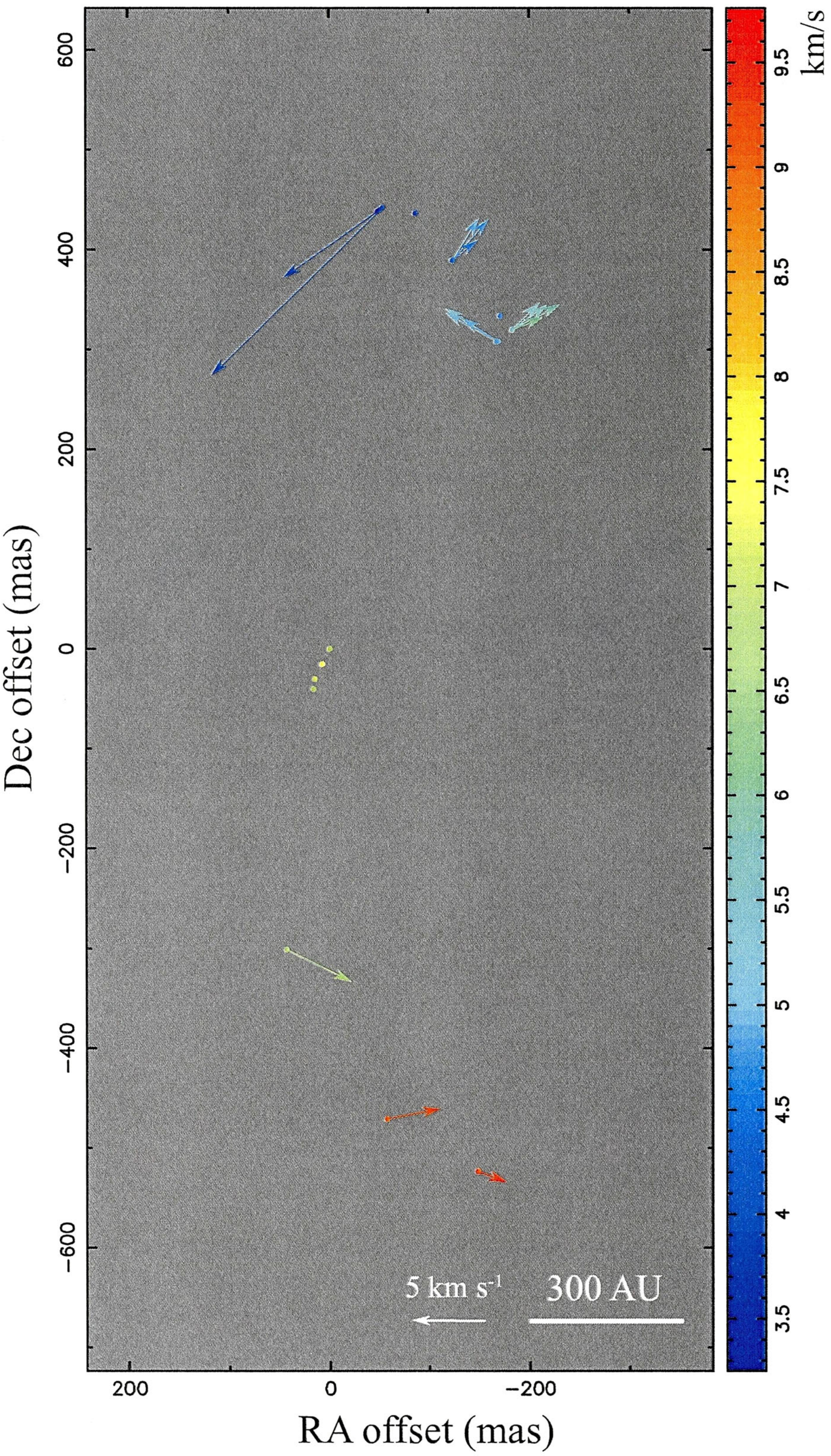

Figure 5-5: Internal proper motions of the 6.7 GHz methanol masers in W75 N. Arrows show proper motion of spots, and their lengths are proportional to the tangential velocities. The spatial and velocity scales are shown in the bottom. Filled circles show the methanol maser spots in a fixed scale. The displayed proper-motion vector is that subtracted by a velocity bias of the reference spot, $(\mu_\alpha, \mu_\delta) = (-0.18, +0.19)$ mas yr^{-1}, from the original vector to cancel out the average motions of all features.

Table 5-3: Parameters of the 6.7 GHz methanol maser spots in W75 N including information of the internal proper motion.

ID	Cluster	LSR	Relative offset				Proper motion						Peak intensity	
		velocity	RA	σ_α	Dec	σ_δ	μ_α	$\sigma\mu_\alpha$	V_x	μ_δ	$\sigma\mu_\delta$	V_y	1st	2nd
		(km s^{-1})	(mas)				(mas yr^{-1})		(km s^{-1})	(mas yr^{-1})		(km s^{-1})	(Jy $beam^{-1}$)	
(1)	(2)	(3)	(4)	(5)	(6)	(7)	(8)	(9)	(10)	(11)	(12)	(13)	(14)	(15)
1	I	6.07	−236.91	0.46	124.28	0.20	…	…	…	…	…	…	…	2.07
2	I	5.89	−236.42	0.42	124.44	0.18	…	…	…	…	…	…	…	3.12
3	I	6.24	−184.55	0.40	320.09	0.19	…	…	…	…	…	…	…	1.36
4	I	6.07	−183.59	0.17	319.59	0.14	−0.49	0.10	−4.63	0.32	0.08	3.05	11.68	9.51
5	I	5.89	−183.10	0.13	319.44	0.11	−0.66	0.08	−6.27	0.44	0.06	4.23	29.92	19.63
6	I	5.54	−183.00	0.19	319.85	0.14	−0.45	0.13	−4.32	0.46	0.09	4.38	12.46	5.43
7	I	5.71	−182.89	0.14	319.53	0.11	−0.53	0.08	−5.07	0.44	0.06	4.20	30.71	14.80
8	I	6.07	−181.50	0.24	292.88	0.13	…	…	…	…	…	…	…	3.44
9	I	5.89	−181.03	0.16	292.90	0.09	…	…	…	…	…	…	…	6.98
10	I	5.71	−180.62	0.16	292.94	0.08	…	…	…	…	…	…	…	5.88
11	I	5.54	−171.35	0.17	309.07	0.07	…	…	…	…	…	…	…	4.80
12	I	4.66	−170.71	0.70	333.65	0.66	…	…	…	…	…	…	7.75	…
13	I	4.48	−170.50	0.75	333.46	0.74	…	…	…	…	…	…	7.92	…
14	I	5.36	−168.96	0.19	307.85	0.14	0.35	0.12	3.32	0.52	0.08	4.98	9.68	16.52
15	I	5.19	−168.51	0.17	307.88	0.10	0.34	0.10	3.26	0.48	0.06	4.56	19.56	24.00
16	I	5.01	−167.62	0.18	307.94	0.10	0.17	0.12	1.62	0.42	0.06	4.03	14.82	13.50
17	I	4.84	−167.03	0.49	307.93	0.37	…	…	…	…	…	…	4.00	…
18	I	5.36	−155.65	0.31	244.62	0.07	…	…	…	…	…	…	…	6.39
19	I	5.19	−155.64	0.27	244.65	0.07	…	…	…	…	…	…	…	8.67
20	III	9.76	−148.37	0.22	−523.94	0.28	…	…	…	…	…	…	3.12	3.73
21	III	9.58	−148.13	0.10	−523.84	0.11	−0.47	0.07	−4.44	0.08	0.06	0.75	10.33	8.54
22	III	9.40	−148.01	0.08	−523.59	0.09	−0.47	0.06	−4.47	0.08	0.05	0.74	13.77	7.90
23	III	9.23	−147.87	0.12	−523.28	0.13	…	…	…	…	…	…	7.27	3.11

Table 5-3: Continued.

ID	Cluster	LSR	Relative offset				Proper motion						Peak intensity	
		velocity	RA	σ_α	Dec	σ_δ	μ_α	$\sigma\mu_\alpha$	V_x	μ_δ	$\sigma\mu_\delta$	V_y	1st	2nd
		(km s^{-1})	(mas)				(mas yr^{-1})		(km s^{-1})	(mas yr^{-1})		(km s^{-1})	(Jy beam^{-1})	
(1)	(2)	(3)	(4)	(5)	(6)	(7)	(8)	(9)	(10)	(11)	(12)	(13)	(14)	(15)
24	I	4.84	−123.20	0.38	389.28	0.34	−0.45	0.23	−4.27	0.61	0.19	5.84	7.96	9.81
25	I	4.66	−122.87	0.18	389.12	0.20	−0.55	0.11	−5.22	0.60	0.11	5.74	22.69	20.27
26	I	4.48	−122.61	0.16	389.11	0.18	−0.45	0.10	−4.24	0.39	0.10	3.75	26.67	13.18
27	I	4.31	−122.58	0.24	389.19	0.27	…	…	…	…	…	…	10.23	5.18
28	I	4.13	−101.47	0.24	439.65	0.20	…	…	…	…	…	…	…	6.93
29	I	3.96	−101.35	0.28	439.84	0.24	…	…	…	…	…	…	…	4.98
30	I	4.48	−99.72	0.19	408.75	0.19	…	…	…	…	…	…	…	4.58
31	I	4.66	−99.53	0.21	409.36	0.19	…	…	…	…	…	…	…	7.93
32	I	4.31	−87.08	0.12	437.36	0.11	…	…	…	…	…	…	…	9.02
33	I	4.13	−86.23	0.23	436.52	0.28	…	…	…	…	…	…	11.57	17.91
34	I	3.96	−86.10	0.22	436.64	0.26	…	…	…	…	…	…	11.48	13.86
35	I	3.78	−86.02	0.40	436.52	0.56	…	…	…	…	…	…	3.40	3.51
36	I	3.25	−71.75	0.37	395.35	0.29	…	…	…	…	…	…	…	1.52
37	I	3.43	−71.52	0.27	395.60	0.22	…	…	…	…	…	…	…	3.10
38	I	3.61	−71.47	0.29	395.49	0.24	…	…	…	…	…	…	…	3.05
39	III	9.05	−57.25	0.27	−470.91	0.30	…	…	…	…	…	…	2.70	1.16
40	III	9.23	−57.23	0.24	−471.16	0.36	−0.72	0.21	−6.86	0.29	0.22	2.80	3.46	2.39
41	I	3.78	−53.18	0.38	442.11	0.41	1.54	0.23	14.65	−1.50	0.23	−14.26	4.20	2.73
42	I	3.61	−50.53	0.35	439.98	0.31	0.79	0.21	7.57	−0.50	0.17	−4.74	8.00	5.80
43	I	3.43	−48.88	0.18	438.70	0.16	…	…	…	…	…	…	12.31	6.70
44	I	3.25	−48.42	0.23	438.46	0.22	…	…	…	…	…	…	6.80	3.04
45	II	7.12	−12.59	0.22	30.94	0.19	…	…	…	…	…	…	…	4.56
46	II	7.30	−12.02	0.25	30.95	0.21	…	…	…	…	…	…	…	6.71
47	II	6.94	−0.33	0.15	0.22	0.16	…	…	…	…	…	…	13.36	4.18
48	II	7.47	−0.16	0.29	0.12	0.27	…	…	…	…	…	…	10.02	15.08

Table 5-3: Continued.

ID	Cluster	LSR	Relative offset				Proper motion						Peak intensity	
		velocity	RA	σ_α	Dec	σ_δ	μ_α	$\sigma\mu_\alpha$	V_x	μ_δ	$\sigma\mu_\delta$	V_y	1st	2nd
		(km s^{-1})	(mas)				(mas yr^{-1})		(km s^{-1})	(mas yr^{-1})		(km s^{-1})	(Jy $beam^{-1}$)	
(1)	(2)	(3)	(4)	(5)	(6)	(7)	(8)	(9)	(10)	(11)	(12)	(13)	(14)	(15)
49	II	7.12	−0.13	0.12	0.08	0.13	...	...	...	...	...	...	30.55	18.35
50*	II	7.30	0.00	0.15	0.00	0.15	0.00	0.09	0.00	0.00	0.09	0.00	27.70	27.46
51	II	7.47	6.79	0.33	−14.85	0.37	...	...	...	...	...	...	9.13	...
52	II	7.65	7.31	0.25	−15.33	0.30	...	...	...	...	...	...	4.25	...
53	II	7.30	14.32	0.35	−30.22	0.35	...	...	...	...	...	...	9.92	...
54	II	7.47	14.44	0.39	−29.91	0.44	...	...	...	...	...	...	5.58	...
55	II	7.30	15.66	0.30	−40.25	0.39	...	...	...	...	...	...	10.26	...
56	II	7.12	15.68	0.20	−39.99	0.27	...	...	...	...	...	...	14.27	...
57	II	6.94	15.84	0.22	−40.07	0.29	...	...	...	...	...	...	6.86	...
58	II	7.12	18.69	0.18	−12.51	0.12	...	...	...	...	...	...	...	5.46
59	II	7.30	19.26	0.17	−12.22	0.12	...	...	...	...	...	...	...	8.98
60	II	7.47	20.02	0.13	−12.07	0.09	...	...	...	...	...	...	...	6.21
61	II	6.77	42.74	0.17	−301.12	0.15	−0.83	0.14	−7.86	−0.13	0.11	−1.27	5.81	2.77
62	II	6.94	43.06	0.23	−301.08	0.23	...	...	...	...	...	...	8.03	4.49

Column 1: spot identification number (in RA order); Column 2: cluster number associated with each maser spot; Column 3: LSR velocity; Columns 4–7: relative positional offsets with respect to the reference maser spot and uncertainties in the first epoch; Columns 8–13: internal proper motions, fitting errors, and tangential velocities for the right ascension and declination directions, respectively; Columns 14–15: peak intensities at each epoch.

* Reference spot for relative position and velocity. The absolute coordinates of the spot are given in the text.

5.3 Cep A

5.3.1 Spatial Distributions

We detected 98, 97, and 72 maser spots at epochs 1, 2, and 3, respectively, while the number of independent spots are 158. The peak intensities of the spots ranged from ~0.4 to 92.2 Jy beam^{-1}, and the rms of the image noise (1 σ) in a line-free channel was 80, 100, and 110 mJy beam^{-1}, respectively. Given approximately same image sensitivities in each observational epoch, differences of detection rate for the maser spots in each epoch could be due to the variation of flux densities. The 6.7 GHz methanol maser spectral features have been well known to represent dramatically flux variation in the short period of ~30 days ([161]Sugiyama et al. 2008b). Actually, there were clearly flux variations during the spanning 776 days, as shown in figure 5-6 (left-panel). The flux densities of the spectral features I and II have decreased from the first epoch to the third epoch, while ones of the features III, IV, and V have increased during the same period. They may be also due to the Christmas-tree effect as same as the case in W75 N. Parameters of each maser spot are summarized in table 5-4. The maser emissions were detected even with longer baselines, and the correlated flux accounted for over 80% of the single-dish flux.

The spatial distribution of the 6.7 GHz methanol maser spots in Cep A at each epoch are shown in figure 5-6 with their spectra. The absolute coordinates of the spot at −2.64 km s^{-1} obtained in our observation are α(J2000.0) = $22^{\mathrm{h}}56^{\mathrm{m}}17^{\mathrm{s}}.9042$, δ(J2000.0) = $+62^{\circ}01'49''.577$, with errors less than 1 mas. This is the origin of the image. The methanol maser spots in Cep A formed isolated clusters as well as the separated features in the spectrum. The cluster of the spots locating near the origin of the VLBI map corresponds to the spectral features I and II, and a cluster locating at $0''.45$ east, $0''.10$ south from the origin corresponds to the feature II. The correspondences of the other clusters and the spectral features are as follows; the western cluster ($0''.30$ west, $0''.20$ north) is III, the eastern cluster ($1'.35$ east, $0''.20$ south) is IV, and the northern cluster ($0''.10$ east, $0''.50$ north) is V, respectively. The clusters II ($0'.45$ east, $0''.10$ south) and V were dicovered in the VLBI image as same as the ones by [172]Torstensson et al. (2010). Some weak spots with radial velocities from −0.53 to −0.36 km s^{-1}, which are a part of the cluster II, were detected only in the VLBI observation, and not detected in the spectral observation with Yamaguchi 32-m telescope. The red-shifted (I, II) and the blue-shifted features (III, IV, V) are isolated in the spatial distribution by more than 100 AU, and the red-shifted features are surrounded by the blue-shifted features.

The spatial distribution of the spots in Cep A showed an arched structure, and the size from edge to edge of the arclike structure is ~1900 mas or ~1400 AU at a distance of 0.70 kpc. The peak of 43 GHz continuum emission, which may be an exciting source ([37]Curiel et al. 2006), located near the center of the arclike structure of the 6.7 GHz methanol maser spots. The elongation of the arched structure is nearly perpendicular to the radio jet. The overall distribution of the maser spots coincide with the CH_3CN and NH_3 disks ([129]Patel et al. 2005; [169]Torrelles et al. 2007) and the velocity range of the spots is similar to that of these disks, although a simple velocity gradient was not detected with the maser spots. The water maser disk reported by [167]Torrelles et al. (1996) locates almost the same position with the methanol arched structure, although the size of the water maser disk is about 2 times smaller. The ground-state hydroxyl masers around the HW2 object ([113]Migenes et al. 1992; [6]Bartkiewicz et al. 2005b), whose internal proper motions were mainly directed away from the central source, are distributed surrounding the methanol maser distribution, as introduced in section 3.3. The radial velocities of both masers (water: −27.3 to +8.9 km s^{-1}; hydroxyl: −25.2 to −0.6 km s^{-1}) cover the range of the methanol maser (−4.93 to −0.36 km s^{-1}).

5.3.2 Internal Proper Motions

Maser spots detected in different epochs were identified as the same if their LSR velocities coincided within the velocity resolution of 0.18 km s^{-1} and their positions were within 6.4 mas at the first to third epochs (corresponding to a two times transversal velocity of $\sim$10 km s^{-1} at 0.70 kpc, almost equivalent to two times of the range of the radial velocity). On the basis of these criteria, 35 maser spots were identified at all three epochs, 19 spots were indentified at the first and the second epochs, four spots were identified at the first and the third epochs, and 13 spots were identified at the second and the third epochs. The motions of 46 maser spots out of 71 identified spots were significantly larger than the relative positional uncertainties during the observation period in both the right ascension and declination directions. The internal proper-motion vectors are shown in figure 5-7, and the positional variations of each maser spot are shown in figure 5-8 and 5-9. The internal proper motions were measured by applying linear motion to the positional offsets on the timeline. The results of the internal proper-motion measurements are also shown in table 5-4. We note that the proper motions in cluster II ($0''.45$ east, $0''.10$ south) could be in only one spot identified as ID 111.

As seen in figure 5-7, the internal proper motions in Cep A showed various vector in each maser cluster. The motions in cluster I and II, which locates near the origin of the map, are especially random shown in figure 5-7(c). The averaged tangential velocities were $(V_{\mathrm{I,II}x}, V_{\mathrm{I,II}y}) = (+2.0 \pm 0.7, -0.2 \pm 0.4)$ km s^{-1} for cluster I and II (locating near the origin), $(V_{\mathrm{III}x}, V_{\mathrm{III}y}) = (+4.4 \pm 0.5, +1.8 \pm 0.2)$ km s^{-1} for cluster III, $(V_{\mathrm{IV}x}, V_{\mathrm{IV}y}) = (-1.0 \pm 1.1, -1.2 \pm 0.6)$ km s^{-1} for cluster IV, and $(V_{\mathrm{V}x}, V_{\mathrm{V}y}) = (+3.2 \pm 1.0, -3.3 \pm 1.7)$ km s^{-1} for cluster V (east and north are positive). The internal proper motions including all of clusters were along the arched structure of the 6.7 GHz methanol maser itself, which was basically perpendicular to the radio continuum jet.

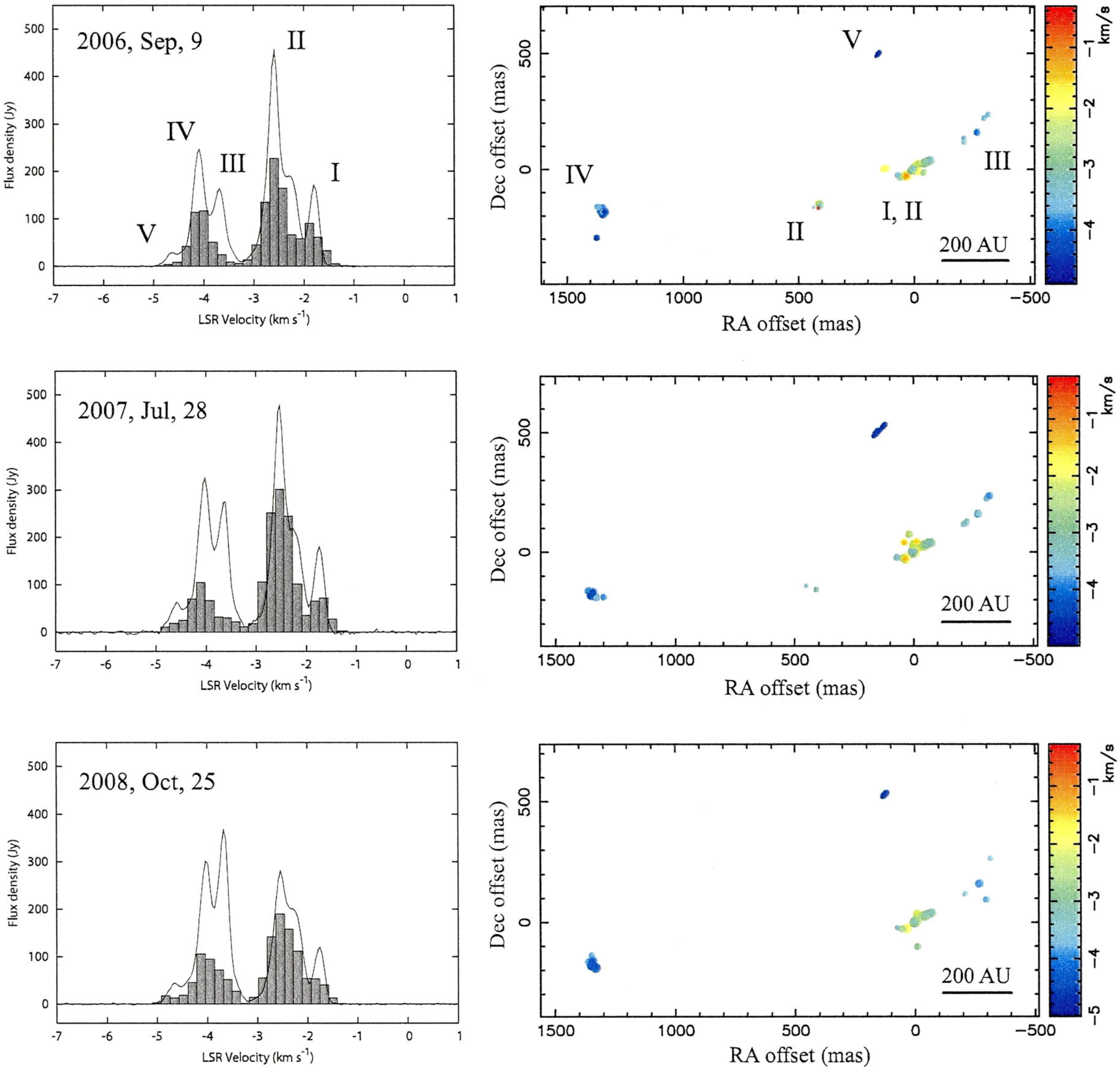

Figure 5-6: The 6.7 GHz methanol maser emissions in Cep A. Upper-panel:maser spectra (left) and spatial distribution (right) in the first epoch. In the spectra, filled block and solid curve is CLEANed component spectrum and total spectrum, repsectively. In the distribution, the spot size and color indicates its peak intensity in logarithmic scale and its radial velocity (see color index at the right), respectively. The labels I–V indicate each maser cluster. The origin of this map corresponds to the absolute coordinate of the 6.7 GHz methanol maser ($\alpha(\mathrm{J2000.0}) = 22^{\mathrm{h}}56^{\mathrm{m}}17^{\mathrm{s}}.9042$, $\delta(\mathrm{J2000.0}) = +62^{\circ}01'49''.577$) obtained by our observation; Middle-panel:same as upper-panel but in the second epoch; Lower-panel:same as upper-panel but in the third epoch.

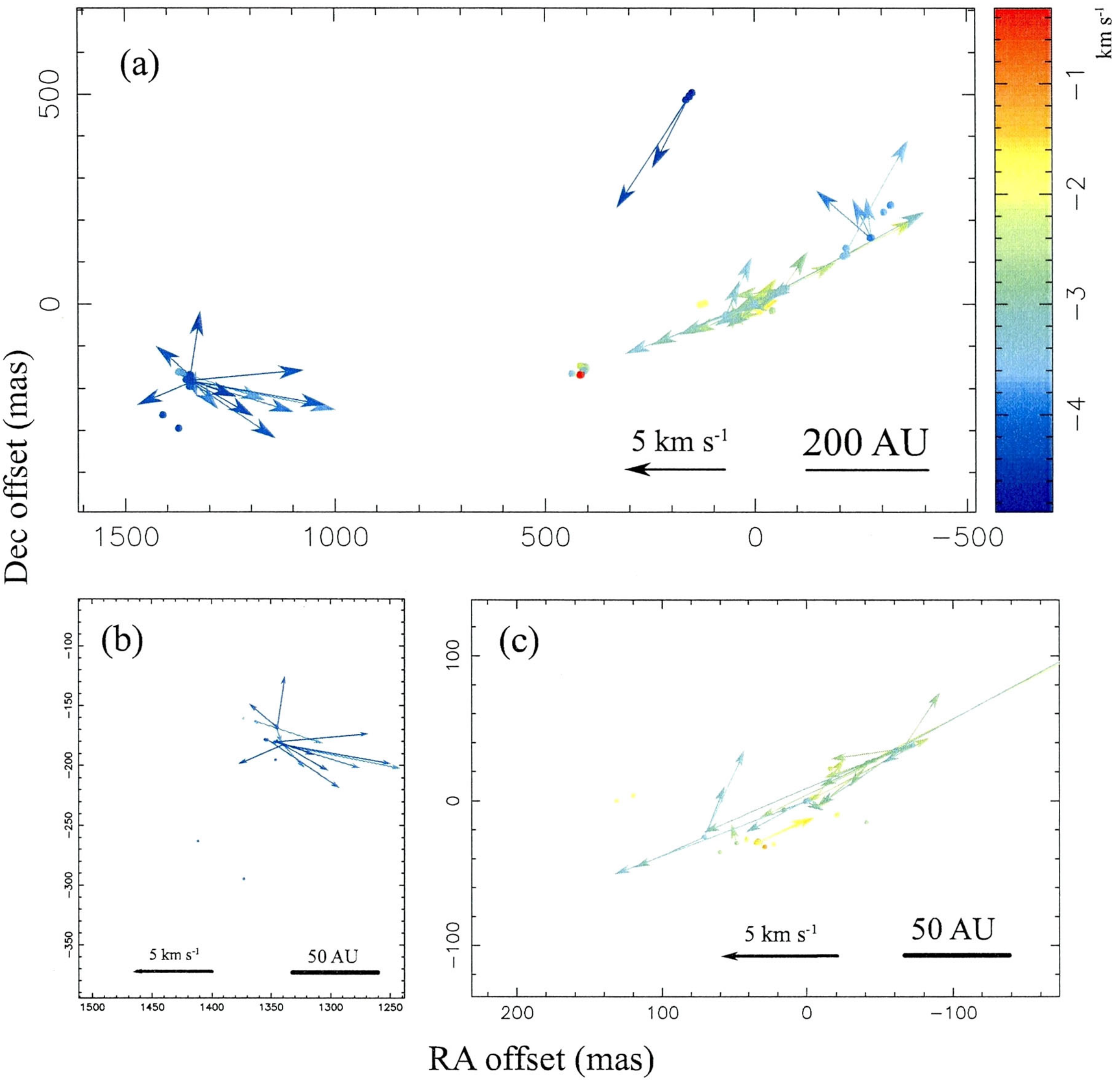

Figure 5-7: (a) Internal proper motions of the 6.7 GHz methanol masers in Cep A. Arrows show proper motion of spots, and their lengths are proportional to the tangential velocities. The spatial and velocity scales are shown in the lower corner. Filled circles show the methanol maser spots in a fixed scale. The displayed proper-motion vector is that subtracted by a velocity bias of the reference spot, $(\mu_\alpha, \mu_\delta) = (+0.46, -0.18)$ mas yr^{-1}, from the original vector to cancel out the average motions of all features. (b),(c) Blow-up figures of cluster IV and I,II, respectively.

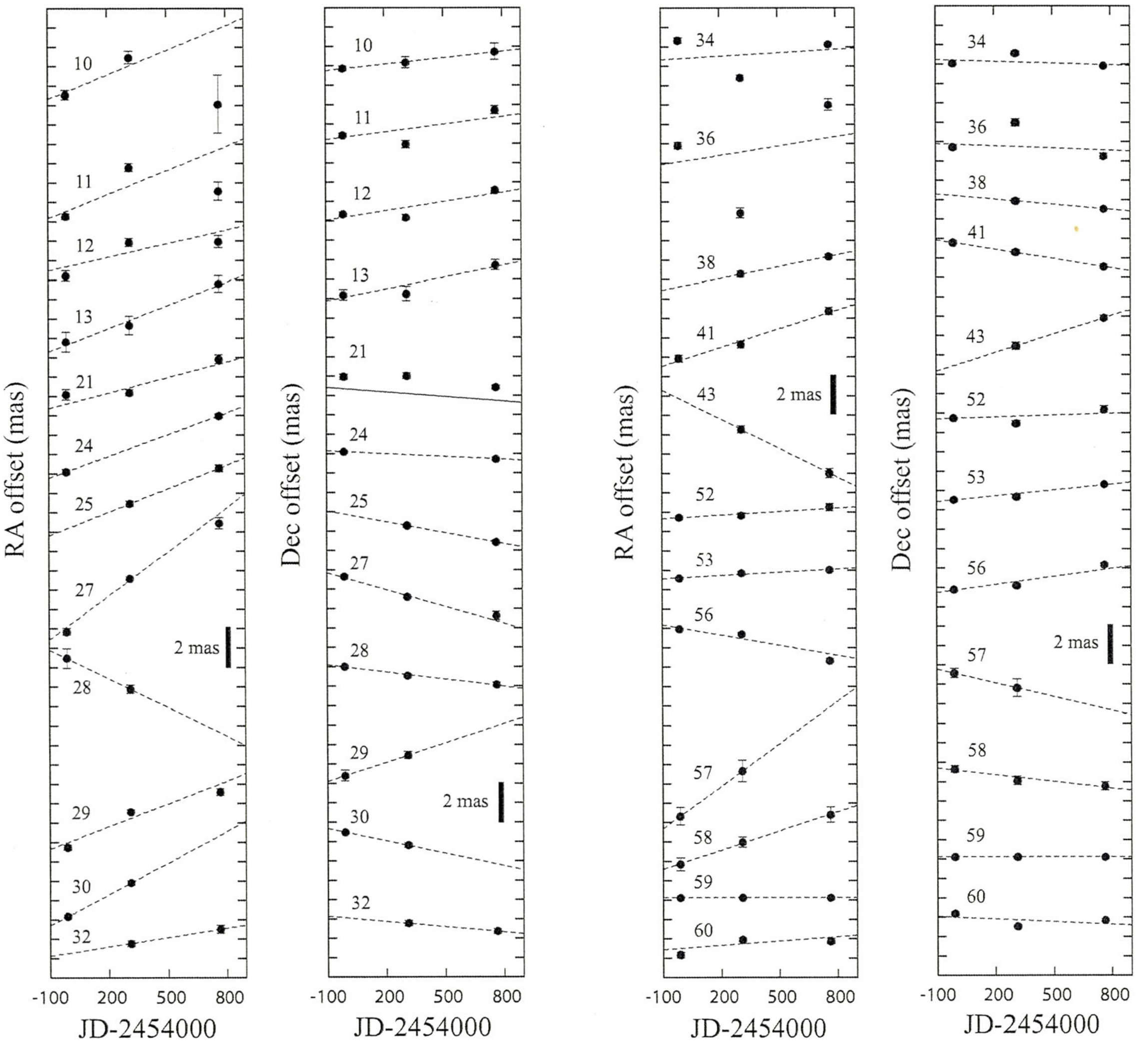

Figure 5-8: The positional variation in each direction (RA and Dec) of the methanol maser spots of Cep A during the observation period. Numbers are the spot ID in table 5-4. The dash lines indicate a linear fit.

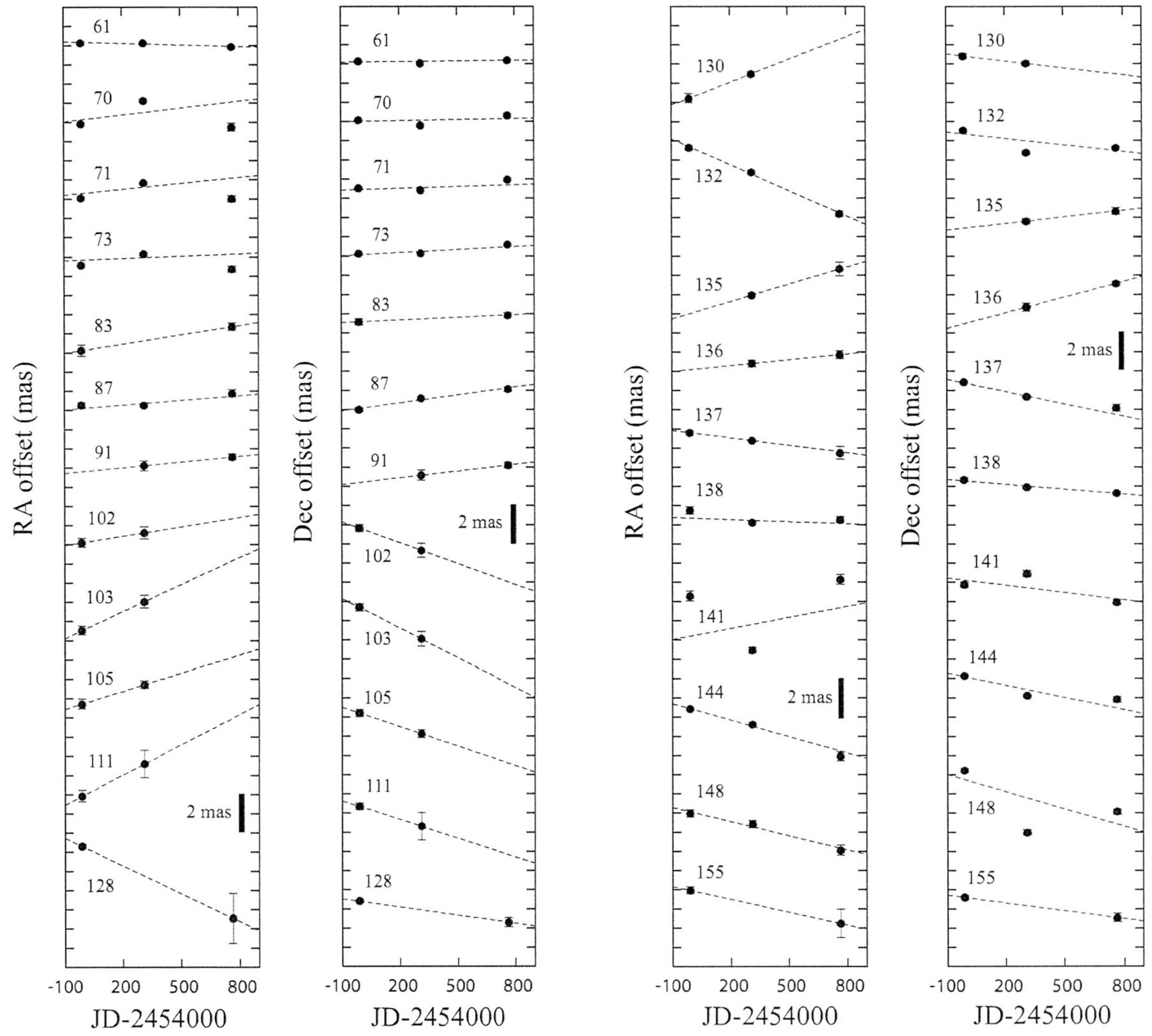

Figure 5-9: Continued from fig 5-8.

Table 5-4: Parameters of the 6.7 GHz methanol maser spots in Cep A including information of the internal proper motion.

ID	Cluster	LSR velocity (km s^{-1})	Relative offset				Proper motion						Peak intensity		
			RA	σ_α	Dec	σ_δ	μ_α	$\sigma\mu_\alpha$	V_x	μ_δ	$\sigma\mu_\delta$	V_y	1st	2nd	3rd
			(mas)				(mas yr^{-1})		(km s^{-1})	(mas yr^{-1})		(km s^{-1})	(Jy beam^{-1})		
(1)	(2)	(3)	(4)	(5)	(6)	(7)	(8)	(9)	(10)	(11)	(12)	(13)	(14)	(15)	(16)
1	III	−3.87	−320.49	0.68	237.24	0.46	...	...	...	...	...	...	1.45	7.16	...
2	III	−3.69	−319.99	0.41	236.96	0.31	...	...	...	...	...	...	2.10	7.51	...
3	III	−3.52	−319.45	0.45	236.78	0.34	...	...	...	...	...	...	1.40	3.55	...
4	III	−4.05	−317.90	0.59	234.75	0.49	...	...	...	...	...	...	...	2.72	...
5	III	−3.52	−314.99	0.91	265.70	0.33	...	...	...	...	...	...	...	...	1.96
6	III	−3.52	−303.73	0.40	220.89	0.32	...	...	...	...	...	...	1.33	...	...
7	III	−3.69	−303.30	0.30	220.80	0.19	...	...	...	...	...	...	2.13	3.26	...
8	III	−3.87	−299.02	0.74	94.65	0.30	...	...	...	...	...	...	...	...	3.50
9	III	−3.69	−298.73	0.86	94.70	0.34	...	...	...	...	...	...	...	...	3.53
10	III	−3.52	−274.34	0.25	160.71	0.13	1.55	0.40	5.16	0.40	0.19	1.35	2.64	1.90	2.42
11	III	−3.69	−273.89	0.14	160.43	0.10	1.48	0.19	4.94	0.47	0.11	1.58	5.60	6.30	8.32
12	III	−3.87	−273.22	0.26	159.77	0.11	0.84	0.20	2.81	0.58	0.08	1.94	4.79	8.40	10.41
13	III	−4.05	−271.77	0.51	158.62	0.27	1.45	0.31	4.82	0.74	0.18	2.47	2.30	3.83	8.02
14	III	−3.34	−225.53	0.51	132.59	0.52	...	...	...	...	...	...	...	1.01	...
15	III	−3.52	−224.40	0.40	129.49	0.45	...	...	...	...	...	...	...	1.88	...
16	III	−3.52	−216.10	0.27	119.06	0.16	...	...	...	...	...	...	2.21	3.83	...
17	III	−3.69	−214.79	0.41	134.94	0.24	...	...	...	...	...	...	1.61	4.96	...
18	III	−3.34	−214.45	0.23	119.65	0.15	...	...	...	...	...	...	1.46	1.53	...
19	III	−3.34	−209.55	0.33	117.36	0.33	...	...	...	...	...	...	...	1.43	...
20	III	−3.52	−208.87	0.21	115.73	0.22	...	...	...	...	...	...	...	2.59	2.15
21	I, II	−3.17	−72.49	0.27	38.53	0.14	0.97	0.16	3.22	−0.29	0.08	−0.96	2.08	3.74	3.18
22	I, II	−2.99	−71.69	0.11	37.99	0.05	...	...	...	...	...	...	10.04	11.73	9.71
23	I, II	−2.82	−70.24	0.13	37.35	0.07	...	...	...	...	...	...	16.92	13.94	8.59

Table 5-4: Continued.

ID	Cluster	LSR	Relative offset				Proper motion						Peak intensity		
		velocity	RA	σ_α	Dec	σ_δ	μ_α	$\sigma\mu_\alpha$	V_x	μ_δ	$\sigma\mu_\delta$	V_y	1st	2nd	3rd
		(km s^{-1})	(mas)				(mas yr^{-1})		(km s^{-1})	(mas yr^{-1})		(km s^{-1})	(Jy beam^{-1})		
(1)	(2)	(3)	(4)	(5)	(6)	(7)	(8)	(9)	(10)	(11)	(12)	(13)	(14)	(15)	(16)
24	I, II	−2.64	−68.47	0.12	36.38	0.06	1.36	0.07	4.52	−0.17	0.04	−0.58	13.36	···	11.69
25	I, II	−2.99	−67.42	0.14	37.00	0.09	1.47	0.18	4.89	−0.68	0.10	−2.27	···	12.22	8.40
26	I, II	−2.82	−65.30	0.19	35.43	0.15	···	···	···	···	···	···	···	19.11	13.72
27	I, II	−2.99	−61.87	0.17	35.37	0.09	2.75	0.15	9.18	−1.05	0.10	−3.51	6.97	14.15	4.93
28	I, II	−2.82	−60.54	0.12	34.43	0.06	1.41	0.10	4.71	−0.45	0.06	−1.49	19.02	31.03	9.13
29	I, II	−3.17	−60.41	0.50	34.83	0.28	−1.79	0.61	−5.96	1.21	0.38	4.04	1.12	2.74	···
30	I, II	−2.64	−59.37	0.08	33.63	0.03	1.98	0.15	6.61	−0.77	0.13	−2.57	22.60	26.64	···
31	I, II	−2.46	−59.25	0.26	33.52	0.11	···	···	···	···	···	···	9.87	···	···
32	I, II	−2.99	−48.20	0.15	28.78	0.14	0.59	0.20	1.96	−0.33	0.15	−1.10	···	7.55	6.29
33	I, II	−3.17	−47.33	0.48	37.66	0.39	···	···	···	···	···	···	···	···	1.11
34	I, II	−2.82	−46.39	0.15	28.04	0.08	0.22	0.08	0.72	−0.11	0.04	−0.38	13.59	25.88	18.06
35	I, II	−2.64	−45.23	0.06	27.48	0.03	···	···	···	···	···	···	24.24	34.45	25.46
36	I, II	−2.46	−44.96	0.17	27.57	0.09	0.59	0.15	1.97	−0.13	0.08	−0.42	17.14	12.80	14.29
37	I, II	−2.29	−42.58	0.19	20.50	0.16	···	···	···	···	···	···	···	···	9.00
38	I, II	−2.82	−42.18	0.16	26.38	0.12	0.74	0.16	2.47	−0.32	0.11	−1.07	···	19.93	15.09
39	I, II	−2.64	−40.79	0.09	25.79	0.07	···	···	···	···	···	···	···	35.11	25.68
40	I, II	−2.64	−40.78	0.28	−14.42	0.14	···	···	···	···	···	···	3.89	···	···
41	I, II	−2.46	−40.37	0.18	25.80	0.09	1.17	0.13	3.91	−0.58	0.07	−1.93	14.22	21.52	18.62
42	I, II	−2.46	−34.91	0.20	23.20	0.16	···	···	···	···	···	···	···	17.96	···
43	I, II	−2.29	−34.73	0.18	22.63	0.19	−1.81	0.24	−6.03	1.16	0.18	3.88	···	15.54	9.31
44	I, II	−2.29	−28.73	0.29	28.04	0.16	···	···	···	···	···	···	···	···	6.65
45	I, II	−2.11	−21.21	0.19	−8.92	0.10	···	···	···	···	···	···	10.22	···	···
46	I, II	−1.94	−19.97	0.23	−9.64	0.13	···	···	···	···	···	···	7.57	···	···
47	I, II	−2.29	−15.72	0.28	22.18	0.15	···	···	···	···	···	···	8.19	···	···
48	I, II	−1.76	−13.36	0.45	44.29	0.43	···	···	···	···	···	···	···	2.78	···

Table 5-4: Continued.

ID	Cluster	LSR	Relative offset				Proper motion						Peak intensity		
		velocity	RA	σ_α	Dec	σ_δ	μ_α	$\sigma\mu_\alpha$	V_x	μ_δ	$\sigma\mu_\delta$	V_y	1st	2nd	3rd
		(km s^{-1})	(mas)				(mas yr^{-1})		(km s^{-1})	(mas yr^{-1})		(km s^{-1})	(Jy beam^{-1})		
(1)	(2)	(3)	(4)	(5)	(6)	(7)	(8)	(9)	(10)	(11)	(12)	(13)	(14)	(15)	(16)
49	I, II	−1.59	−13.02	0.51	44.62	0.49	⋯	⋯	⋯	⋯	⋯	⋯	⋯	1.18	⋯
50	I, II	−2.82	−10.77	0.38	−101.54	0.18	⋯	⋯	⋯	⋯	⋯	⋯	⋯	⋯	4.34
51	I, II	−2.29	−7.39	0.25	33.86	0.14	⋯	⋯	⋯	⋯	⋯	⋯	⋯	⋯	7.72
52	I, II	−2.11	−6.27	0.07	3.04	0.04	0.22	0.09	0.74	0.11	0.07	0.37	24.59	21.44	15.12
53	I, II	−2.29	−5.41	0.05	2.56	0.03	0.20	0.04	0.68	0.37	0.03	1.22	46.03	48.59	35.85
54	I, II	−2.64	−4.74	0.04	2.90	0.03	⋯	⋯	⋯	⋯	⋯	⋯	⋯	⋯	27.33
55	I, II	−1.94	−4.10	0.19	2.39	0.11	⋯	⋯	⋯	⋯	⋯	⋯	8.70	⋯	⋯
56	I, II	−2.46	−2.04	0.04	0.91	0.02	−0.62	0.05	−2.08	0.51	0.03	1.68	63.74	73.17	45.07
57	I, II	−3.34	−0.94	0.46	0.31	0.24	2.65	0.82	8.82	−0.86	0.58	−2.86	0.85	0.93	⋯
58	I, II	−3.17	−0.57	0.33	0.68	0.17	1.21	0.24	4.02	−0.41	0.13	−1.38	1.75	2.25	1.53
59*	I, II	−2.64	0.00	0.02	0.00	0.01	0.00	0.02	0.00	0.00	0.01	0.00	68.78	92.19	46.06
60	I, II	−2.99	0.88	0.15	0.07	0.07	0.27	0.09	0.90	−0.15	0.05	−0.50	7.61	13.78	8.82
61	I, II	−2.82	0.99	0.07	−0.29	0.03	−0.10	0.04	−0.32	0.04	0.02	0.12	36.96	55.84	29.14
62	I, II	−2.29	1.27	0.39	30.90	0.34	⋯	⋯	⋯	⋯	⋯	⋯	⋯	9.26	⋯
63	I, II	−2.82	15.43	0.47	−5.97	0.27	⋯	⋯	⋯	⋯	⋯	⋯	5.23	⋯	⋯
64	I, II	−2.64	16.35	0.25	−6.69	0.14	⋯	⋯	⋯	⋯	⋯	⋯	6.12	⋯	⋯
65	I, II	−2.46	18.38	0.48	73.28	0.49	⋯	⋯	⋯	⋯	⋯	⋯	⋯	7.06	⋯
66	I, II	−1.94	22.73	0.23	−29.73	0.12	⋯	⋯	⋯	⋯	⋯	⋯	8.41	⋯	⋯
67	I, II	−1.23	29.20	0.75	−31.63	0.46	⋯	⋯	⋯	⋯	⋯	⋯	0.43	⋯	⋯
68	I, II	−1.06	32.44	0.86	−28.53	0.49	⋯	⋯	⋯	⋯	⋯	⋯	0.37	⋯	⋯
69	I, II	−2.11	32.77	0.24	−28.11	0.14	⋯	⋯	⋯	⋯	⋯	⋯	6.79	8.58	8.96
70	I, II	−1.94	32.93	0.07	−28.36	0.04	0.43	0.09	1.44	0.07	0.04	0.22	25.63	28.96	18.07
71	I, II	−1.76	33.61	0.07	−28.61	0.03	0.38	0.07	1.26	0.12	0.04	0.41	34.02	33.90	17.00
72	I, II	−1.23	33.62	0.37	−27.30	0.21	⋯	⋯	⋯	⋯	⋯	⋯	0.87	⋯	⋯
73	I, II	−1.59	34.14	0.08	−28.72	0.04	0.15	0.08	0.48	0.18	0.04	0.61	18.96	13.93	5.97

Table 5-4: Continued.

ID	Cluster	LSR	Relative offset				Proper motion						Peak intensity		
		velocity	RA	σ_α	Dec	σ_δ	μ_α	$\sigma\mu_\alpha$	V_x	μ_δ	$\sigma\mu_\delta$	V_y	1st	2nd	3rd
		(km s^{-1})	(mas)				(mas yr^{-1})		(km s^{-1})	(mas yr^{-1})		(km s^{-1})	(Jy $beam^{-1}$)		
(1)	(2)	(3)	(4)	(5)	(6)	(7)	(8)	(9)	(10)	(11)	(12)	(13)	(14)	(15)	(16)
74	I, II	−1.41	34.95	0.12	−28.73	0.05	···	···	···	···	···	···	3.53	1.41	0.75
75	I, II	−1.94	39.13	0.63	39.68	0.50	···	···	···	···	···	···	···	5.15	···
76	I, II	−1.76	40.76	0.43	39.13	0.41	···	···	···	···	···	···	···	3.38	···
77	I, II	−1.59	41.41	0.41	38.33	0.41	···	···	···	···	···	···	···	1.64	···
78	I, II	−2.11	41.60	0.32	−25.99	0.19	···	···	···	···	···	···	5.88	···	···
79	I, II	−1.94	41.71	0.21	−26.99	0.13	···	···	···	···	···	···	8.44	···	···
80	I, II	−1.41	42.39	0.55	37.45	0.45	···	···	···	···	···	···	···	0.63	···
81	I, II	−2.64	43.88	0.41	−27.14	0.31	···	···	···	···	···	···	···	7.10	···
82	I, II	−2.46	44.57	0.58	−27.80	0.43	···	···	···	···	···	···	···	5.81	···
83	I, II	−2.64	48.84	0.29	−28.98	0.16	0.59	0.16	1.97	0.16	0.09	0.55	3.94	···	5.38
84	I, II	−2.64	60.28	0.28	−35.42	0.16	···	···	···	···	···	···	4.18	···	···
85	I, II	−2.99	70.86	0.28	−24.90	0.21	···	···	···	···	···	···	3.33	3.28	···
86	I, II	−3.34	71.10	0.28	−24.70	0.18	···	···	···	···	···	···	1.26	2.74	1.33
87	I, II	−3.17	71.25	0.15	−24.85	0.10	0.30	0.11	1.01	0.50	0.07	1.68	3.13	5.32	2.38
88	V	−4.92	115.92	0.48	538.56	0.41	···	···	···	···	···	···	···	···	1.09
89	I, II	−1.94	119.95	0.30	3.88	0.17	···	···	···	···	···	···	6.48	···	···
90	V	−5.10	120.52	0.67	534.02	0.71	···	···	···	···	···	···	···	0.59	···
91	V	−4.92	121.12	0.26	533.02	0.27	0.36	0.24	1.20	0.43	0.24	1.42	···	1.68	2.93
92	V	−4.75	122.16	0.34	532.20	0.35	···	···	···	···	···	···	···	1.75	3.29
93	V	−4.92	124.18	0.21	530.14	0.22	···	···	···	···	···	···	···	···	2.38
94	V	−4.92	128.07	0.33	525.42	0.34	···	···	···	···	···	···	···	1.41	2.15
95	V	−4.75	129.54	0.31	523.64	0.33	···	···	···	···	···	···	···	1.91	2.85
96	I, II	−1.94	131.74	0.45	0.10	0.23	···	···	···	···	···	···	4.79	···	···
97	V	−4.92	133.56	0.40	520.15	0.31	···	···	···	···	···	···	···	···	1.32
98	V	−4.92	138.41	0.63	511.83	0.59	···	···	···	···	···	···	···	0.69	···

Table 5-4: Continued.

ID	Cluster	LSR	Relative offset				Proper motion						Peak intensity		
		velocity	RA	σ_α	Dec	σ_δ	μ_α	$\sigma\mu_\alpha$	V_x	μ_δ	$\sigma\mu_\delta$	V_y	1st	2nd	3rd
		(km s^{-1})	(mas)				(mas yr^{-1})		(km s^{-1})	(mas yr^{-1})		(km s^{-1})	(Jy beam^{-1})		
(1)	(2)	(3)	(4)	(5)	(6)	(7)	(8)	(9)	(10)	(11)	(12)	(13)	(14)	(15)	(16)
99	V	−4.75	140.27	0.52	511.04	0.53	...	...	...	...	...	...	...	1.00	...
100	V	−4.75	151.31	0.25	504.58	0.18	...	...	...	...	...	...	1.43	3.57	...
101	V	−4.92	151.40	0.92	504.26	0.68	...	...	...	...	...	...	0.45	1.56	...
102	V	−4.57	151.96	0.23	504.27	0.18	0.59	0.45	1.97	−1.33	0.47	−4.42	1.55	2.75	...
103	V	−4.57	157.68	0.23	496.85	0.19	1.72	0.46	5.72	−1.87	0.49	−6.24	1.51	2.81	...
104	V	−4.92	157.90	0.72	495.60	0.53	...	...	...	...	...	...	0.46	1.59	...
105	V	−4.75	158.16	0.26	496.37	0.19	1.14	0.37	3.79	−1.23	0.32	−4.09	1.33	3.10	...
106	V	−4.75	165.18	0.55	488.11	0.41	...	...	...	...	...	...	0.65	1.15	...
107	V	−4.92	167.38	0.69	483.48	0.81	...	...	...	...	...	...	...	0.58	...
108	II	−2.64	402.69	0.60	−149.27	0.34	...	...	...	...	...	...	1.87	...	...
109	II	−2.46	405.57	0.82	−148.12	0.36	...	...	...	...	...	...	2.81	...	...
110	II	−2.82	406.40	0.64	−155.93	0.37	...	...	...	...	...	...	3.25	...	...
111	II	−2.99	407.92	0.30	−156.50	0.18	1.92	0.89	6.40	−1.19	0.83	−3.97	3.44	1.92	...
112	II	−3.17	408.88	0.37	−156.78	0.25	...	...	...	...	...	...	1.36	...	...
113	II	−3.17	411.60	0.51	−160.53	0.58	...	...	...	...	...	...	...	1.11	...
114	II	−2.82	413.36	1.04	−161.94	0.71	...	...	...	...	...	...	2.08	...	...
115	II	−2.99	413.61	0.39	−162.63	0.27	...	...	...	...	...	...	2.53	...	...
116	II	−3.17	413.71	0.45	−163.00	0.29	...	...	...	...	...	...	1.15	...	...
117	II	−0.53	417.61	0.76	−167.09	0.35	...	...	...	...	...	...	0.39	...	...
118	II	−0.36	418.01	0.50	−166.97	0.27	...	...	...	...	...	...	0.43	...	...
119	II	−3.34	437.00	0.91	−163.80	0.28	...	...	...	...	...	...	0.60	...	...
120	II	−3.52	451.96	0.48	−142.77	0.54	...	...	...	...	...	...	...	1.06	...
121	II	−3.34	452.28	0.49	−143.34	0.60	...	...	...	...	...	...	...	0.73	...
122	IV	−4.05	1299.50	0.30	−188.51	0.32	...	...	...	...	...	...	...	3.52	...
123	IV	−4.57	1324.54	0.35	−185.54	0.14	...	...	...	...	...	...	...	...	2.59

Table 5-4: Continued.

ID	Cluster	LSR	Relative offset				Proper motion						Peak intensity		
		velocity	RA	σ_α	Dec	σ_δ	μ_α	$\sigma\mu_\alpha$	V_x	μ_δ	$\sigma\mu_\delta$	V_y	1st	2nd	3rd
		(km s^{-1})	(mas)				(mas yr^{-1})		(km s^{-1})	(mas yr^{-1})		(km s^{-1})	(Jy beam^{-1})		
(1)	(2)	(3)	(4)	(5)	(6)	(7)	(8)	(9)	(10)	(11)	(12)	(13)	(14)	(15)	(16)
124	IV	−4.05	1327.92	0.49	−193.17	0.47	···	···	···	···	···	···	···	···	6.27
125	IV	−4.57	1329.57	0.34	−183.19	0.17	···	···	···	···	···	···	···	···	2.35
126	IV	−3.87	1329.78	0.32	−193.76	0.42	···	···	···	···	···	···	···	2.99	···
127	IV	−4.22	1331.99	0.23	−193.64	0.15	···	···	···	···	···	···	···	···	9.09
128	IV	−3.87	1338.30	0.11	−183.16	0.06	−1.77	0.61	−5.89	−0.51	0.11	−1.71	8.25	···	3.47
129	IV	−4.05	1339.17	0.11	−183.07	0.06	···	···	···	···	···	···	17.80	5.81	13.41
130	IV	−4.40	1339.22	0.24	−182.58	0.14	1.44	0.31	4.81	−0.45	0.21	−1.49	7.09	8.61	···
131	IV	−4.57	1339.60	0.35	−182.07	0.20	···	···	···	···	···	···	1.28	···	···
132	IV	−4.22	1340.21	0.12	−182.46	0.07	−1.63	0.09	−5.43	−0.42	0.04	−1.39	18.66	13.59	17.48
133	IV	−4.22	1343.25	0.20	−159.69	0.09	···	···	···	···	···	···	···	···	11.24
134	IV	−4.22	1343.92	0.12	−167.71	0.12	···	···	···	···	···	···	···	11.82	···
135	IV	−4.40	1344.40	0.11	−168.19	0.13	1.09	0.30	3.64	0.42	0.18	1.39	···	8.10	9.14
136	IV	−4.57	1344.84	0.18	−168.65	0.22	0.37	0.22	1.23	0.99	0.20	3.30	···	2.76	2.61
137	IV	−4.40	1344.95	0.11	−179.55	0.06	−0.47	0.12	−1.57	−0.78	0.07	−2.60	15.19	23.24	15.42
138	IV	−4.57	1345.05	0.19	−179.65	0.10	−0.14	0.11	−0.46	−0.32	0.06	−1.05	2.41	6.73	4.53
139	IV	−4.22	1345.68	0.07	−180.35	0.05	···	···	···	···	···	···	30.94	29.77	19.45
140	IV	−4.22	1345.75	0.13	−175.55	0.07	···	···	···	···	···	···	···	···	17.06
141	IV	−4.05	1345.87	0.26	−166.70	0.13	0.71	0.17	2.37	−0.46	0.09	−1.54	6.72	6.80	11.68
142	IV	−4.22	1346.01	0.29	−195.36	0.16	···	···	···	···	···	···	6.55	···	···
143	IV	−3.69	1346.17	0.18	−181.41	0.10	···	···	···	···	···	···	2.13	···	···
144	IV	−4.05	1346.58	0.06	−180.29	0.04	−1.04	0.09	−3.48	−0.75	0.06	−2.51	28.78	13.40	13.95
145	IV	−3.87	1347.60	1.50	−136.95	0.25	···	···	···	···	···	···	···	···	3.00
146	IV	−3.87	1347.64	0.09	−180.68	0.05	···	···	···	···	···	···	11.53	···	···
147	IV	−4.05	1352.70	0.12	−178.68	0.07	···	···	···	···	···	···	16.28	6.18	···
148	IV	−4.22	1352.85	0.20	−178.36	0.10	−0.89	0.16	−2.97	−1.10	0.08	−3.68	12.43	10.02	9.21

Table 5-4: Continued.

ID	Cluster	LSR	Relative offset				Proper motion						Peak intensity		
		velocity	RA	σ_α	Dec	σ_δ	μ_α	$\sigma\mu_\alpha$	V_x	μ_δ	$\sigma\mu_\delta$	V_y	1st	2nd	3rd
		(km s^{-1})	(mas)				(mas yr^{-1})		(km s^{-1})	(mas yr^{-1})		(km s^{-1})	(Jy beam^{-1})		
(1)	(2)	(3)	(4)	(5)	(6)	(7)	(8)	(9)	(10)	(11)	(12)	(13)	(14)	(15)	(16)
149	IV	−4.40	1353.61	0.20	−182.49	0.19	⋯	⋯	⋯	⋯	⋯	⋯	⋯	5.46	⋯
150	IV	−3.87	1353.82	0.15	−179.17	0.09	⋯	⋯	⋯	⋯	⋯	⋯	6.22	⋯	⋯
151	IV	−4.57	1354.54	0.48	−184.84	0.43	⋯	⋯	⋯	⋯	⋯	⋯	⋯	1.43	⋯
152	IV	−4.40	1354.72	0.49	−178.35	0.26	⋯	⋯	⋯	⋯	⋯	⋯	3.52	⋯	⋯
153	IV	−3.69	1361.74	0.15	−164.10	0.09	⋯	⋯	⋯	⋯	⋯	⋯	2.52	⋯	⋯
154	IV	−4.05	1362.43	0.19	−163.66	0.19	⋯	⋯	⋯	⋯	⋯	⋯	⋯	5.82	⋯
155	IV	−3.87	1362.97	0.18	−163.11	0.10	−0.82	0.36	−2.72	−0.49	0.11	−1.64	4.36	⋯	4.21
156	IV	−4.40	1372.61	0.48	−294.80	0.28	⋯	⋯	⋯	⋯	⋯	⋯	3.18	⋯	⋯
157	IV	−3.69	1372.90	0.28	−160.63	0.18	⋯	⋯	⋯	⋯	⋯	⋯	1.32	⋯	⋯
158	IV	−4.40	1411.25	0.49	−263.13	0.31	⋯	⋯	⋯	⋯	⋯	⋯	3.26	⋯	⋯

Column 1: spot identification number (in RA order); Column 2: cluster number associated with each maser spot; Column 3: LSR velocity; Columns 4–7: relative positional offsets with respect to the reference maser spot and uncertainties in the first epoch; Columns 8–13: internal proper motions, fitting errors, and tangential velocities for the right ascension and declination directions, respectively; Columns 14–16: peak intensities at each epoch.

* Reference spot for relative position and velocity. The absolute coordinates of the spot are given in the text.

Chapter 6

Discussions

6.1 Spatial Morphology

We presented the results of the spatial distributions for each epoch and the detected internal proper motions of the 6.7 GHz methanol maser spots in ON 1, W75 N, Cep A in chapter 5. The distributions are classified into two types: an separated structure in ON 1, and an arched structure in W75 N and Cep A. The arched structures are also classified into the elliptical morphology defined by [7]Bartkiewicz et al. (2009) in ~30% of their sources. We present relation between the spatial morphology and their radial velocities in this section.

The linear velocity gradients along the elongated structures of the maser spots are well known to be observed in ~40% of the 6.7 GHz methanol maser sources (e.g., [135]Phillips et al. 1998; [184]Walsh et al. 1998). The elongated structure and linear velocity gradient can be simply interpreted as a rotating disk seen from edge-on (hereafter we call it "edge-on disk", e.g., [115]Minier et al. 2000). This edge-on disk model assumes that the maser spots locate on a concentric radius around a central star, and a rotating speed is constant. We show relations between the position of the maser spots along the elongated structure and radial velocities for each first-epoch data in figure 6-1 (the figures are called as "p-v diagram"). The directions of the elongation are assumed to the declination for ON 1 and W75 N, and the right ascension for Cep A. The clear linear velocity gradient was seen only in the p-v diagram of the methanol masers in W75 N. The p-v diagram provided the velocity gradient dv/dx by applying a linear least-square fit: $-5.7 \pm 0.1 \times 10^{-3}$, $-2.7 \pm 0.1 \times 10^{-3}$, and $-1.1 \pm 0.2 \times 10^{-3}$ km s^{-1} AU^{-1} for ON 1, W75 N, and Cep A. An enclosed mass M in the edge-on rotating disk, whose radius r is assumed as the size of the elongation of the methanol maser distribution, are estimated from this equation $M = (r^3/G) \cdot (dv/dx)^2$, where G is the gravitational constant ($= 6.6743 \times 10^{-11}$ m^3 s^{-2} kg^{-1}). The masses were estimated to $92.9^{+4.5}_{-4.3}$, $7.4^{+0.8}_{-0.7}$, and $0.3^{+0.2}_{-0.1}$ $M_\odot$ for ON 1, W75 N, and Cep A. Firstly, the 6.7 GHz methanol masers in W75 N are well known to be associated with the VLA 1. The central star in the VLA 1 is believed to be in B1 spectral type ([148]Shepherd et al. 2004), whose mass is known to be 8-16 $M_\odot$. Our estimated enclosed mass for W75 N is consistent with the central mass in the VLA 1. For ON 1, there are four YSOs within an area of the methanol maser distribution, that is the SMA2, 4, 5, and the UC Hɪɪ region. Even if all of their masses are summed of 19-27 $M_\odot$, however, the mass is not enought to be our estimated enclosed mass for ON 1. Given the outward motions in the north-south direction detected in the internal proper motions of the methanol masers as mentioned in section 5.1.2, a rotating disk model can be unlikely. For Cep A, our estimated enclosed mass is much low as the central mass of a high-mass star (> 8 $M_\odot$), and as the enclosed mass ~ 20 $M_\odot$ estimated from the distribution size and the radial velocity gradient of the CH_3CN line emission ([129]Patel et al. 2005). This result was already indicated by [172]Torstensson et al.

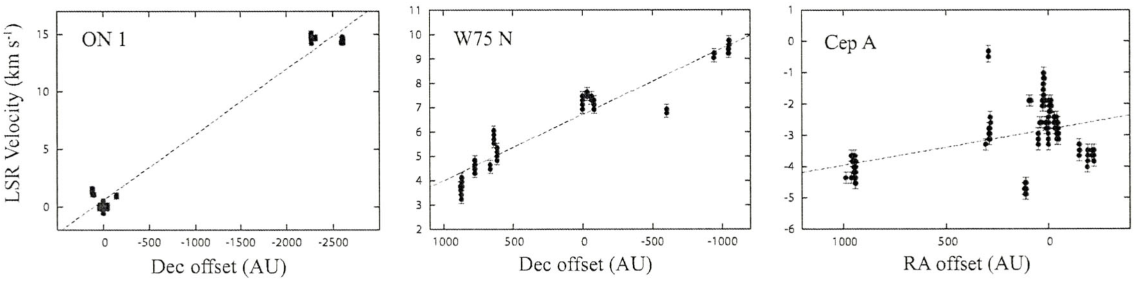

Figure 6-1: P-v diagrams of the 6.7 GHz methanol masers for each source. The horizontal axis shows relative positional offsets along the elongated structure: declination for ON 1 and W75 N, and right ascension for Cep A. The vertical axiz shows the radial velocity. The dash lines indicate a linear fit.

Table 6-1: Parameters estimated by fitting ellipse structure.

Source	Epoch	Coordinates		a	$\mathrm{PA_{mj}}$	i
		$\Delta\alpha$ (mas)	$\Delta\delta$ (mas)	(AU)	(°)	(°)
W75 N	1st	−83	−115	1192	−3	80
	2nd	−96	−89	1065	−2	78
Cep A	1st	+436	+118	680	110	73
	2nd	+385	+125	756	114	75
	3rd	+378	+141	720	112	74

Column 1: source name; Column 2: number of observational epoch; Column 3-4: relative center coordinates of the ellipse to the reference spot; Column 5-7: radius of semi-major axis, position angle (north is 0°, and counterclockwise is positive), and inclination of the ellipse (a direction from the face-on is 0°).

(2010), and the authors presented that the Cep A methanol masers were associated with not a simply rotating disk but rather a rotating with infall disk. The infall velocity was estimated to 1.3 km s^{-1} by using the ring model defined by [175]Uscanga et al. (2008) and [7]Bartkiewicz et al. (2009). We therefore conclude that the methanol maser in W75 N and Cep A could be associated with the rotating disk and/or with expansion/infall, while the maser in ON 1 is associated with other morphology.

The arched structures of the 6.7 GHz methanol masers in W75 N and Cep A are least-square fitted by using an elliptical structure, and estimated parameters for each epoch are summarized in table 6-1: the parameters are the relative center coordinates of the ellipse to the reference spot ($\Delta\alpha, \Delta\delta$), the radius of semi-major axis of the ellipse a, the position angle of the major axis $\mathrm{PA_{mj}}$ (north is 0°, and counterclockwise is positive), and the inclination angle i (a direction from the face-on is 0°) of the disk assumed that the disk has basically ring structure. The inclination angle is the angle between the radial direction and the normal to the ring plane, which is defined to be $i = \arccos(b/a)$, where b the radius of semi-minor axis of the ellipse. We use hereafter averaged parameters for deriving various parameters in following sections: for W75 N $(\Delta\alpha, \Delta\delta) = (-90 \pm 7, -102 \pm 13)$ mas, $a = 1129 \pm 64$ AU, $\mathrm{PA_{mj}} = -3 \pm 1°$, $i = 79 \pm 1°$, and for Cep A $(\Delta\alpha, \Delta\delta) = (+400 \pm 18, +128 \pm 7)$ mas, $a = 719 \pm 22$ AU, $\mathrm{PA_{mj}} = 112 \pm 1°$, $i = 74 \pm 1°$.

6.2 Spatial Relationship

6.2.1 ON 1

(The following description for ON 1 is extracted from the published paper in 2011 [162].)

In figure 6-2 left-panel, we superposed the 6.7 GHz methanol masers in ON 1 (open squares) on the 22.2 GHz water masers (open circles, [125]Nagayama et al. 2008), hydroxyl masers at 1.665 and 1.667 GHz (crosses, [59]Fish & Reid 2007), and continuum emission at 8.4 GHz (white contours, [3]Argon et al. 2000) and at 345 GHz (stars, [157]Su et al. 2009). The arrows indicate the directions of the northeast-southwest bipolar outflow traced by $H^{13}CO^+$ and SiO lines ([95]Kumar et al. 2004), and the dashed line represents the axis of the east-west bipolar outflow observed in the CO $J = 2-1$ line and discussed by [125]Nagayama et al. (2008). The absolute positional accuracy of the methanol masers was 1 mas, and those of the water and hydroxyl masers were ~80 mas and 200 mas, respectively. Those of the 8.4 GHz and 345 GHz continuum emissions were $\sim 0''.3$ and $\sim 0''.1$, respectively.

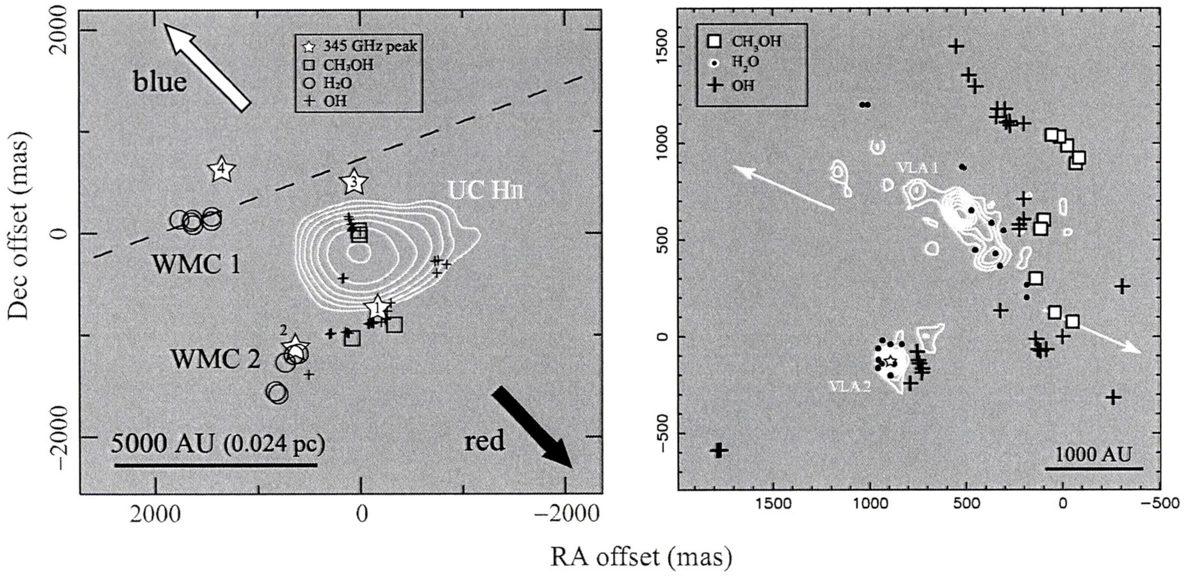

Figure 6-2: Left-panel:the observed methanol maser distribution (open squares) in ON 1 superposed on the 8.4 GHz radio continuum map (white contours) of UC HII region ([3]Argon et al. 2000). The origin corresponds to the absolute coordinates of the 6.7 GHz methanol maser. The star symbols correspond to the positions of the brightness peak of the dust emissions at 345 GHz and their number denote the SMA1–4 ([157]Su et al. 2009), while the SMA5 locates out of this figure. Average sizes of the dust emissions are ~ 1 arcsec^2. The water maser ([125]Nagayama et al. 2008) and the hydroxyl maser distributions ([59]Fish & Reid 2007) are shown by open circles and crosses, respectively. The WMC 1 and 2 were defined in [125]Nagayama et al. (2008). The arrows represent the directions of the NE-SW bipolar outflows traced by H^{13}CO$^+$ $J = 1{-}0$ and SiO $J = 2{-}1$ lines (Kumar et al. 2004). The colors of black and white correpond to the red- and blue-shifted sides with respect to the systemic velocity. The dashed line indicates the axis of the E-W bipolar outflow observed in the CO $J = 2{-}1$ line ([95]Kumar et al. 2004); Right-panel:the detected methanol maser distribution (white squares) in W75 N superposed on the 22 GHz radio continuum map (white contours: [168]Torrelles et al. 1997), whose negative emissions are subtracted. The VLA 3 locates out of this figure. The origin corresponds to the absolute coordinates of the hydroxyl maser measured by [152]Slysh et al. (2010): α(J2000.0) = $20^{\mathrm{h}}38^{\mathrm{m}}36^{\mathrm{s}}.4082$, δ(J2000.0) = $+42°37'34''.238$ with an accuracy of 2 mas. The star symbol shows the position of the radio continuum emission at 43 GHz ([148]Shepherd et al. 2004). The water maser ([168]Torrelles et al. 1997) and the hydroxyl maser distributions ([152]Slysh et al. 2010) are shown by filled circles and crosses, respectively. The two arrows indicate the direction of the bipolar outflow (PA= 66°: [84]Hunter et al. 1994).

Note that each cluster of the methanol maser spots coincided spatially with a cluster of hydroxyl masers (defined in figure 1 of [59]Fish & Reid 2007): cluster I to the N cluster, cluster II to the SW cluster, and cluster III to the SE cluster. These two types of masers also have similar LSR velocity ranges: -0.52 to 15.12 and 2.48 to 16.73 km s^{-1} for methanol and hydroxyl masers, respectively. The hydroxyl masers were thought to be associated with the expanding UC HII region because their internal proper motions showed an expansion with respect to the center of the peak of the 8.4 GHz continuum emission. A coincidence between the methanol and hydroxyl masers was suggested by a maser-excitation model ([33]Cragg et al. 2002). According to the model, a physical condition that produces simultaneous population inversions in both the 6.7 GHz methanol and 1.6 GHz hydroxyl transitions by infrared radiation is achieved.

On the other hand, the water masers of WMC 1 were clearly separated from the methanol and hydroxyl masers, with a positional offset of $\sim 1''.5$, i.e., $\sim$4000 AU at 2.57 kpc. The LSR velocities of the water masers also differed from those of the methanol and hydroxyl masers, showing far higher velocities and a wider range of V_{lsr}(~ -60 to

60 km s^{-1}). [125]Nagayama et al. (2008) suggested that the two clusters of water masers (WMC 1 and 2) would be associated with YSOs at around the dust emission peaks at 345 GHz (SMA4 and 2). Theoretical models of water maser excitation ([49]Elitzur et al. 1992) predicted that water masers were produced by collisional pumping within shocked layers.

The distinctions between the methanol and hydroxyl masers and the water masers in ON 1 in terms of their spatial distributions and radial/tangential velocities can also be understood in terms of the types of associated sources. These results suggest that methanol and hydroxyl masers are excited by different sources at separate sites and by different pumping mechanisms from those of the water masers.

6.2.2 W75 N

In figure 6-2 right-panel, we superposed the 6.7 GHz methanol masers in W75 N (white squares) on the 22.2 GHz water masers (filled circles, [168]Torrelles et al. 1997), hydroxyl masers at 1.665 GHz (crosses, [152]Slysh et al. 2010), continuum emission at 22 GHz (VLA 1 and 2: white contours, [168]Torrelles et al. 1997), and the position of the continuum emission at 43 GHz (a star symbol, [148]Shepherd et al. 2004). We note that the hydroxyl maser data observed in June 2006 were used in figure 6-2 right-panel. The arrows indicate the directions of the bipolar outflow with PA of 66° ([84]Hunter et al. 1994). The absolute positional accuracy of the methanol masers was $\sim$20 mas, and those of the water and hydroxyl masers were $\sim$50 mas and 2 mas, respectively. Those of the 22, 43 GHz continuum emissions were $\sim 0''.1$.

The methanol maser spots are associated with the VLA 1 defined by the 22 GHz continuum observation, while the radio continuum emission at 43 GHz was detected in only the VLA 2. Each cluster of the methanol maser spots locate near each the hydroxyl maser spots (defined in figure 5 of [154]Slysh et al. 2002): cluster I to the hydroxyl maser identified as D and F–I, cluster II to the hydroxyl maser identified as C and E, and cluster III to the hydroxyl maser identified as A and B. The hydroxyl masers associated with the VLA 1 in W75 N were thought to trace a simple rotating disk ([154]Slysh et al. 2002). There are not precisely coincidence but the methanol maser distribution in $\sim$200 AU west from the hydroxyl maser distribution. As mentioned in section 5.2.1, the radial velocity range of the methanol maser ($3.25 \leq V_{\rm lsr} \leq 9.76$ km s^{-1}) is covered from that of the hydroxyl maser ($3.70 \leq V_{\rm lsr} \leq 12.45$ km s^{-1}). But the radial velocity of the hydroxyl masers are $\sim$2 km s^{-1} higher than that of the methanol maser in each cluster: in cluster I $V_{\rm lsr}$ = 3.25 to 6.24 km s^{-1} while the hydroxyl ones $V_{\rm lsr}$ = 3.70 to 7.35 km s^{-1}, in cluster II $V_{\rm lsr}$ = 6.77 to 7.65 km s^{-1} while the hydroxyl ones $V_{\rm lsr}$ = 6.00 to 9.35 km s^{-1}, and in cluster III $V_{\rm lsr}$ = 9.05 to 9.76 km s^{-1}, while the hydroxyl ones $V_{\rm lsr}$ = 9.38 to 12.45 km s^{-1}. These slightly offsets of the spatial position and the radial velocity could be a difference of a distance from an exciting source, which is probably the B1 type star forming the VLA 1 jet. The hydroxyl maser spots are distributed $\sim$600 AU west from the peak of the 22 GHz continuum emission, while the methanol maser spots are distributed $\sim$800 AU west. Assumed that the simple Keplerian rotation, the rotation velocity is in proportion to $r^{-1/2}$, where r is a distance from the exciting source. The 1.3 times difference of the distance from the VLA 1 star provides 0.87 times difference of the radial velocity. These can affect the slightly offset between the hydroxyl and the methanol masers.

We estimated each velocity of the disk by fitting radial velocities of the methanol maser using the ring model, which was suggested by [175]Uscanga et al. (2008) and [7]Bartkiewicz et al. (2009). As introduced in section 1.2.4, the ring model is expressed to be $V_{\rm lsr} = (x'/a)\sin i \cdot V_{\rm rot} + (y'/a)\tan i \cdot V_{\rm exp} + V_{\rm sys}$, where $V_{\rm lsr}$ is the radial velocity of the maser spot, $V_{\rm rot}$, $V_{\rm exp}$, $V_{\rm sys}$ is the rotation, expansion, and systemic velocity of each source, respectively. And x', y' are the central position, a the radius of the major axis, and i the inclination angle of the ellipse structure. The parameters of the elliptical structure at the first epoch were used as the ring parameter in this estimation. Each velocity was estimated to be $V_{\rm rot} = 3.13$, $V_{\rm exp} = -0.16$, $V_{\rm sys} = 7.36$ km s^{-1}, and the model results are presented in figure 6-4 lower-panel. We note that the expansion velocity is negative leading to the infall velocity. The rotation velocity is dominant compared to the infall velocity, and this fitted result is consistent with the simple rotation as described in section 6.1.

On the other hand, the water masers in W75 N are associated with mainly the VLA 1 and 2 ([168]Torrelles et al. 1997). The water maser spots associated with the VLA 1 were distributed along the elongation (PA= 43°) of the 22 GHz continuum emission, and the internal proper motions showed a bipolar outward motion parallel to the elongated structure and the motions were well-collimated with OP< 10° ([171]Torrelles et al. 2003). The motions were nearly parallel to the direction of the bipolar molecular outflow (PA= 66°: [84]Hunter et al. 1994). The water masers in the VLA 1 clearly trace a well-collimated outflow driven by the associated YSO.

The differences of emitted regions and the exciting mechanism have been also predicted: the methanol and the hydroxyl masers are excited by infrared radiation from nearby warm dust ([33]Cragg et al. 2002), while the water masers are produced by collisional pumping within shocked layers ([49]Elitzur et al. 1992).

6.2.3 Cep A

In figure 6-3, we superposed the 6.7 GHz methanol masers in Cep A (white squares) on the 22.2 GHz water masers (filled circles, [167]Torrelles et al. 1996), dust continuum emissions at 335 GHz (dashed contours, [169]Torrelles et al. 2007), NH_3 (4, 4) line emissions (thin contours: [169]Torrelles et al. 2007), SO_2 line emissions (thick contours: [86]Jiménez-Serra et al. 2007), and the position of the peak at 43 GHz continuum emission (a star symbol, [37]Curiel et al. 2006). The position of the 43 GHz peak is thought to be the location of an exciting source for Cep A-HW2. The absolute positional accuracy of both the methanol masers and the water masers was ~1 mas. Those of the 335 GHz continuum and the molecular line emissions were $\sim 0''.1$. That of the 43 GHz peak was estimated as ~10 mas.

As mentioned in section 5.3.1, the arched structure of the methanol maser spots in Cep A coincided with the CH_3CN and NH_3 rotating disks surrounding the dust emission at 335 GHz and the velocity range of the spots is similar to that of these disks. The overall size of the arched structure estimated by elliptical fitting 1438 AU was approximately equal to the size of the NH_3 disk of ~1400 AU. The size of the CH_3CN disk of ~1200 AU was roughly equal to ones in both the maser and NH_3 emissions. The position angle of the ellipse structure ~ 112° was also roughly equal to the angle of the CH_3CN disk ~ 124°. The peak of the 43 GHz continuum emission located close to the center of the elliptical structure formed with the methanol maser spots: for relative positions with respect to the reference spot of the methanol maser, the peak of the 43 GHz emission locates $(\Delta\alpha, \Delta\delta) = (+550, -7)$ mas, while the center of the ellipse is $(\Delta\alpha, \Delta\delta) = (+400 \pm 18, +128 \pm 7)$ mas. The radio continuum jet at 22 GHz along a PA of 45° (e.g., [167]Torrelles et al. 1996) was nearly perpendicular to the ellipse structure fitted from the methanol maser spots distribution as well as the molecular disks (as shown in figure 6-3 right-panel): a difference between position angles is 67-79°. These characteristics suggest that the 6.7 GHz methanol masers in Cep A-HW2 could be associated with a rotating disk as well as the CH_3CN and the NH_3 line emissions.

We estimated each velocity of the disk using the ring model in the same way of the case for the W75 N methanol maser. The parameters of the elliptical structure at the first

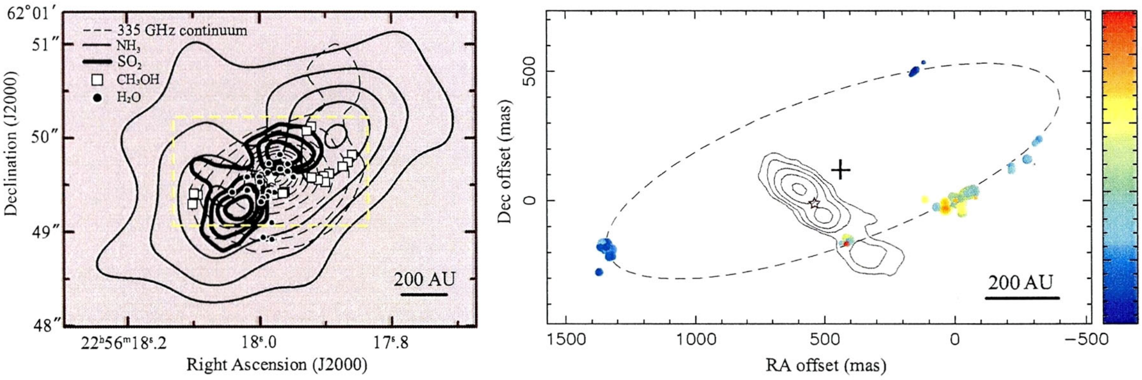

Figure 6-3: Left-panel:the methanol maser spots in Cep A (white squares) superposed on the water maser spots (filled circles: [167]Torrelles et al. 1996), dust continuum emissions at 335 GHz (dashed contours: [169]Torrelles et al. 2007), NH_3 (4, 4) line emissions (thin contours: [169]Torrelles et al. 2007), and SO_2 emissions (thick contours: [86]Jiménez-Serra et al. 2007). A star symbol indicates the peak of 43 GHz continuum emission, which is thought to be the location of an exciting source ([37]Curiel et al. 2006); Right-panel:blow-up figure of a yellow rectangular part in the left-panel. The 6.7 GHz methanol maser spots are represented by colored circles, and an ellipse shows a best fit toward the maser overall distribution. The plus sign indicates the center of the ellipse. The contours indicate the radio continuum jet observed at 22 GHz by [170]Torrelles et al. (1998) and re-reduced by [65]Gallimore et al. (2003).

epoch were used as the ring parameter in this estimation. Each velocity was estimated to be $V_{\rm rot} = -0.02$, $V_{\rm exp} = -1.44$, $V_{\rm sys} = -3.82$ km s^{-1}, and the model results are presented in figure 6-4 upper-panel. The expansion velocity is negative leading to the infall velocity. The infall velocity is dominant compared to the rotation velocity, and this fitted result is consistent with the result obtained by [172]Torstensson et al. (2010).

Cep A-HW2 is one of very rare sources that both the methanol and the water masers are associated with a same YSO and trace same kinematics. The water maser spots in Cep A-HW2 were observed as tracing a rotating disk from characteristics of spatial elongation perpendicular to the radio jet and a linear velocity gradient along the elongation ([167]Torrelles et al. 1996). The size of the water maser disk is ∼600 AU, which is more 2 times smaller than the size of the methanol maser disk. This difference in terms of size could be explained as a difference of excitation temperatures. Assumed that a central star isotropically radiates, dust tempratures around the star is in propotion to $r^{-1/2}$, where r is a distance from the central star. The theoretical model predicted the excitation temperature $\geq$ 400 K for the water masers ([49]Elitzur et al. 1992), while the temperature ∼100-200 K for the methanol masers ([34]Cragg et al. 2005). They indicate the water masers need hotter regions for those excitation rather than the methanol masers. Our estimation is consistent with the prediction from the theoretical model.

6.3 Exciting Sources

The 6.7 GHz methanol maser spots detected with the JVN were distributed in wide spatial area more than 1000 AU. Especially, the three clusters of the 6.7 GHz methanol maser in ON 1 are spatially separated with a scale of ∼2800 AU at maximum. We discuss exciting sources which produce each maser spot in each source, and whether each cluster is physically associated with each other and can be excited by a common source.

For the 6.7 GHz methanol masers in W75 N and Cep A, exciting sources are clear to determine. The methanol maser spots in W75 N are associated with the VLA 1, and are excited by a high-mass YSO forming the radio jet of VLA 1. The 22 GHz radio continuum

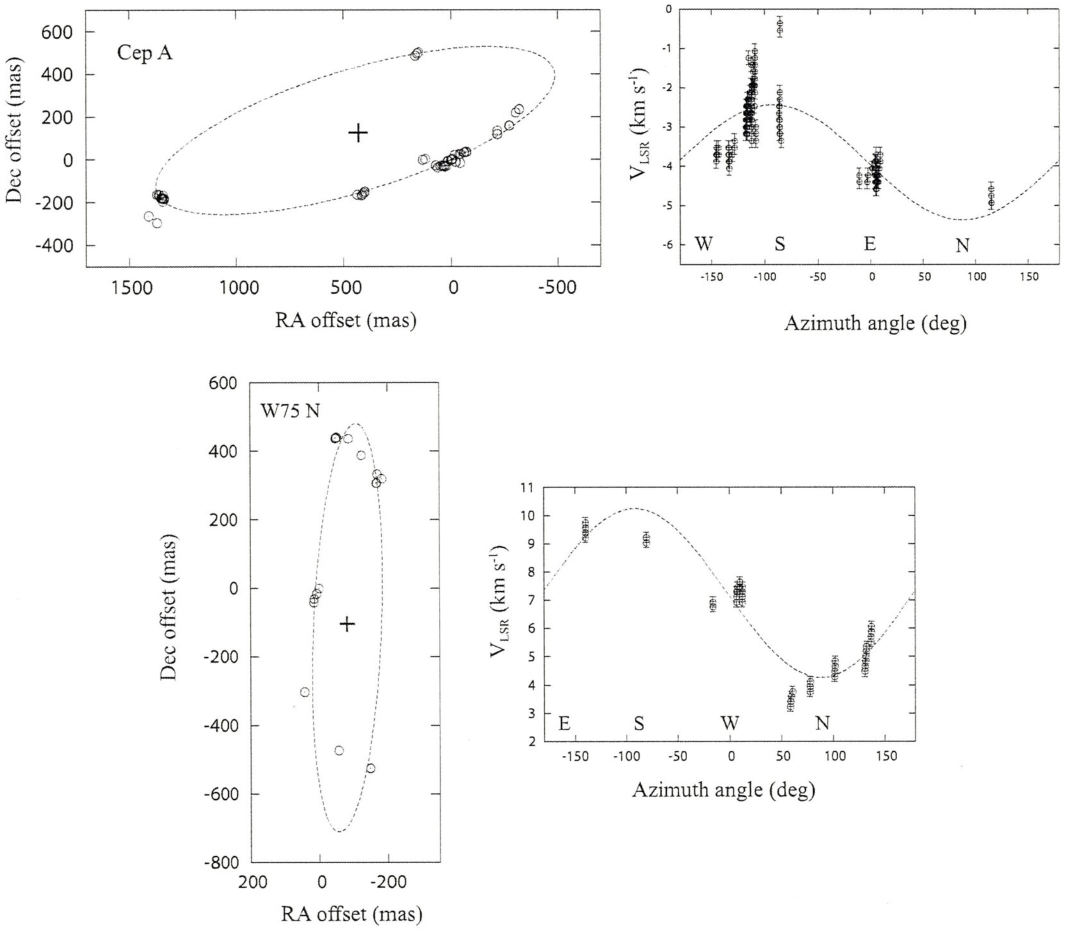

Figure 6-4: Fit of the ring model. Upper-panel:for the methanol maser in Cep A, the maser spot positions observed at the first epoch (open circles) with the fitted ellipse in left-panel. The plus sign indicates the center of the ellipse. In right-panel, the measured radial velocities (open circles) with errors are shown as a function of the azimuth angle on the ellipse. The dashed line shows the best fit using the ring model. Lower-panel:for the methanol maser in W75 N (each expression is same to the upper-panel).

emission, which corresponds to the VLA 1 radio jet, is the closest to the methanol maser spots. It is clear that the methanol maser spots in Cep A are excited by a high-mass YSO, which warms amibient dust detected at 335 GHz frequency and forms the radio jet along a PA of 45°. The location of the high-mass YSO was represented in the peak of the 43 GHz radio continuum emission. For the methanol masers in ON 1, three radio continuum sources, which consists of centimeter (UC HII region) and two submillimeter (dust: SMA1 and 3) emissions, are detected around the location of the methanol maser clusters. As mentioned in section 3.1, [157]Su et al. (2009) eventually concluded that the SMA1 and 3 were just dust emissions associated with the UC HII region, that is that the SMA1 and 3 do not include YSOs. Thus, there is only one high-mass star around the location of the clusters.

Some methanol maser emissions have shown periodic variation of flux density with synchronization above all spectral features (e.g., [71][74]Goedhart et al. 2003, 2009). Those maser spots were distributed in a scale of ~6000 AU at maximum, which corresponds to a size 2-4 times larger than that in the case of our observed sources. The 6.7 GHz methanol masers in Cep A-HW2 also showed the synchronized flux variation above all spectral features within 30 days ([161]Sugiyama et al. 2008b). The synchronized time variation of the masers are explained as all of the maser spots are pumped by infrared radiation from the dust that is heated by a common exciting source with a rapid variability ([161]Sugiyama et al. 2008b). Thus, the methanol maser clusters distributed in with the area of 2800, 2000, and 1400 AU in ON 1, W75 N, and Cep A can be produced with one exciting source.

We verify whether the methanol masers in W75 N and Cep A, which could be associated with the rotating disk, can be produced with the exciting star by estimating dust temperatures. Assumed that the exciting star isotropically radiates, a dust temprature T_d around the star can be derived by using the following equation: $T_\mathrm{d} = (16\pi\sigma)^{-1/4} \cdot r^{-1/2} \cdot L^{1/4}$, where r is the distance between each maser spot and the exciting star, L the luminosity of the star, and σ the stefan-boltzmann constant ($= 5.6705 \times 10^{-8}$ W m^{-2} K^{-4}). The luminosity of the star for each source was assumed as follows. The W75 N has the integrated FIR luminosity of 1.4×10^5 $L_\odot$ (e.g., [168]Torrelles et al. 1997), and there are three radio continuum sources named as VLA 1–3 ([168]Torrelles et al. 1997). Therefore, we used one-third value of the entire luminosity, that is 4.7×10^4 $L_\odot$. As mentioned in section 3.3, the Cep A-HW2 takes about half of the entire luminosity, that is 1.3×10^4 $L_\odot$. Assumed that r is the radius of the elliptical structure fitting the methanol maser distributions, the dust temperatures were derived to 122 ± 4 and 111 ± 2 K for W75 N and Cep A, respectively. These temperatures are consistent with the range of the dust temperature exciting the 6.7 GHz methanol masers ~100–200 K predicted by the theoretical model ([34]Cragg et al. 2005).

6.4 Sites Associated with the 6.7 GHz Methanol Masers

The spatial distributions of the 6.7 GHz methanol masers observed with the JVN were classified into two types as mentioned in section 6.1. The maser spots in W75 N and Cep A were distributed in the arched structures well fitted with the elliptical structure, while the spots in ON 1 were separated with each cluster more than 2000 AU. We discuss for sites associated with the 6.7 GHz methanol masers in ON 1, W75 N, and Cep A considered with the spatial distribution, spatial relation ship with other probes, and detected internal proper motions.

6.4.1 Rotating Disks with Infall/Expansion

It is thought to be possible that the elliptical structures of the 6.7 GHz methanol masers in W75 N and Cep A could be associated with the rotating disk and/or with expansion/infall because of their spatial structures, radial velocity gradient, and spatial relationship with other probes. The detected internal proper motions especially in Cep A supported the scenario of the disk. Those motions seen in most of the spots showed various vector in each maser cluster, especially random in cluster I and II, but orbited along the elliptical structure fitted by the methanol maser distribution, which was perpendicular to the radio continuum jet. The rotation velocity V_rot, the expansion velocity V_exp, and the systemic velocity V_sys were defined as follows:

$$\begin{aligned} V_x^\mathrm{calc} &= V_\mathrm{rot}\sin\theta + V_\mathrm{exp}\cos\theta & \text{(6-1)} \\ V_y^\mathrm{calc} &= -(V_\mathrm{rot}\cos\theta - V_\mathrm{exp}\sin\theta)\cos i & \text{(6-2)} \\ V_z^\mathrm{calc} &= -(V_\mathrm{rot}\cos\theta - V_\mathrm{exp}\sin\theta)\sin i + V_\mathrm{sys} & \text{(6-3)} \end{aligned}$$

where V_x^calc, V_y^calc are the tangential velocities in right ascension and declination directions, V_z^calc the radial velocity, θ the azimuth angle on the concentric radius of the disk, and i the inclination angle of the disk (a direction from the face-on is 0°). The disk model expressed in equation (6-1 – 6-3) is sketched in figure 6-5. The factors $\cos\theta$ and $\sin\theta$ related to the azimuth angle θ are defined to be x'/a and $y'/(a \cdot \cos i)$, where a is the radius of the disk corresponding to the major axis of the elliptical structure. About x'

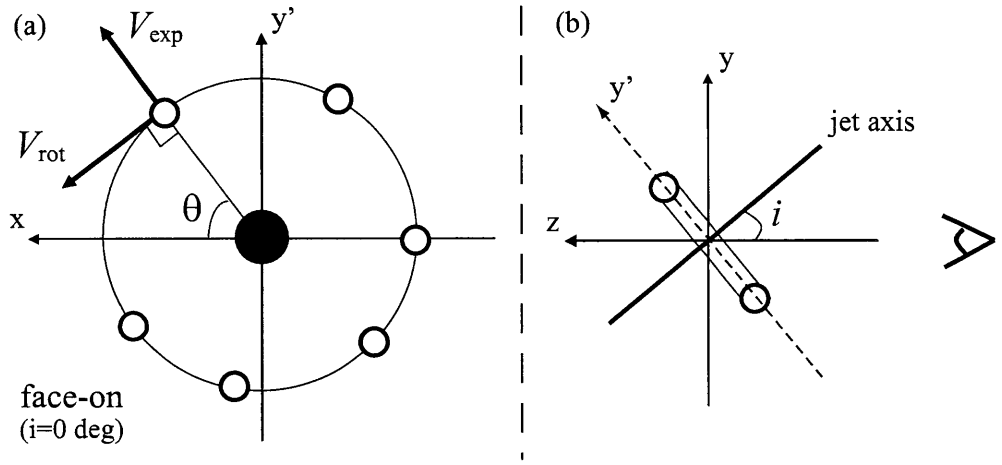

Figure 6-5: The disk model expressed in equation (6-1 – 6-3). (a) the model seen from the face-on direction ($i = 0°$). The filled and white circles correspond to an exciting star and methanol maser spots, respectively. (b) definition of the inclination angle. The horizontal axiz indicates the line-of-sight direction, and right side corresponds to an observer.

and y', these factors are converted as follows:

$$\begin{aligned} x' &= (x - x_0)\cos \mathrm{PA_{mj}} + (y - y_0)\sin \mathrm{PA_{mj}} \\ y' &= -(x - x_0)\sin \mathrm{PA_{mj}} + (y - y_0)\cos \mathrm{PA_{mj}} \end{aligned}$$

where x, y are the relative position to the reference spot, x_0, y_0 the center position of the ellipse, and $\mathrm{PA_{mj}}$ the position angle of the major axis. The solutions for each velocity were based on the minimisation of the χ^2 function expressed as follows (in detail how to solve is shown in appendix D):

$$\chi^2 = \sum_{j=1}^{N} w_j \left((V_{xj} - V_{xj}^{\rm calc})^2 + (V_{yj} - V_{yj}^{\rm calc})^2 + (V_{zj} - V_{zj}^{\rm calc})^2 \right) \tag{6-4}$$

where N is the number of the maser spots that the internal proper motions were detected, V_{xj}, V_{yj} the tangential velocities measured as the internal proper motions for the maser spot identified as ID j, V_{zj} the radial velocity corresponding to $V_{\rm lsr}$, and w_j the weight function expressed as $1/(\sigma_{xj}^2 + \sigma_{yj}^2 + \sigma_{zj}^2)$. The factors σ_{xj}, σ_{yj} are the uncertainties of the tangential velocities, and σ_{zj} is ones of the radial velocity, which corresponds to the spectral velocity resolution of 0.18 km s^{-1}. Each velocity for W75 N and Cep A was derived to be $V_{\rm rot} = 1.3 \pm 0.7$, $V_{\rm exp} = 0.1 \pm 0.6$, $V_{\rm sys} = 5.8 \pm 0.8$ km s^{-1}, and $V_{\rm rot} = 1.0 \pm 1.0$, $V_{\rm exp} = -2.5 \pm 1.1$, $V_{\rm sys} = -4.8 \pm 0.8$ km s^{-1}, respectively. The rotation velocity for W75 N was smaller than that estimated from the p-v diagram ~3 km s^{-1} using the radius of the ellipse. This difference might be caused by high inclination of the disk ~80°. For the methanol masers in Cep A, the expansion velocity was the negative value showing an infall kinematics caused by the accretion from the disk. This is the first result of detecting infall phenomenon as internal proper motions.

We need to evaluate whether the infalling pressure can exceed the radiation pressure from the exciting star. The momentum rate of the radiation pressure from the exciting star is defined as follows: $\dot{\Pi}_{\rm rd} = (L_* \tau)/(4\pi c)$ assumed that the star isotropically radiates, where L_* is the luminosity of the star, τ the average optical depth of the stellar photon, and c the speed of light ($= 2.998 \times 10^5$ km s^{-1}). Taking $L_* = 1.3 \times 10^4\ L_\odot$, the momentum rate of the radiation pressure was derived to be $\dot{\Pi}_{\rm rd} = 2.1 \times 10^{-5} \cdot \tau\ M_\odot$ yr^{-1} km s^{-1}. The upper limit of the optical depth $\tau \simeq 10$ in a HMSFR ([99]Lamers & Cassinelli

1999) makes the radiation pressure $\sim 10^{-4}$ $M_{\odot}$ yr^{-1} km s^{-1} at maximum. On the other hand, assumed that the accretion occurs from the disk plane, the momentum rate in the infall can be derived with the equation $\dot{\Pi}_{\rm if} = 2\pi r^2 \cdot \rho \cdot V_{\rm inf}^2$, where r is the distance from the star, ρ the mass density in the infall, and $V_{\rm inf}$ its velocity. The factor ρ is related to the number density of the gas $n_{\rm H_2}$. Taking $V_{\rm inf} = 2.5$ km s^{-1} and $r = 719$ AU, the gas density at the masing site is needed to be larger than 10^7 cm^{-3} to exceed the momentum rate of the radiation pressure even if the optical depth is $\tau = 10$. The gas density larger than 10^7 cm^{-3} is covered over the wide range of the gas density for the excitation of the 6.7 GHz methanol masers predicted by [34]Cragg et al. (2005), that is 10^6–10^9 cm^{-3}. The infall momentum rate if the gas density is 10^8 cm^{-3}, $\dot{\Pi}_{\rm if} = 2.4\times10^{-3}(n_{\rm H_2}/[10^8 \text{ cm}^{-3}])$ $M_{\odot}$ yr^{-1} km s^{-1}, is consistent with the accretion rate to exceed the radiation pressure predicted by the theoretical model (e.g., [107]McKee & Tan 2002). High-resolution ($\sim$100 mas scale) observations for the high-density tracer, e.g., N_2H line emission with its critical density $\sim 10^7$ cm^{-3}, are needed to be conducted in Cep A-HW2 to verify whether the high density of the gas $\geq 10^7$ cm^{-3} is fulfilled at the masing site.

6.4.2 Expansion or Outflow

(The following description for ON 1 is extracted from the published paper in 2011 [162].)

First of all, it is unlikely that the methanol masers in ON 1 are associated with a disk because of the spatial distribution isolated with each cluster as well as its separated spectral features, the too large enclosed mass estimated by the p-v diagram, and the outward motions in the north-south direction, as mentioned in section 6.1. We discuss the following two possibilities for sites associated with methanol masers in ON 1: (i) an expanding shell, and (ii) a bipolar outflow.

First, are the methanol masers in ON 1 associated with the expanding UC HII region as well as with the hydroxyl masers? As described in section 6.2.1, the methanol masers in ON 1 coincide spatially with the hydroxyl masers. The radial velocity ranges and the internal proper motions of the methanol masers were also quite similar to those of the hydroxyl masers, at least where the two types coincided spatially. [141]Rygl et al. (2010) also detected internal proper motions of the 6.7 GHz methanol masers in ON 1 in the north-south direction with the EVN and suggested that the methanol masers would be located in the molecular gas surrounding the expanding UC HII region.

There are radial velocity differencies between the 6.7 GHz methanol and the 1.665 GHz hydroxyl masers in the cluster I: methanol $V_{\rm lsr}$ from -0.7 to 1.6 km s^{-1}, while hydroxyl $V_{\rm lsr}$ from 2.5 to 6.1 km s^{-1}. In the 1.665 GHz hydroxyl masers, almost spots correspond to left-circular polarization (LCP) emissions (9 in the 12 spots: [59]Fish & Reid 2007). Thus, the difference in the radial velocities could be due to the Zeeman splitting effects in the area around the cluster I. [58]Fish (2007) measured strengthes of megnetic fields around the cluster I by the 6.035 GHz hydroxyl maser, which range from -8.7 to -12.1 mG. If we assume a magnetic field of averaged -10 mG around the cluster I, similar to that seen in the case of the 6.035 GHz hydroxyl maser by [58]Fish (2007), LCP and RCP of the 1.665 GHz maser features would be separated by 5.9 km s^{-1} according to the Zeeman splitting coefficient 0.59 km s^{-1} mG^{-1} at 1.665 GHz ([41]). For the 1.665 GHz hydroxyl maser LCP features at $V_{\rm lsr}$ from 3.1 to 6.1 km s^{-1} in the north cluster, these might have pairs of RCP features at $V_{\rm lsr}$ from -2.8 to 0.2 km s^{-1}. On the other hand, the 6.7 GHz methanol maser indicates Zeeman splitting coefficient 4.9×10^{-5} km s^{-1} mG^{-1} ([180]Vlemmings et al. 2006; [179]Vlemmings 2008), which leading a separation of 4.9×10^{-4} km s^{-1} between LCP and RCP features: essentially no change in the radial velocity. Hence, the suspected radial velocities of the 1.665 GHz hydroxyl RCP features would correspond to those of the 6.7 GHz methanol masers, and the LCP spots of the 1.665 GHz hydroxyl maser would have radial velocities higher than those of the 6.7 GHz methanol maser. Those RCP components would have flux densities weaker than the image sensitivities in [60]Fish et al. (2005) and [59]Fish & Reid (2007).

Second, we present another possibility for the associated sites: the methanol masers in ON 1 might be associated with the $H^{13}CO^+$ and SiO outflows. As mentioned in subsection 5.1.2, the internal proper motions of the methanol masers showed a flow direction similar to the $H^{13}CO^+$ and SiO outflows: the motions were roughly in the north-south direction, away from the reference maser spot. The radial velocities of the methanol masers were shifted with respect to the systemic velocity in the same direction as the $H^{13}CO^+$ and SiO outflows; the northeast and southwest components of both types of masers and of the outflows were blue- and red-shifted, respectively. The difference in the mean velocities of the north and south components of the proper motion, $V_\mathrm{I} - V_\mathrm{II,III}$, was 5.0 km s^{-1}, which was roughly equal to the velocity of the $H^{13}CO^+$ outflow, 4.5 km s^{-1}. These results suggest that the 6.7 GHz methanol masers in ON 1 could have the same kinematics as the $H^{13}CO^+$ and SiO outflows. To confirm whether the maser spots are moving toward the $H^{13}CO^+$ and SiO outflows, the absolute proper motions of the methanol masers in ON 1 must be measured.

We note that the spatial extent of the maser spot distribution was ~30 times smaller than that of the observed $H^{13}CO^+$ outflow, and the velocity gradients of the methanol masers and the $H^{13}CO^+$ line differ. The velocity gradient for the methanol masers was 7.0×10^{-3} km s^{-1} AU^{-1}, more than an order of magnitude steeper than that for the $H^{13}CO^+$ line, 2.1×10^{-4} km s^{-1} AU^{-1}. This difference might arise from the difference in the spatial resolutions (~1000 times) of the observations.

6.5 Methanol Kinematics Versus an Evolutionary Phase of High-mass YSOs

The relation to an evolutionary phase of high-mass YSOs is likely to explain the difference of the kinematics detected in the 6.7 GHz methanol maser: the methanol masers in W75 N and Cep A are associated with the rotating disk and/or with the infall, while the maser in ON 1 is associated with the expanding UC HII region or the molecular outflow. We note the results of the spatial relationship to other probes, as described in section 6.2, to define an evolutionary phase for each source.

It is easy to define that Cep A-HW2 is the earliest evolutionary phase compared to other two sources. The methanol masers associated with Cep A-HW2 superposed on the dust emission detected as the 335 GHz continuum emission, and an UC HII region has not been detected. The dust emission source is obviously in a younger phase than the UC HII region, which is produced by a well-evolved star embedded in the region. We consider the following two reason to define which sources trace earlier phase in ON 1 and W75 N. First, the methanol maser in ON 1 is associated with the UC HII region produced by a well-evolved star, which is probably a star on the main sequence. Second, the radio jet traced by the internal proper motions of the water masers associated with the VLA 1 in W75 N is well-collimated with an OP < 10°. [14]Beuther & Shepherd (2005) suggested that the high-mass YSOs forming the well-collimated outflow or jet are in the earlier evolutionary phase than an UC HII region. The well-collimated outflow or jet are thought to be formed by the interaction from the disk wind. Indeed, there is the rotating disk traced by the methanol and the hydroxyl masers in W75 N. These properties of the associated sites suggest that the W75 N methanol maser appeared earlier than the ON 1 methanol maser in the evolutionary phase of high-mass YSOs.

We conclude about the relation between the methanol maser kinematics and the evolutionary phase of high-mass YSOs as the following time line. First, the elliptical structure and the infall motions detected in the Cep A-HW2 methanol maser are occured at the

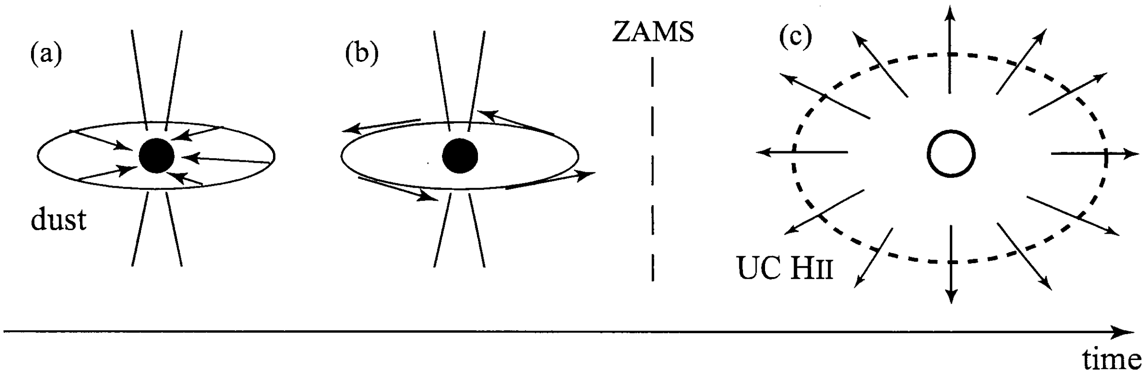

Figure 6-6: A sketch of the relation between the kinematics of the 6.7 GHz methanol masers and evolutionary phases of high-mass YSOs. The time line is evolved to the right direction. The dashed line is the border of the ZAMS (zero-age main sequence). (a) the evolutionary phase in Cep A-HW2. The filled circle represents an exciting YSO, and the blank ellipse surrounding the YSO is a disk. The gas motions on the disk detected as internal proper motions are represented by arrows. The solid lines perpendicular to the disk correspond to an outflow ejected from the YSO. The gray ellipse shows an distribution of a dust emission. (b) the evolutionary phase in W75 N (each expression is same to the figure (a)). (c) the evolutionary phase in ON 1. An exciting star is shown as the open circle, and an UC HII region is shown as the dashed ellipse. The arrows represent an expansion of the UC HII region.

earliest evolutionary phase of the high-mass YSO, which is embedded in the dust emission. The infall motions can be caused by the accretion phenomenon from the rotating disk surrounding the central YSO. Next, the elliptical structure and the simple rotational motions detected in the W75 N methanol maser are seen at the earlier phase than the evolutionary phase forming an UC HII region. The simple rotational motions can be caused by the rotation of the disk without infall/expansion. At this phase, dust emissions surrounding the disk are not detect or too weak to detect. Finally, the separated structure and the outward motions detected in the ON 1 methanol maser are observed at the evolved evolutionary phase that the UC HII region is produced by a well-evolved star, and the accretion disk might be already destroyed. The outward motions trace the expansion of the UC HII region or the molecular outflow. This conclusion is sketched in figure 6-6. [7][8]Bartkiewicz et al. (2009) and (2011) suggested that the elliptical structures detected in ~30% of their methanol maser sources could be observed at the earliest phase of the high-mass YSO evolution, and in some of which sources the water masers could not be detected.

These results suggest not only that the 6.7 GHz methanol masers are useful tool to detect rotational with infall/expansion motions as internal proper motions, but also that the methanol masers trace the two or three evolutionary phases of the high-mass YSOs and the motions depend on the evolutionary phase. The 6.7 GHz methanol masers could be detected in wide-time range of the high-mass YSO evolution from the period for the accretion on the disk to the period that an UC HII region is already produced. Mesuring internal proper motions for more than 100 methanol maser sources by using the VLBI observation technique must provide significat information to figure out the time sequence in the high-mass YSO evolution.

Chapter 7

Concluding and Remarks

We presented spatial distributions with a few mas resolution and internal proper motions of the 6.7 GHz methanol masers in HMSFR ON 1, W75 N, and Cep A, using the JVN. The JVN observations in ON 1, W75 N, and Cep A were conducted at three, two, and three epochs over ~2 years. The phase-referecing technique to obtain the absolute coordinates of the reference maser spot with an accuracy of ~1 mas was used for the methanol masers in ON 1 and Cep A. The spatial distributions of the methanol maser spots observed with the JVN were classified into two types: (i) the separated structure in ON 1 larger than 2000 AU, (ii) the arched of the elliptical structures in W75 N and Cep A with the size ~1000 AU. We draw the following conclusions about the sites associated with the 6.7 GHz methanol masers in each source, including the results of the superposition on other probes and the detected internal proper motions:

1. The 6.7 GHz methanol maser spots in ON 1 were distributed within an area of ~1000 × 2800 AU^2, and were detected as three clusters. Each cluster was separated larger than 2000 AU at maximum as well as separation of its spectral features. The radial velocities of northern and southern clusters were blue- and red-shifted, respectively. The distribution coincided with that of the hydroxyl masers, which surround an UC Hii region. The methanol masers detected with the JVN showed outward motions in roughly the north-south direction. The relative outward velocity is ~5 km s^{-1}, and the motion is also similar to that of the hydroxyl masers. These two masers, therefore, probably trace the same kinematics, that is, the expanding UC Hii region. On the other hand, the distribution and velocity of the methanol masers are also similar to those of the H^{13}CO$^+$ $J = 1{-}0$ and SiO $J = 2{-}1$ outflows. The methanol masers in ON 1 might be associated with these outflows.

2. The 6.7 GHz methanol maser spots in W75 N were distributed within an area of ~ 600 × 2000 AU^2, and the overall distribution represented the arched structure elongated in the north-south direction with linear velocity gradient, which suggested a nearly edge-on disk with a simple rotation. The arched structure fitted by an ellipse with a radius of ~1100 AU was associated with the VLA 1, which is the radio jet along PA of 43°. The methanol maser spots located near the hydroxyl maser spots, where the hydroxyl masers associated with the VLA 1 were thought to trace a simple rotating disk as well as the case of the methanol masers. The slightly offsets between the methanol and the hydroxyl masers estimated to ~200 AU can be explaned by a difference of a distance from an exciting source. The internal proper motions detected with the JVN were fitted by applying the rotating disk with infall/expansion model, and the following velocities were derived: the rotation velocity $V_{\rm rot} = 1.3 \pm 0.7$ km s^{-1}, the expansion velocity $V_{\rm exp} = 0.1 \pm 0.6$ km s^{-1}, and the systemic velocity $V_{\rm sys} = 5.8 \pm 0.8$ km s^{-1}. This result was consistent that the W75 N methanol masers could be associated with the simple rotational disk.

3. The 6.7 GHz methanol maser spots in Cep A-HW2 were clustered as five clusters, corresponding to each spectral feature. The overall distribution formed the arhced structure with the size of ~1400 AU. The arched structure fitted by an ellipse with a radius of ~700 AU coincided with the rotating disks observed with the CH$_3$CN and NH$_3$ line emissions with similarities of the spatial size and the radial velocity range. The elliptical structure was nearly perpendicular to the radio jet in the NE-SW direction. The exciting star represented by the peak of the 43 GHz continuum emission located close to the center of the elliptical structure. The internal proper motions detected with the JVN supported the scenario of the disk. Those motions seen in most of the spots orbited along the elliptical structure. By fitting with the rotating disk with infall/expansion model as well as the case of W75 N, the following velocities were derived: the rotation velocity $V_{\rm rot} = 1.0 \pm 1.0$ km s^{-1}, the infall

> velocity $V_{\rm inf} = 2.5 \pm 1.1$ km s^{-1}, and the systemic velocity $V_{\rm sys} = -4.8 \pm 0.8$ km s^{-1}. This is the first result of detecting infall phenomenon as internal proper motions. It was ambiguity whether the infall can exceed the radiation pressure from the exciting star, because the momentum rate in the infall depends on the mass density related to the gas density. If the gas density is larger than 10^7 cm^{-3}, the infall momentum rate can exceed the momentum rate of the radiation pressure. High-resolution (~100 mas scale) observations for the high-density tracer are needed to verify whether the high density of the gas $\geq 10^7$ cm^{-3} is fulfilled at the masing site.

The difference of the kinematics detected in the 6.7 GHz methanol maser for each source could be explain by considering the relation to an evolutionary phase of high-mass YSOs. It was easy to define that Cep A-HW2 was the earliest evolutionary phase because of the superposition on the dust emission detected at 335 GHz, and non-detection of an UC HII region. The UC HII region is well known to be produced by a well-evolved star embedded in the region. Compared between ON 1 and W75 N, the latter could be likely to appear an earlier phase than the former, because the VLA 1 associated with the methanol masers in W75 N showed the well-collimated outflow with an OP < 10°. The well collimation is thought to be formed by the interaction from the disk wind. We concluded about the relation between the methanol maser kinematics and the evolutionary phase of high-mass YSOs as follows: (i) the elliptical structure and the infall motions like the Cep A-HW2 methanol masers are occured at the earliest phase embedded in the dense gas and dust, (ii) the same structure but the simple rotational motions like the W75 N methanol masers are seen at the second phase at which an UC HII region was not yet formed, (iii) the separated structure and the outward motions like the ON 1 methanol masers are observed at the evolved phase, at which an UC HII region has been formed and the disk might be already destroyed.

We could indicate that the 6.7 GHz methanol masers are useful tool to detect rotational with infall/expansion motions as internal proper motions, and the methanol masers trace the two or three evolutionary phases of the high-mass YSOs and the motions depend on the evolutionary phase. We have planned measuring internal proper motions for more than 50 methanol maser sources to figure out the time sequence in the high-mass YSO evolution in the future.

Acknowledgment

This thesis is based on the collaboration with Prof. Kenta Fujisawa. First of all, I express my appreciation to him. He gave me many useful suggestions, comments, and advices everyday.

I am a Research Fellow DC2 of the Japan Society for the Promotion of Science (JSPS), and this study was supported by a Grant-in-Aid for Scientific Research (No. 21-10375) from the JSPS.

I would like to thank the referees Prof. Junichiro Hara, Prof. Hiroyuki Mashiyama, Prof. Kiyoshi Shiraishi, and Prof. Koji Nozaki for many useful suggestions and comments, which improved this thesis. I am grateful to seniors in the laboratory: Akihiro Sawada, Tsuyoshi Oitate, Naoki Takahashi, Keiichiro Harada, Teppei Tamaki, and Kosuke Suematsu. They encouraged and adviced a lot for data reductions. I deeply thank Dr. Akihiro Doi (the Japan Aerospace Exploration Agency: JAXA), Dr. Mareki Honma (the National Astronomical Observatory of Japan: NAOJ), Dr. Satoko Sawada-Satoh (NAOJ), Dr. Kiyoaki Wajima (Yamaguchi University), and Prof. Hideyuki Kobayashi (NAOJ). They provided me many chances of the discussions about physics and sciences of our studies, and good advices for this observation and data reductions. I also would like to thank Dr. Nanako Mochizuki (JAXA), Dr. Yasuhiro Murata (JAXA), and Prof. Hideo Ogawa (Osaka Prefecture University). They made the high-performance 6.7 GHz receivers at the Usuda 64-m and the each VERA 20-m radio telescope and dedicated management the receivers for high-quality observations. I would like to thank Prof. Osamu Kaburaki (already retired from Yamaguchi University). They gave me many useful comments and assisted me over years. And I express my gratitude to Dr. Simon P. Ellingsen, Dr. Shari L. Breen, Ms. Anita Titmarsh, and Mr. Jay Blanchard, all of who are at the University of Tasmania (UTAS) in Australia. They gave me not only many chances of discussion about my studies, but also the managements of staying at UTAS for two months in 2010.

I am grateful to the KDDI corporation and the staffs in the corporation for their management and maintenance of the Yamaguchi 32-m radio telescope. I also thank the JVN team for assistance and support during the observations. The JVN project is led by NAOJ, which is a branch of the National Institutes of Natural Sciences, Hokkaido University, The University of Tsukuba, Ibaraki University, Gifu University, Osaka Prefecture University, Yamaguchi University, and Kagoshima University, in cooperation with the Geographical Survey Institute, JAXA, and the National Institute of Information and Communications Technology.

Finally, I specially express my most appreciation to my parents, Kuniyoshi and Yasuko, and my sister, Mayuko. They lead me the advance to the doctoral course to achieve my studies, and supported my life since I was born.

Bibliography

[1] Akabane, K., Kaifu, N., & Tahara, H. 1988, Kyoritsu Shuppan Co., Ltd., *Cosmic Radio Astronomy*

[2] Alakoz, A. V., et al. 2005, Astron. Lett., 31, 375

[3] Argon, A. L., Reid, M. J., & Menten, K. M. 2000, ApJS, 129, 159

[4] Barrett, A. H., Schwartz, P. R., & Waters, J. W. 1971, ApJ, 168, L101

[5] Bartkiewicz, A., Szymczak, M., & van Langevelde, H. J. 2005a, A&A, 442, L61

[6] Bartkiewicz, A., Szymczak, M., Cohen, R. J., & Richards, A. M. S. 2005b, MNRAS, 361, 623

[7] Bartkiewicz, A., Szymczak, M., van Langevelde, H. J., Richards, A. M. S., & Pihlström, Y. M. 2009, A&A, 502, 155

[8] Bartkiewicz, A., Szymczak, M., Pihlström, Y. M., van Langevelde, H. J., Brunthaler, A., & Reid, M. J. 2011, A&A, 525, A120

[9] Batrla, W., Matthews, H. E., Menten, K. M., & Walmsley, C. M. 1987, Nature, 326, 49

[10] Beasley, A. J., Gordon, D., Peck, A. B., Petrov, L., MacMillan, D. S., Fomalont, E. B., & Ma, C. 2002, ApJS, 141, 13

[11] Beckwith, S., Evans, N. J., II, Becklin, E. E., & Neugebauer, G. 1976, ApJ, 208, 390

[12] Beltran, M. T., Cesaroni, R., Neri, R., Codella, C., Furuya, R. S., Testi, L., & Olmi, L. 2004, ApJ, 601, L187

[13] Beltran, M. T., Cesaroni, R., Codella, C., Testi, L., Furuya, R. S., & Olmi, L. 2006, Nature, 443, 427

[14] Beuther, H., & Shepherd, D. 2005, Cores to Clusters: *Star Formation with Next Generation Telescopes*, 105

[15] Beuther, H., Walsh, A., Schilke, P., Sridharan, T. K., Menten, K. M., & Wyrowski, F. 2002, A&A, 390, 289

[16] Bloemhof, E. E., Reid, M. J., & Moran, J. M. 1992, ApJ, 397, 500

[17] Brand, J., & Blitz, L. 1993, A&A, 275, 67

[18] Breckenridge, S. M., & Kukolich, S. G. 1995, ApJ, 438, 504

[19] Breen, S. L., et al. 2007, MNRAS, 377, 491

[20] Bronfman, L., Nyman, L.-A., & May, J. 1996, A&AS, 115, 81

[21] Campbell, B. 1984, ApJ, 282, L27

[22] Campbell, B., & Thompson, R. I. 1984, ApJ, 279, 650

[23] Caswell, J. L. 1996a, MNRAS, 279, 79

[24] Caswell, J. L. 1996b, MNRAS, 283, 606

[25] Caswell, J. L., Vaile, R. A., Ellingsen, S. P., & Norris, R. P. 1995b, MNRAS, 274, 1126

[26] Caswell, J. L., Vaile, R. A., Ellingsen, S. P., Whiteoak, J. B., & Norris, R. P. 1995a, MNRAS, 272, 96

[27] Caswell, J. L., et al. 2010, MNRAS, 404, 1029

[28] Cesaroni, R., Hofner, P., Walmsley, C. M., & Churchwell, E. 1998, A&A, 331, 709

[29] Cesaroni, R., Neri, R., Olmi, L., Testi, L., Walmsley, C. M., & Hofner, P. 2005, A&A, 434, 1039

[30] Chini, R., Hoffmeister, V., Kimeswenger, S., Nielbock, M., Numberger, D., Schmidtobreick, L., & Sterzik, M. 2004, Nature, 429, 155

[31] Clarke, C. J., Bonnell, I. A., & Hillenbrand, L. A. 2000, in Mannings, V., Boss, A. P., Russell, S., eds, Protostars and Planets IV. Univ. Arizona Press, Tucson, p.151

[32] Cohen, R. J., et al. 2007, *Triggered Star Formation in a Turbulent ISM*, edited by B. G. Elmegreen & J. Palous, IAU Symp. 237, 403

[33] Cragg, D. M., Sobolev, A. M., & Godfrey, P. D. 2002, MNRAS, 331, 521

[34] Cragg, D. M., Sobolev, A. M., & Godfrey, P. D. 2005, MNRAS, 360, 533

[35] Cragg, D. M., Johns, K. P., Godfrey, P. D., & Brown, R. D. 1992, 259, 203

[36] Cragg, D. M., Sobolev, A. M., Ellingsen, S. P., Caswell, J. L., Godfrey, P. D., Salii, S. V., & Dodson, R. G. 2001, MNRAS, 323, 939

[37] Curiel, S., et al. 2006, ApJ, 638, 878

[38] Cyganowski, C. J., et al. 2008, AJ, 136, 2391

[39] Cyganowski, C. J., Brogan, C. L., Hunter, T. R., & Churchwell, E. 2009, ApJ, 702, 1615

[40] Dame, T. M., et al. 1987, ApJ, 322, 706

[41] Davies, R. D. 1974, *Galactic Radio Astronomy*, IAU Symp. 60, 275

[42] Davis, C. J., Varricatt, W. P., Todd, S. P., & Ramsay Howat, S. K. 2004, A&A, 425, 981

[43] De Buizer, J. M. 2003, MNRAS, 341, 277

[44] Dent, W. R. F., Little, L. T., Kaifu, N., Ohishi, M., & Suzuki, S. 1985, A&A, 146, 375

[45] Dodson, R., Ojha, R., & Ellingsen, S. P. 2004, MNRAS, 351, 779

[46] Downes, D. 1987, *Star forming regions*, edited by Peimbert, M., & Jugaku, J., IAU Symp. 115, 93

[47] Downes, D., Genzel, R., Moran, J. M., Johnston, K. J., Matveenko, L. I., Kogan, L. R., Kostenko, V. I., & Ronnang, B. 1979, A&A, 79, 233

[48] Dreher, J. W., & Welch, W. J. 1981, ApJ, 245, 857

[49] Elitzur, M., Hollenbach, D. J., & McKee, C. F. 1992, ApJ, 394, 221

[50] Ellingsen, S. P. 2005, MNRAS, 359, 1498

[51] Ellingsen, S. P. 2006, ApJ, 638, 241

[52] Ellingsen, S. P. 2007, MNRAS, 377, 571

[53] Ellingsen, S. P., von Bibra, M. L., McCulloch, P. M., Norris, R. P., Deshpande, A. A., & Phillips, C. J. 1996, MNRAS, 280, 378

[54] Ellingsen, S. P., Voronkov, M. A., Cragg, D. M., Sobolev, A. M., Breen, S. L., & Godfrey, P. D. 2007, *Astrophysical Masers and Their Environments*, IAU Symp. 242, 213

[55] Etoka, S., Cohen, R. J., & Gray, M. D. 2005, MNRAS, 360, 1162

[56] Evans, N. J., II, et al. 1981, ApJ, 244, 115

[57] Fey, A. L., et al. 2004, AJ, 127, 3587

[58] Fish, V. L. 2007, ApJ, 669, L81

[59] Fish, V. L., & Reid, M. J. 2007, ApJ, 670, 1159

[60] Fish, V. L., Reid, M. J., Argon, A. L., & Zheng, X.-W. 2005, ApJS, 160, 220

[61] Fomalont, E., Petrov, L., McMillan, D. S., Gordon, D., & Ma, C. 2003, AJ, 126, 2562

[62] Forster, J. R., & Caswell, J. L. 1989, A&A, 213, 339

[63] Fujisawa, K. 2008, in Proc. 9th European VLBI Network Symp. (Bologna), p.75

[64] Furuya, R. S., Cesaroni, R., Codella, C., Testi, L., Bachiller, R., & Tafalla, M. 2002, A&A, 390, L1

[65] Gallimore, J. F., Cool, R. J., Thornley, M. D., & McMullin, J. 2003, ApJ, 586, 306

[66] Gaume, R. A., Goss, W. M., Dickel, H. R., Wilson, T. L., & Johnston, K. J. 1995, ApJ, 438, 776

[67] Gaylard, M. J, & MacLeod, G. C. 1993, MNRAS, 262, 43

[68] Genzel, R., Reid, M. J., Moran, J. M., & Downes, D. 1981a, ApJ, 244, 884

[69] Genzel, R., et al. 1981b, ApJ, 247, 1039

[70] Goddi, C., Moscadelli, L., Sanna, A., Cesaroni, R., & Minire, V. 2007, A&A, 461, 1027

[71] Goedhart, S., Gaylard, M. J., & van der Walt, D. J. 2003, MNRAS, 339, L33

[72] Goedhart, S., Gaylard, M. J., & van der Walt, D. J. 2004, MNRAS, 355, 553

[73] Goedhart, S., Minier, V., Gaylard, M. J., & van der Walt, D. J. 2005, MNRAS, 356, 839

[74] Goedhart, S., Langa, M. C., Gaylard, M. J., & van der Walt, D. J. 2009, MNRAS, 398, 995

[75] Gomez, L., Rodriguez, L. F., Loinard, L., & Lizano, S. 2005, ApJ, 635, 1166

[76] Green, J. A., Richards, A. M. S., Vlemmings, W. H. T., Diamond, P., & Cohen, R. J. 2007, MNRAS, 382, 770

[77] Green, J. A., et al. 2010, MNRAS, 409, 913

[78] Greisen, E. W. 2003, *Information Handling in Astronomy - Historical Vistas*, edited by Andre, H., ASSL, 285, 109

[79] Harvey-Smith, L., & Cohen, R. J. 2006, MNRAS, 371, 1550

[80] Herbst, W., & Racine, R. 1976, AJ, 81, 840

[81] Honma, M., et al. 2005, PASJ, 57, 595

[82] Hughes, V. A., & Wouterloot, J. G. A. 1984, ApJ, 276, 204

[83] Hughes, V. A., Cohen, R. J., & Garrington, S. 1995, MNRAS, 272, 469

[84] Hunter, T. R., Taylor, G. B., Felli, M., & Tofani, G. 1994, A&A, 284, 215

[85] Israel, F. P., & Wootten, H. A. 1983, ApJ, 266, 580

[86] Jiménez-Serra, I., Martín-Pintado, J., Rodríguez-Franco, A., Chandler, C., Comito, C., & Schilke, P. 2007, ApJ, 661, L187

[87] Joint IRAS Science W. G. 1988, Infrared Astronomical Satellite (IRAS) Catalog and Atlas (Washington, D.C.: NASA)[1]

[88] Kameya, O., Morita, K.-I., Kawabe, R., & Ishiguro, M. 1990, ApJ, 355, 562

[89] Klaassen, P. D., & Wilson, C. D. 2007, ApJ, 663, 1092

[90] Kobayashi, H., et al. 2003, ASP Conf. Ser., 306, 367

[91] Kogan, L., & Slysh, V. 1998, ApJ, 497, 800

[92] Kraus, S., et al. 2010, Nature, 466, 339

[93] Krumholz, M. R., Klein, R. I., & McKee, C. F. 2007, ApJ, 665, 478

[94] Kumar, M. S. N., Davis, C. J., & Bachiller, R. 2003, Ap&SS, 287, 191

[95] Kumar, M. S. N., Tafalla, M., & Bachiller, R. 2004, A&A, 426, 195

[96] Kurtz, S., & Franco, J. 2002, Revista Mexicana de Astronomia y Astrofisica Conference Series, 12, 16

---

[1] Joint IRAS Science W.G. 1994, VizieR Online Data Catalog, 2125, 0

[97] Kurtz, S., Churchwell, E., & Wood, D. O. S. 1994, ApJS, 91, 659

[98] Lada, C. J., & Lada, E. A. 2003, ARA&A, 41, 57

[99] Lamers, H. J. G. L. M., & Cassinelli, J. P. 1999, Introduction to Stellar Winds (Cambridge: Cambridge Univ. Press)

[100] Liechti, S., & Wilson, T. L. 1996, A&A, 314, 615

[101] Lonsdale, C. J., et al. 1998, Bulletin of the American Astronomical Society, 30, 1355

[102] Ma, C., et al. 1998, AJ, 116, 516

[103] MacLeod, G. C., & Gaylard, M. J. 1992a, MNRAS, 256, 519

[104] MacLeod, G. C., Gaylard, M. J., & Nicolson, G. 1992b, MNRAS, 254, 1

[105] MacLeod, G. C., Scalise, E. J., Saedt, S., Galt, J. A., & Gaylard, M. J. 1998b, AJ, 116, 1897

[106] MacLeod, G. C., van der Walt, D. J., North, A., Gaylard, M. J., Galt, J. A., & Moriarty-Schieven, G. H. 1998a, AJ, 116, 2936

[107] McKee, C. F., & Tan, J. C. 2002, Nature, 416, 59

[108] McKee, C. F., & Tan, J. C. 2003, ApJ, 585, 850

[109] Menten, K. M. 1991b, ApJ, 380, L75

[110] Menten, K. M. 1991a, Atoms, Ions and Molecules: *New Results in Spectral Line Astrophysics*, ASP Conf. Ser. 16, 119

[111] Menten, K. M., Reid, M. J., Pratap, P., Moran, J. M., & Wilson, T. L. 1992, ApJ, 401, L39

[112] Menten, K. M., Reid, M. J., Moran, J. M., Wilson, T. L., Johnston, K. J., & Batrla, W. 1988, ApJ, 333, L83

[113] Migenes, V., Cohen, R. J., & Brebner, G. C. 1992, MNRAS, 254, 501

[114] Minier, V., Booth, R. S., & Conway, J. E. 1998, A&A, 336, L5

[115] Minier, V., Booth, R. S., & Conway, J. E. 2000, A&A, 362, 1093

[116] Minier, V., Booth, R. S., & Conway, J. E. 2002, A&A, 383, 614

[117] Minier, V., Conway, J. E., & Booth, R. S. 2001a, A&A, 369, 278

[118] Minier, V., Ellingsen, S. P., Norris, R. P., & Booth, R. S. 2003, A&A, 403, 1095

[119] Moscadelli, L., Menten, K. M., Walmsley, C. M., & Reid, M. J. 1999, ApJ, 519, 244

[120] Moscadelli, L., Menten, K. M., Walmsley, C. M., & Reid, M. J. 2002, ApJ, 564, 813

[121] Moscadelli, L., Menten, K. M., Walmsley, C. M., & Reid, M. J. 2003, ApJ, 583, 776

[122] Moscadelli, L., Goddi, C., Cesaroni, R., Beltran, M. T., & Furuya, R. S. 2007, A&A, 472, 867

[123] Moscadelli, L., Reid, M. J., Menten, K. M., Brunthaler, A., Zheng, X. W., & Xu, Y. 2009, ApJ, 693, 406

[124] Müller, H. S. P., Menten, K. M., & Mäder, H. 2004, A&A, 428, 1019

[125] Nagayama, T., Nakagawa, A., Imai, H., Omodaka, T., & Sofue, Y. 2008, PASJ, 60, 183

[126] Nammahachak, S., Asanok, K., Hutawarakorn Kramer, B., Cohen, R. J., Muanwong, O., & Gasiprong, N. 2006, MNRAS, 371, 619

[127] Norris, R. P., Whiteoak, J. B., Caswell, J. L., Wieringa, M. H., & Gough, R. G. 1993, ApJ, 412, 222

[128] Pandian, J. D., Goldsmith, P. F., & Deshpande, A. A. 2007, ApJ, 656, 255

[129] Patel, N. A., et al. 2005, Nature, 437, 109

[130] Pestalozzi, M. R., Minier, V., & Booth, R. S. 2005, A&A, 432, 737

[131] Pestalozzi, M. R., Minier, V., Booth, R., & Conway, J. 2002, Cosmic MASERs: *From Protostars to Blackholes* edited by Migenes, V., and Reid, M. J., IAU Symp. 206, 139

[132] Pestalozzi, M. R., Elitzur, M., Conway, J. E., & Booth, R. S. 2004, ApJ, 603, L113

[133] Pestalozzi, M. R., Minier, V., Motte, F., & Conway, J. E. 2006, A&A, 448, L57

[134] Petrov, L., Kovalev, Y. Y., Fomalont, E., & Gordon, D. 2005, AJ, 129, 1163

[135] Phillips, C. J., Norris, R. P., Ellingsen, S. P., & McCulloch, P. M. 1998, MNRAS, 300, 1131

[136] Plambeck, R. L., & Menten, K. M. 1990, 364, 555

[137] Racine, R. 1968, AJ, 73, 233

[138] Reid, M. J. 2007, *Astrophysical Masers and Their Environments*, IAU Symp. 242, 522

[139] Rodriguez, L. F., Poveda, A., Lizano, S., & Allen, C. 2005, ApJ, 627, L65

[140] Rodríguez, L. F., Garay, G., Curiel, S., Ramírez., S., Torrelles, J. M., Gómez, Y., & Velázquez, A. 1994, ApJ, 430, L65

[141] Rygl, K. L. J., Brunthaler, A., Reid, M. J., Menten, K. M., van Langevelde, H. J., & Xu, Y. 2010, A&A, 511, A2

[142] Sanna, A., Moscadelli, L., Cesaroni, R., Tarchi, A., Furuya, R. S., & Goddi, C. 2010a, A&A, 517, A71

[143] Sanna, A., Moscadelli, L., Cesaroni, R., Tarchi, A., Furuya, R. S., & Goddi, C. 2010b, A&A, 517, A78

[144] Schneider, N., et al. 2006, A&A, 458, 855

[145] Schutte, A., van der Walt, D., Gaylard, M., & MacLeod, G. 1993, MNRAS, 261, 783

[146] Shepherd, M. C. 1997, *Astronomical Data Analysis Software and Systems VI*, ASP Conf. Ser. 125, 77

[147] Shepherd, D. S., Testi, L., & Stark, D. P. 2003, ApJ, 584, 882

[148] Shepherd, D. S., Kurtz, S. E., & Testi, L. 2004, ApJ, 601, 952

[149] Shibata, K. M., Kameno, S., Inoue, M., & Kobayashi, H. 1998, IAU Colloq. 164: *Radio Emission from Galactic and Extragalactic Compact Sources*, ASP Conf. Ser. 144, 413

[150] Shu, F. H., & Adams, F. C. 1987, *Circumstellar matter*, edited by Dordrecht, D., IAU Symp. 122, 7

[151] Shu, F. H., Adams, F. C., & Lizano, S. 1987, Annual Review A&A, 25, 23

[152] Slysh, V. I., Alakoz, A. V, & Migenes, V. 2010, MNRAS, 404, 1121

[153] Slysh, V. I., Val'tts, I. E., Kalenskii, S. V., Voronkov, M. A., Palagi, F., Tofani, G., & Catarzi, M. 1999, A&AS, 134, 115

[154] Slysh, V. I., et al. 2002, ApJ, 564, 317

[155] Sobolev, A. M., Cragg, D. M., & Godfrey, P. D. 1997, MNRAS, 288, L39

[156] Stier, M. T., et al. 1984, ApJ, 283, 573

[157] Su, Y.-N., Liu, S.-Y., & Lim, J. 2009, ApJ, 698, 1981

[158] Su, Y. N., et al. 2004, ApJ, 616, L39

[159] Sun, Y., & Gao, Y. 2009, MNRAS, 392, 170

[160] Sugiyama, K., Fujisawa, K., Doi, A., Honma, M., Kobayashi, H., Bushimata, T., Mochizuki, N., & Murata, Y. 2008a, PASJ, 60, 23

[161] Sugiyama, K., Fujisawa, K., Doi, A., Honma, M., Isono, Y., Kobayashi, H., Mochizuki, N., & Murata, Y. 2008b, PASJ, 60, 1001

[162] Sugiyama, K. et al. 2011(accepted), 63, in prep

[163] Surcis, G., Vlemmings, W. H. T., Dodson, R., & van Langevelde, H. J. 2009, A&A, 506, 757

[164] Sutton, E. C., Sobolev, A. M., Ellingsen, S. P., Cragg, D. M., Mehringer, D. M., Ostrovskii, A. B., & Godfrey, P. D. 2001, ApJ, 554, 173

[165] Szymczak, M., Hrynek, G., & Kus, A. J. 2000, A&A, 143, 269

[166] Szymczak, M., Kus, A. J., Hrynek, G., Kepa, A., & Pazderski, E. 2002, A&A, 392, 277

[167] Torrelles, J. M., Gómez, J. F., Rodríguez, L. F., Curiel, S., Ho, P. T. P., & Garay, G. 1996, ApJ, 457, L107

[168] Torrelles, J. M., Gómez, J. F., Rodríguez, L. F., Ho, P. T. P., Curiel, S., & Vázquez, R. 1997, ApJ, 489, 744

[169] Torrelles, J. M., Patel, N. A., Curiel, S., Ho, P. T. P., Garay, G., & Rodríguez, L. F. 2007, ApJ, 666, L37

[170] Torrelles, J. M., Gómez, J. F., Garay, G., Rodríguez, L. F., Curiel, S., Cohen, R. J., & Ho, P. T. P. 1998, ApJ, 509, 262

[171] Torrelles, J. M., et al. 2003, ApJ, 598, L115

[172] Torstensson, K. J. E., van Langevelde, H. J., Vlemmings, W. H. T., & Bourke, S. 2010, arXiv:1010.4191

[173] Turner, B. E. 1984, Vistas in Astronomy, 27, 303

[174] Turner, J. L., & Welch, W. J. 1984, ApJ, 287, L81

[175] Uscanga, L., et al. 2008, MNRAS, 390, 1127

[176] van der Walt, D. J., Gaylard, M. J., & MacLeod, G. C. 1995, A&AS, 110, 81

[177] van der Walt, D. J., Retief, S. J. P., Gaylard, M. J., & MacLeod, G. C. 1996, MNRAS, 282, 1085

[178] van der Tak, F. F. S., van Dishoeck, E. F., Evans, N. J., II, & Blake, G. A. 2000, ApJ, 537, 283

[179] Vlemmings, W. H. T. 2008, A&A, 484, 773

[180] Vlemmings, W. H. T., Harvey-Smith, L., & Cohen, R. J. 2006, MNRAS, 371, L26

[181] Vlemmings, W. H. T., Surcis, G., Torstensson, K. J. E., & van Langevelde, H. J. 2010, MNRAS, 404, 134

[182] Voronkov, M. A., Slysh, V. I., Palagi, F., & Tofani, G. 2002, in Proc. 6th European VLBI Network Symposium, 213

[183] Voronkov, M. A., Sobolev, A. M., Ellingsen, S. P., & Ostrovskii, A. B. 2005, MNRAS, 362, 995

[184] Walsh, A. J., Burton, M. G., Hyland, A. R., & Robinson, G. 1998, MNRAS, 301, 640

[185] Walsh, A. J., Hylard, A. R., Robinson, G., & Burton, M. G. 1997, MNRAS, 291, 261

[186] Willner, S. P. 1976, ApJ, 206, 728

[187] Wilson, W. J., & Barrett, A. H. 1972, A&A, 17, 385

[188] Wood, D. O. S., & Churchwell, E. 1989, ApJ, 340, 265

[189] Xu, Y., Reid, M. J., Zheng, X. W., & Menten, K. M. 2006, Science, 311, 54

[190] Xu, Y., Li, J. J., Hachisuka, K., Pandian, J. D., Menten, K. M., & Henkel, C. 2008, A&A, 485, 729

[191] York, H. W., & Sonnhalter, C. 2002, ApJ, 569, 846

[192] Zhang, B., Zheng, X. W., Reid, M. J., Menten, K. M., Xu, Y., Moscadelli, L., & Brunthaler, A. 2009, ApJ, 693, 419

[193] Zheng, X. W., Ho, P. T. P., Reid, M. J., & Schneps, M. H. 1985, ApJ, 293, 522

[194] Zinnecker, H., & Yorke, H. W. 2007, ARA&A, 45, 481

[195] the VERA home-page about *System & Stations*, http://veraserver.mtk.nao.ac.jp/system/index-e.html

Appendix A

Maser

The normal line emissions at radio frequencies are very weak caused by spontaneous radiation by collision between molecules. In interstellar space, however, inverted population is often achieved by collision of molecules or/and external infrared radiation from background sources. In the situation, the population number in the upper quantum level is superior to that in the lower level. The phenomenon that the particles in the upper level cascade to the lower level by the background radiation is a trigger of a very strong stimulated emission. The stimulated emission is called as the Microwave Amplification by Stimulated Emission of Radiation, that is maser. Since the hydroxyl maser was dicoverd in 1965 as the interstellar maser for the first time, many masers have been detected from various molecules: H_2O, SiO, CH_3OH, NH_3, and H_2CO. These maser emissions were detected at around both YSOs and evolved stars.

The maser can be described using a simple quantum model showing three levels, as shown in figure 1-1. The following description is refered from the book "Cosmic Radio Astronomy" authored by [1]Akabane et al. (1988). The first and second level occur for the maser emission, and the third level is needed to achieve the inverted population as a role of reservoir. The equilibrium between the first and second level is expressed as follows:

$$N_2(C_{21} + M_{21} + P_{21} + A_{21}) = N_1(C_{12} + M_{12} + P_{12}) \tag{1-1}$$

where N_1, N_2 are the number density of the particles staying at each level, C_{ij} the probability of the collisional transion, A_{21} the Einstein A coefficient, B_{21}, B_{12} the Einstein B coefficient for stimulated emission and absorption, respectively, and P_{ij} is the transition related to the reservoir in the third level. The factor $M_{ij} \equiv B_{ij} I \Omega_{\mathrm{m}}/4\pi$ is the probability of the stimulated emission and the absorption, where Ω_{m} is the solid angle of a background radiation. A pumping up to the level 3 has a key role to make the inverted population, where the pumping up assumed to be able to be achived by either the infrared radiation or the collision in this section. The Einstein A coefficient shows a constant value for each molecule and atom. For example, for the transition seen in CH_3OH molecule at 6.7 GHz the A coefficient is 6.5 $\times 10^{-10}$ sec^{-1}, and for the transition in H_2O, OH (ground-state), and SiO ($J = 1 \rightarrow 0$) the A coefficient are 1.9×10^{-9}, $\sim 10^{-11}$, 3.0×10^{-6} sec^{-1}, respectively. Therefore, the A coefficient can be ignored if the gas density n_{H_2}, or/and the gas temperature, or/and the intensity at radio frequency is much large conditions. The following condition $C_{12} \simeq C_{21} = C$ can be achieved. In this case, the product of the number density of the particles is expressed as follows:

$$\frac{N_2}{N_1} = \frac{P_{12} + M + C}{P_{21} + M + C} \tag{1-2}$$

where $M = M_{12} = M_{21}$. The inverted population including all of effects is expressed as

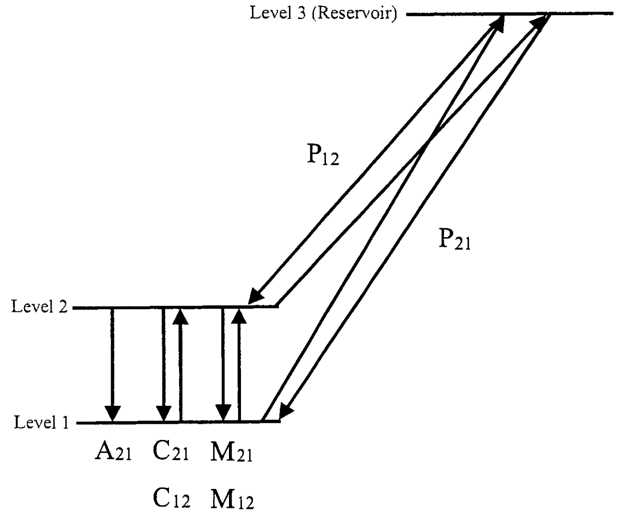

Figure 1-1: A maser model using a simple three quantum levels.

follows assumed:

$$\Delta N = N_2 - N_1 = \frac{\Delta N_0}{1 + \frac{2(C+M)}{P}} \tag{1-3}$$

where $P = P_{12} + P_{21}$, ΔN_0 is the ΔN for $M = C = 0$. We have to consider a radio propagation to the direction of z. The equation of the propagation is expressed as follows by an integration of the radiative transfer equation over all of frequencies:

$$\frac{dI}{dz} = \frac{h\nu}{4\pi\Delta\nu}\Big((N_2 - N_1)BI + N_2 A_{21}\Big) \quad . \tag{1-4}$$

By substituting the equation (1-3) to the equation (1-4), the following expression is described:

$$\frac{dI}{dz} = \frac{\alpha_0 I}{1 + \frac{I}{I_\mathrm{s}}} + \epsilon \quad . \tag{1-5}$$

The factor α_0, I_s, and ϵ are expressed as follows:

$$\begin{cases} \alpha_0 \equiv \frac{h\nu B}{4\pi\Delta\nu} \frac{\Delta N_0}{1+\frac{2C}{P}} \\ I_\mathrm{s} \equiv \frac{1+\frac{2C}{P}}{\frac{B\Omega_\mathrm{m}}{2\pi P}} \\ \epsilon \equiv \frac{h\nu}{4\pi\Delta\nu} N_2 A_{21} \end{cases} \quad .$$

The first term in the equation (1-5) corresponds to the stimulated emission by the background radiation (its intensity I). We note that α_0 is the coefficient of the reverse absorption, and I_s is the intensity at the situation that the maser is saturated. If $I > I_\mathrm{s}$ is made, the situation is called as the maser saturation. In this situation, the stimulated emission affects the population between the quantum levels.

When the maser is unsaturated under the condition $I < I_\mathrm{s}$, its intensity is expressed as follows:

$$I = I_0 e^{\alpha_0 z} + \frac{\epsilon}{\alpha_0}(e^{\alpha_0 z} - 1) \quad . \tag{1-6}$$

The intensity increases in propotion to the path length z with an exponential function, $e^{\alpha_0 z}$, where $\alpha_0 z$ is the gain of unsaturation. The medium for amplification of the unsaturate maser is itself of the inverted population, and the level population depends on proper parameters of the pumping mechanism. The exponential increase of the maser intensity is caused by the cascade transition with the stimulated emission. Once the inverted population starts to be broke up by its maser phenomenon, the maser starts to be saturated under the condition $I > I_\mathrm{s}$. The saturation leads the following relation:

$$\frac{dI}{dz} = \alpha_0 I_\mathrm{s} + \epsilon = constant \quad , \tag{1-7}$$

$$I = I_0 + (\alpha_0 I_\mathrm{s} + \epsilon) z \quad . \tag{1-8}$$

The intensity of the saturated maser is in propotion to the factor $\alpha_0 z$, and has the linearly relation to the path length z.

Appendix B

Characteristics of the 6.7 GHz Methanol Maser

B.1 Variation of Flux Densities

The methanol maser detected at 6.7 GHz is well known to show some variation of its flux densities. [26]Caswell et al. (1995a) conducted the target survey of the methanol masers toward the source sample associated with the hydroxyl masers in the southern hemisphere. The authors detected the methanol masers in 245 sources, and some flux variations with a few months period were observed in 77% sources of 170 sources idetified at five epochs observations. Also, 34% sources in the variation sample showed the flux varition larger than 10%. In the northern hemisphere, [165]Szymczak et al. (2000) conducted the target survey of the methanol masers toward 1411 sources selected in the IRAS point sources. The authors detected the maser in 182 sources, and showed that about 65% of the masers exhibit moderate or strong flux variations on time-scales of about 4 and 8 years. The largest monitoring program for the investigation of the methanol maser flux variation has been conducted using the Hartbeesthoek 26-m radio telescope in the southern hemisphere by [72]Goedhart et al. (2004). The monitoring program was taken toward 54 methanol sources with 1-2 week intervals over 4 years, and the flux variations were classified into six types: non-varying, monotonic increases or decreases, aperiodic, quasi-periodic, and periodic variations. The periodic variations were seen especially in the methanol masers of G 9.62+0.20E with 246 days period, which was the first result of periodic variations associated with high-mass star formation (shown in figure 2-1). It was noted that the periodic variations were synchronized with all of spectral features. The maser spots corresponding to the spectral features showed no changes in spatial morphology within the variation period observed at seven epochs VLBI observations.

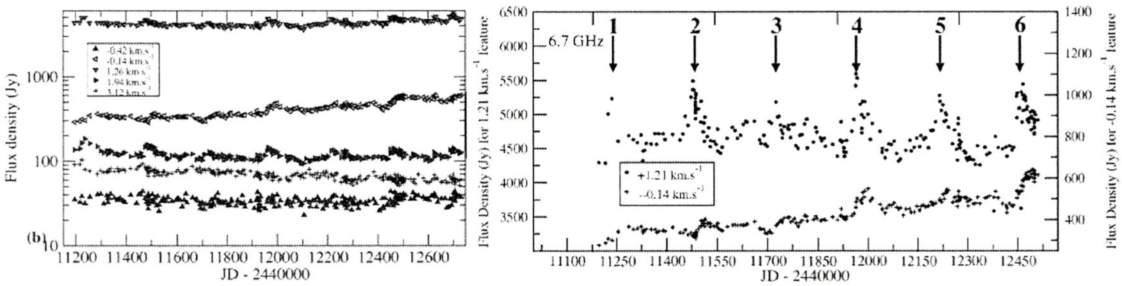

Figure 2-1: Variations of flux densities for the 6.7 GHz methanol masers in HMSFR G 9.62+0.20. Left-panel:extracted from Goedhart et al. (2004); Right-panel:for spectral features with radial velocities of -0.14 and $+1.21$ km s^{-1} (Goedhart et al. 2003). Arrows and numbers indicate cycles of periodic variations of flux densities.

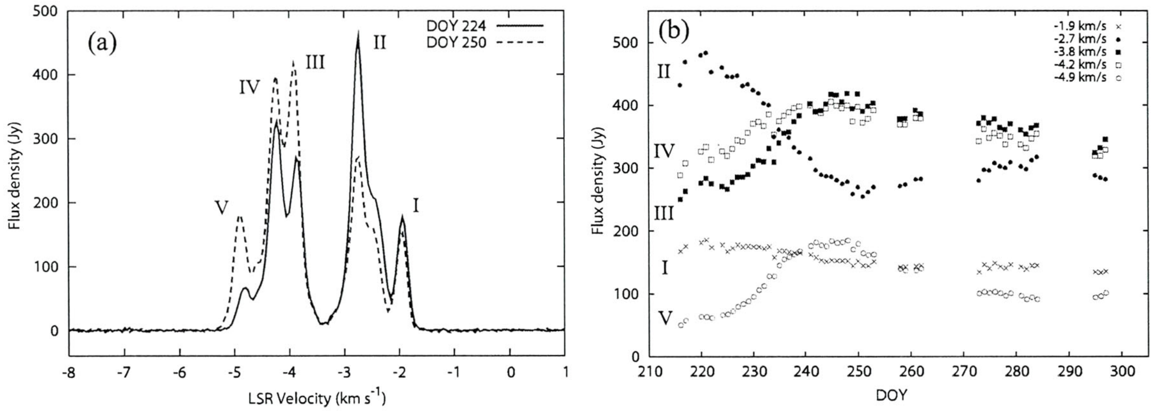

Figure 2-2: The 6.7 GHz methanol maser in Cep A. The labels I, II, III, IV, and V correspond to each spectral feature in each panel. (a) The spectra obtained in the monitoring observations. The solid and dashed line shows the spectra obtained in DOY 224 and 250 observation, respectively. (b) Time variation of each spectral feature.

[161]Sugiyama et al. (2008b) conducted the daily monitoring observations of the 6.7 GHz methanol maser in Cep A using the Yamaguchi 32-m radio telescope for the first time. Five identifed spectral features were grouped into two groupes, redshifted and blueshifted, and the rapid variation within 30 days was detected and the variation was synchronized with each spectral feature. The maser spots corresponding to each spectral feature were separated larger than 100 AU each other, and the authors concluded that the synchronized time variation of the methanol masers can be explained if all of the maser features are excited by infrared radiation from the dust that is heated by a common exciting source with a rapid variability. [74]Goedhart et al. (2009) detected the periodic and synchronized flux variations of the methanol masers in G 12.89+0.49 by daily monitoring. The period of the variation was 29.5 days and the period seemed to be stable over the 110 cycles for about 9 years.

Appendix C

VLBI Channel Maps of Snap-Shot Observations with the JVN

We present the channel-velocity maps of the detected sources with the JVN observations in 2005, as introduced in chapter 2, shown in figure 3-1–3-13. Only total-power spectrum is shown in figure 3-3 for S 255. The maps indicates positions of maser spots relative to that of the reference spot; the size and color of a spot represent its flux density in logarithmic scale and radial velocity, respectively. We describe the results on each individual source below in Right Ascension order.

C.1 W3(OH)

W3(OH) (figure 3-1) is a well-studied star-forming region at a distance of 1.95 ± 0.04 kpc ([189]Xu et al. 2006) containing a hot molecular core (HMC) and an UC Hɪɪ region ([173]Turner & Welch 1984). The central object is thought to be an O9−O7 young star with an estimated mass of $\simeq 30\ M_{\odot}$ ([48]Dreher & Welch 1981). W3(OH) has been imaged with the MERLIN ([55]Etoka et al. 2005; [180]Vlemmings et al. 2006; [79]Harvey & Cohen 2006) and VLBI array at 6.7 GHz ([111]Menten et al. 1992), and with the VLBA at 12.2 GHz ([112]Menten et al. 1988; [119][120][121]Moscadelli et al. 1999, 2002, 2003; [189]Xu et al. 2006).

In our observation, 48 maser spots were detected. The velocity of reference feature is -45.46 km s^{-1} (-45.37 km s^{-1} appeared in [55]Etoka et al. 2005). We detected the maser clusters 1, 5, 6 and 7 defined by [111]Menten et al. (1992), and found a new spot of -46.51 km s^{-1} at 180 mas west from the reference feature. There are 38 spots within a 200 mas area of the cluster 6. The other three clusters locate 0.8″ west, 1.2″ south, and 1.7″ south form the main cluster, respectively.

C.2 Mon R2

The Monoceros R2 (Mon R2, figure 3-2) molecular cloud has a cluster of seven bright infrared sources ([11]Beckwith et al. 1976). The cluster is one of the closest HMSFRs to the solar system at a distance of 0.83 kpc ([137]Racine 1968; [80]Herbst & Racine 1976). The 6.7 GHz methanol maser of Mon R2 has been observed with the Australia Telescope Compact Array (ATCA, [184]Walsh et al. 1998) and with European VLBI Network (EVN, [115][117]Minier et al. 2000, 2001). Although there are several peaks in the total-power spectrum, our VLBI observation detected only one spectral feature around 10.64 km s^{-1} as eight maser spots. This eight spots ($V_{\rm lsr}$ = 10.29 to 11.34) correspond to 'C' defined by [184]Walsh et al. (1998), and also are identified with that five of fourteen spots detected by [115]Minier et al. (2000).

Since this source shows an on-going flux variation, the single-dish spectrum was largely different from that of previous observations. It seems that some spectral features disappeared and some others appeared during 1992 to 2005 ([26]Caswell et al. 1995a; [165]Szymczak et al. 2000).

C.3 S 255

S 255 locating at a distance of 1.59 $^{+0.07}_{-0.06}$ kpc ([141]Rygl et al. 2010) includes one UC HII region G 192.58-0.04 ([97]Kurtz et al. 1994). S 255 has been observed with EVN at 6.7 GHz ([115][117]Minier et al. 2000, 2001), and seven spots were detected with the longest projected baselines of ~30 Mλ. We observed this source and correlated with the coordinates that are used by [115][117]Minier et al. (2000), (2001), but no spot was detected. This source might be resolved out with our baselines. The single-dish spectrum observed by Yamaguchi 32 m is shown in figure 3-3.

C.4 W 33A

W 33A (figure 3-4) is a highly luminous object ($L = 1\times10^5\ L_\odot$, [156]Stier et al. 1984) and coincide a deeply embedded high-mass young stars ([178]van der Tak et al. 2000). The kinematic distance based on CS and $C^{34}S$ observations is 4 kpc ([178]van der Tak et al. 2000). A map consisting eleven maser spots has been obtained with the ATCA ([184]Walsh et al. 1998).

Our observation, the first VLBI for this source, detected 19 maser spots which correspond to 'F', 'G', and 'K' defined by the ATCA observation. The total-power spectrum having several peaks, but weak spectral peaks were not detected in the VLBI map. This source consists of two clusters, and each clusters are separated larger than 1000 AU.

C.5 IRAS 18151−1208

IRAS 18151−1208 (figure 3-5) is embedded in a high-density cloud ([20]Bronfman et al. 1996) and thought to be in pre-UC HII phase ([42]Davis et al. 2004). The kinematic distance based on CS line observation is 3.0 kpc ([17]Brand & Blitz 1993). Thirteen maser spots were detected by our observation. This source has been observed with the ATCA ([15]Beuther et al. 2002) and with EVN ([182]Voronkov et al. 2002). A spot of 27.83 km s^{-1} at 137 mas south from the main cluster was newly detected one.

C.6 G 24.78+0.08

G 24.78+0.08 (figure 3-6) is a cluster of high-mass protostars at a distance of 7.7 kpc ([62]Forster & Caswell 1989). A pair of cores associated with a compact bipolar outflow have been detected ([64]Furuya et al. 2002). [12]Beltran et al. (2004) have detected rotating disks associated with high-mass YSOs by observing 1.4 mm continuum and CH_3CN ($J = 12$–11) line emission. This source has been observed with the EVN ([122]Moscadelli et al. 2007). Our observation showed 21 maser spots, and this source consists of three clusters separated larger than 3000 AU.

C.7 G 29.95−0.02

G 29.95−0.02 (figure 3-7) is at a distance of 9 kpc ([188]Wood & Churchwell 1989) and coincides an NH_3 hot core, but is offset by a few arcsec from the continuum peak of a UC HII region ([28]Cesaroni et al. 1998). The methanol masers of G 29.95−0.02 has been observed with the ATCA at 6.7 GHz ([184]Walsh et al. 1998) and with the VLBA at 12.2 GHz ([115][117]Minier et al. 2000, 2001). Our observation at 6.7 GHz provides the first VLBI image for this source, in which fourteen spots were detected. Twelve of which were clustered within 10 mas, the other two spots were isolated $0.76''$ east from the main cluster. These two clusters detected in our map correspond to 'M' and 'G' defined by [184]Walsh et al. (1998), respectively. There are several spectral features between 95 and 105 km s^{-1} in contrast to 12.2 GHz spectrum, most of weak features could not be detected by our VLBI observation.

C.8 IRAS 18556+0136

IRAS 18556+0136 (figure 3-8) is at a distance of $2.19\ ^{+0.24}_{-0.20}$ kpc ([192]Zhang et al. 2009) and associated with a CO outflows ([44]Dent et al. 1985). Our VLBI observation is the first one for this source, and six maser spots were detected. This source consists of two clusters which are separated larger than 5000 AU. Although there are several spectral peaks, most of weak features could not be detected.

C.9 W 48

W 48 (figure 3-9) is a well-known HII region at a distance of $3.27\ ^{+0.56}_{-0.42}$ kpc ([192]Zhang et al. 2009). This source has a bright UC HII region that could be an on-going high-mass star formation ([188]Wood & Churchwell 1989). W 48 has been observed with EVN at 6.7 GHz ([115]Minier et al. 2000) and with the VLBA at 12.2 GHz ([115]Minier et al. 2000). The maser of this source is strong and the spectrum is widespread, 24 spots forming a ring like structure were detected as observed by [115]Minier et al. (2000). A spot of 43.86 km s^{-1} at 34 mas north and 55 mas west from the reference spot was newly detected one by this observation.

C.10 OH 43.8−0.1

OH 43.8−0.1 (figure 3-10) is a star-forming region at a distance of 2.8 ± 0.5 kpc ([81]Honma et al. 2005). This star-forming region coincides with IRAS 19095+0930 which is an UC HII region ([97]Kurtz et al. 1994). This is the first VLBI observation at 6.7 GHz for this source and we detected nine maser spots. A spot of 43.00 km s^{-1} was located at $0.4''$ east and $0.3''$ south from the reference spot.

C.11 ON 1

Onsala 1 (ON 1, figure 3-11) is an UC HII region located in the densest part of the Onsala molecular cloud ([85]Israel & Wootten 1983) at a distance of $2.57\ ^{+0.34}_{-0.27}$ kpc. This source is known to be associated with a HMSFR and IRAS 20081+3122. Our observation is the first VLBI at 6.7 GHz and seven maser spots were detected. The redshifted cluster and blueshifted cluster are separated about 2400 AU from each other. It is surprising that the redshifted cluster corresponds to the narrow ($\sim$0.5 km s^{-1}) spectral maximum with a flux density of 107 Jy, the correlated flux density is only 4.6 Jy. The flux ratio of correlated to total spectrum is 4.3 %. On the other hand, the blueshifted cluster correspond to relatively weak (~20 Jy) and wide spectral peak, while the flux ratio is about 50 %.

C.12 Cep A

Cepheus A (Cep A, figure 3-12) is a CO condensation at a distance of 0.70 ±0.04 kpc ([123]Moscadelli et al. 2009). One of HMSFRs in Cep A is named as CepA-HW 2 ([82]Hughes & Wouterloot 1984). Cep A has been observed at 12.2 GHz with the VLBA ([115][117]Minier et al. 2000, 2001), while our observation is the first VLBI at 6.7 GHz. We found 30 maser spots, 20 of which had $V_{\rm lsr}$ ranging from −1.15 to −3.26 km s^{-1} and the other ten spots had $V_{\rm lsr}$ ranging from −3.61 to −4.67 km s^{-1}. It is notable that spots in the redshifted cluster aligned in the linear structure. The blueshifted cluster is located at 1.34″ east from the redshifted cluster.

C.13 NGC 7538

The NGC 7538 (figure 3-13) is a star forming region at a distance of $2.65\,^{+0.12}_{-0.11}$ kpc ([123]Moscadelli et al. 2009) including at least 11 high luminosity infrared sources (NGC 7538 IRS 1−11), which are probably young high-mass stars ([88]Kameya et al. 1990). The central star has been thought as O6 ([186]Willner 1976; [22]Campbell & Thompson 1984), so the luminosity of the central source is $8.3\times10^4\ L_\odot$ and the mass is $\simeq 30\ M_\odot$. It is known that this object is associated with an UC Hii region that is observed with the VLA ([21]Campbell 1984; [66]Gaume et al. 1995). The methanol maser of NGC 7538 has been observed with the MERLIN ([133]Pestalozzi et al. 2006) and EVN at 6.7 GHz ([114][115][117]Minier et al. 1998, 2000, 2001; [132][133]Pestalozzi et al. 2004, 2006), and with the VLBA at 12.2 GHz ([114][115][117]Minier et al. 1998, 2000, 2001). The distribution of maser spots in our map corresponds to IRS 1 region ([114]Minier et al. 1998). The map is in good agreement with that of [115]Minier et al. (2000). The redshifted cluster spots with $V_{\rm lsr}$ ranging from −56.45 to −55.75 km s^{-1} aligned in the linear structure as well as previous studies ([114]Minier et al. 1998; [132]Pestalozzi et al. 2004). The spectral features of −53.07 km s^{-1} and −48.99 km s^{-1} corresponding to infrared sources IRS 11 and IRS 9 ([133]Pestalozzi et al. 2006), respectively, were not detected.

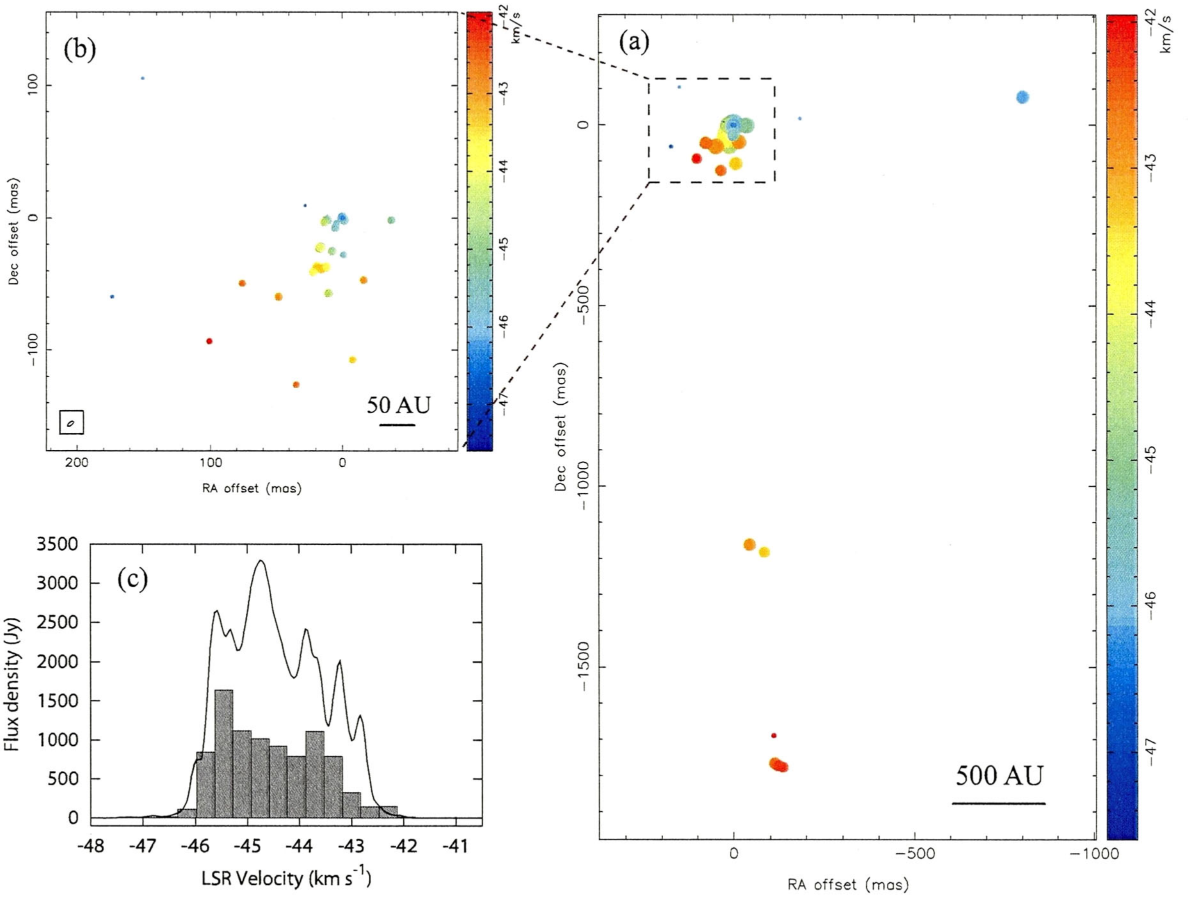

Figure 3-1: W3(OH): (a) wide field view of 0.9″ × 1.8″ channel-velocity map. (b) close-up of the main cluster. (c) CLEANed component spectrum (filled block) and total spectrum (solid curve).

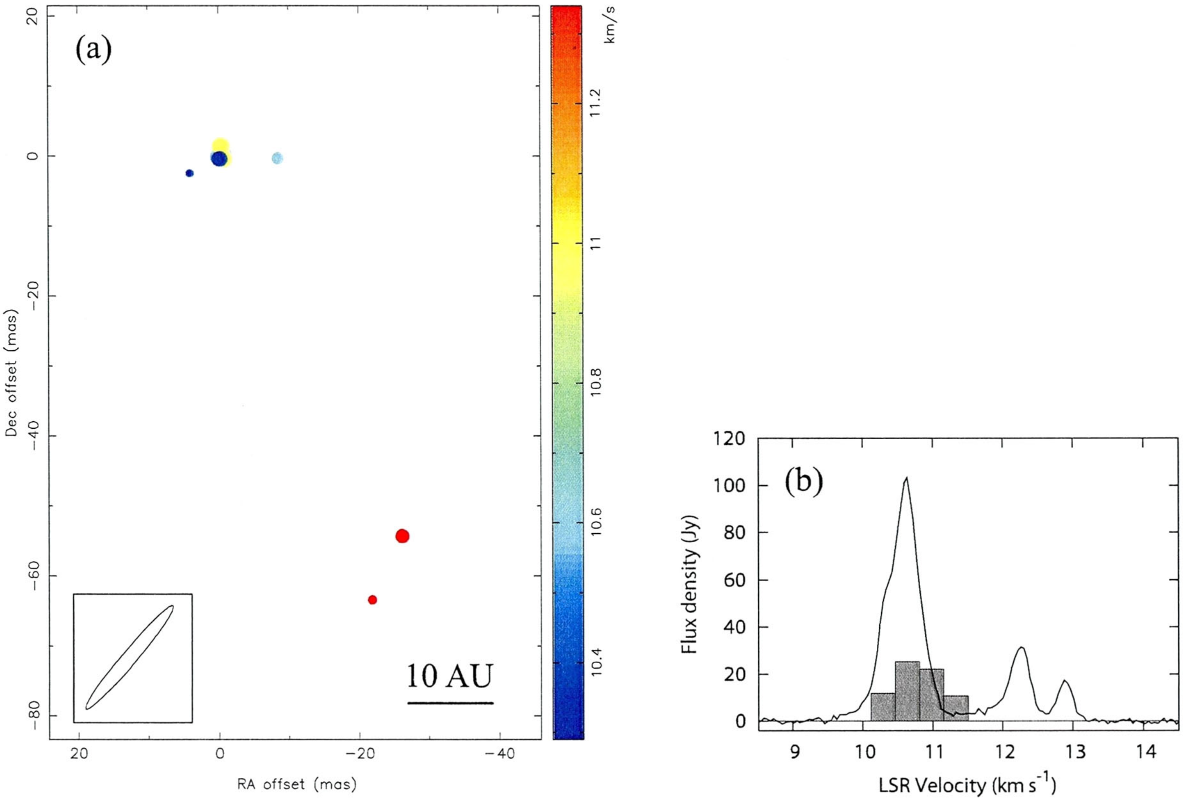

Figure 3-2: Mon R2: (a) channel-velocity map. (b) CLEANed component spectrum (filled block) and total spectrum (solid curve).

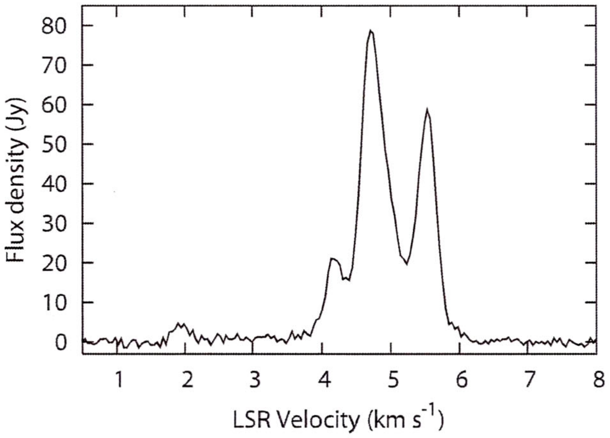

Figure 3-3: The total spectrum of S 255 observed by Yamaguchi 32 m. This source was not detected by our VLBI observation.

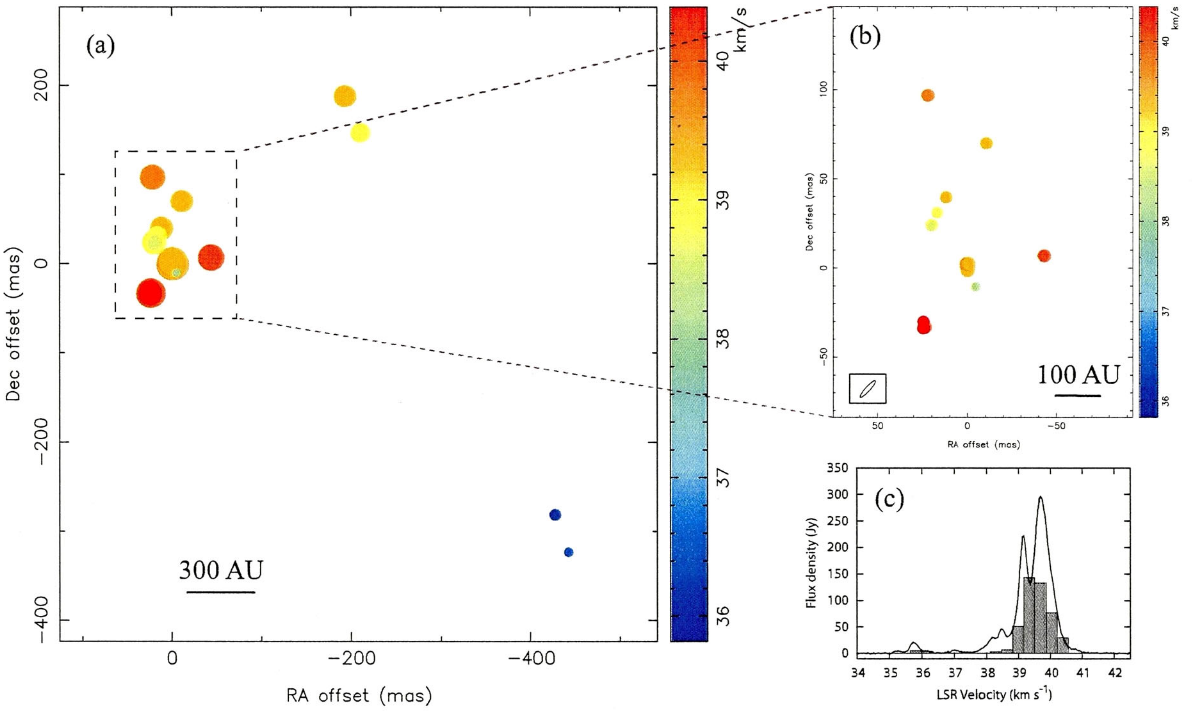

Figure 3-4: W 33A: (a) wide field view of 0.5″ × 0.5″ channel-velocity map. (b) close-up of the main cluster. (c) CLEANed component spectrum (filled block) and total spectrum (solid curve).

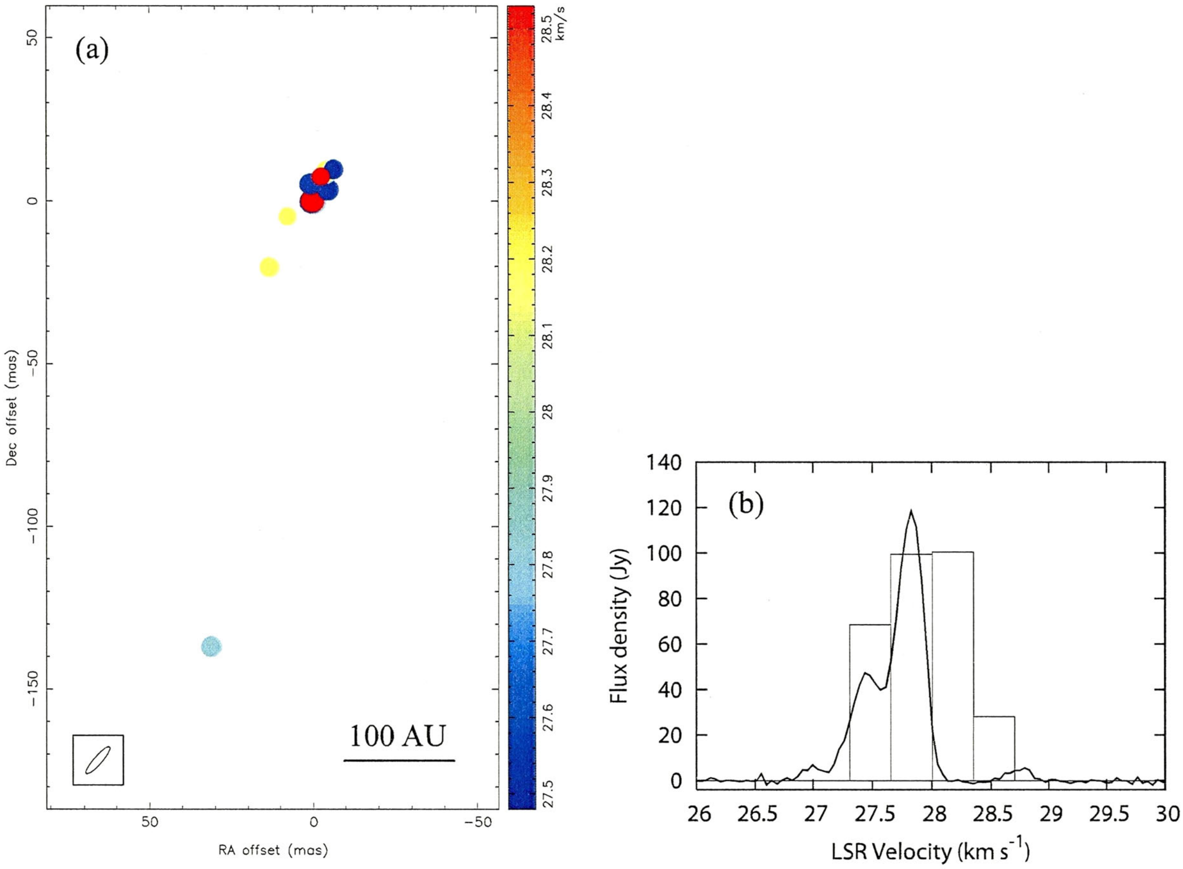

Figure 3-5: IRAS 18151−1208: (a) channel-velocity map. (b) CLEANed component spectrum (blank block) and total spectrum (solid curve).

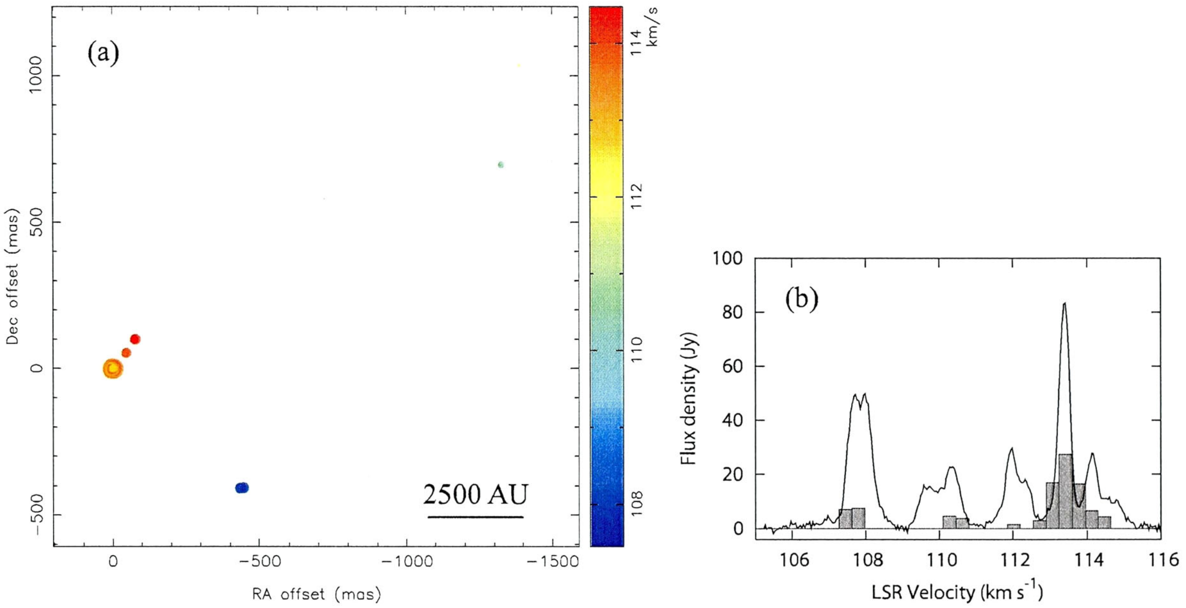

Figure 3-6: G 24.78+0.08: (a) wide field view of 1.4″ × 1.4″ channel-velocity map. (b) CLEANed component spectrum (filled block) and total spectrum (solid curve).

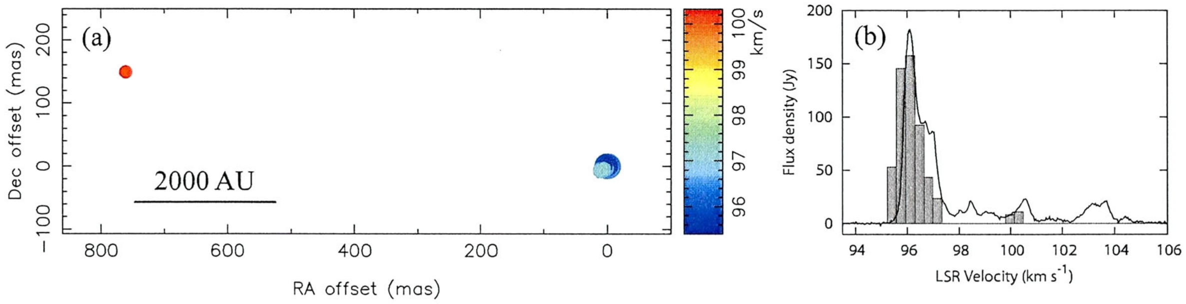

Figure 3-7: G 29.95−0.02: (a) wide field view of 0.76″ × 0.15″ channel-velocity map. (b) CLEANed component spectrum (filled block) and total spectrum (solid curve).

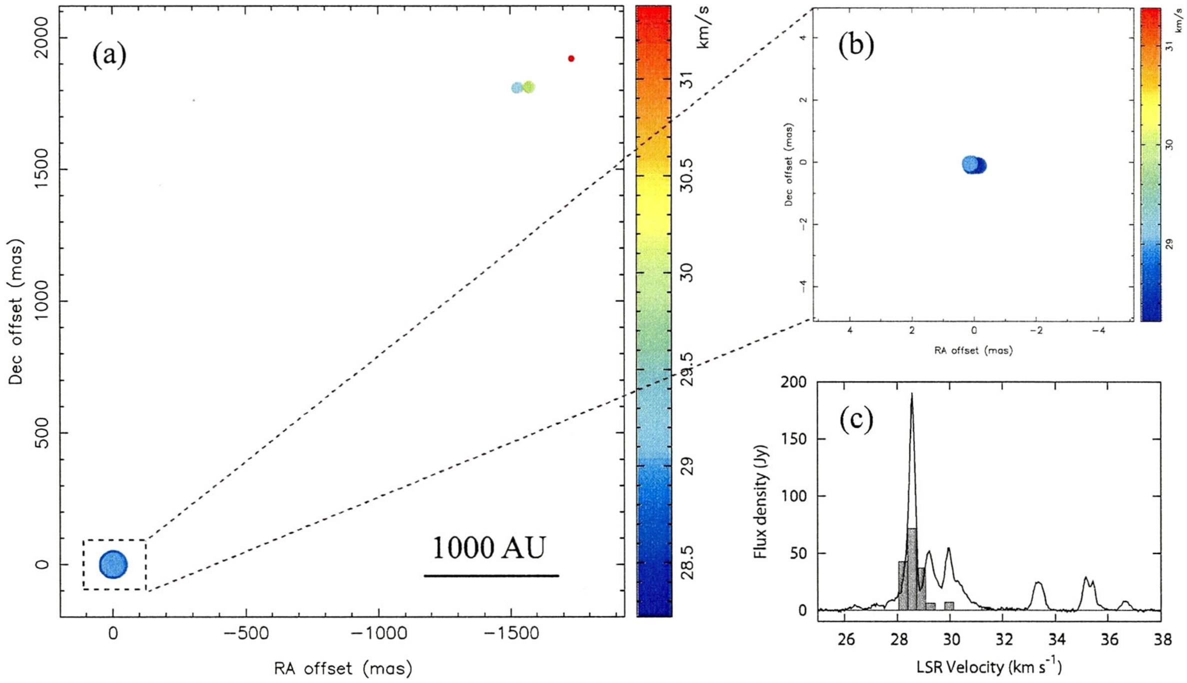

Figure 3-8: IRAS 18556+0136: (a) wide field view of 1.7″ × 1.9″ channel-velocity map. (b) CLEANed component spectrum (filled block) and total spectrum (solid curve).

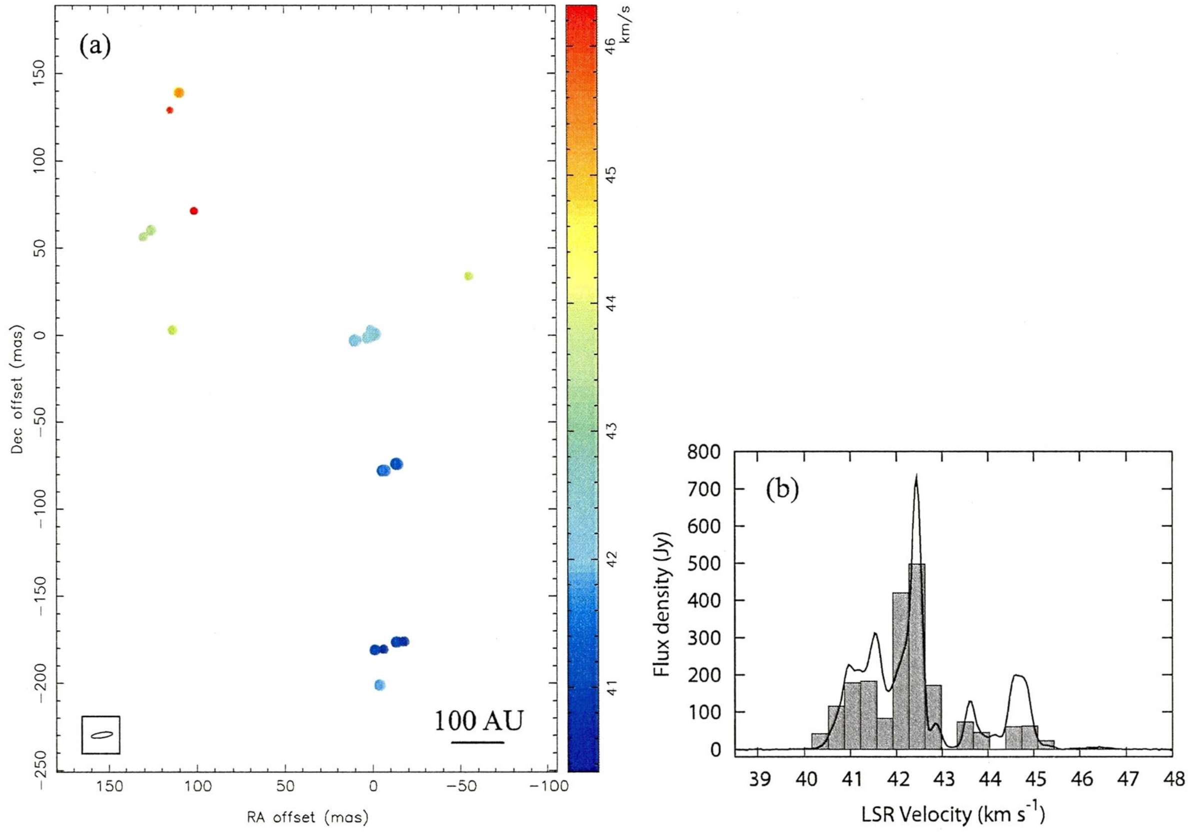

Figure 3-9: W 48: (a) channel-velocity map. (b) CLEANed component spectrum (filled block) and total spectrum (solid curve).

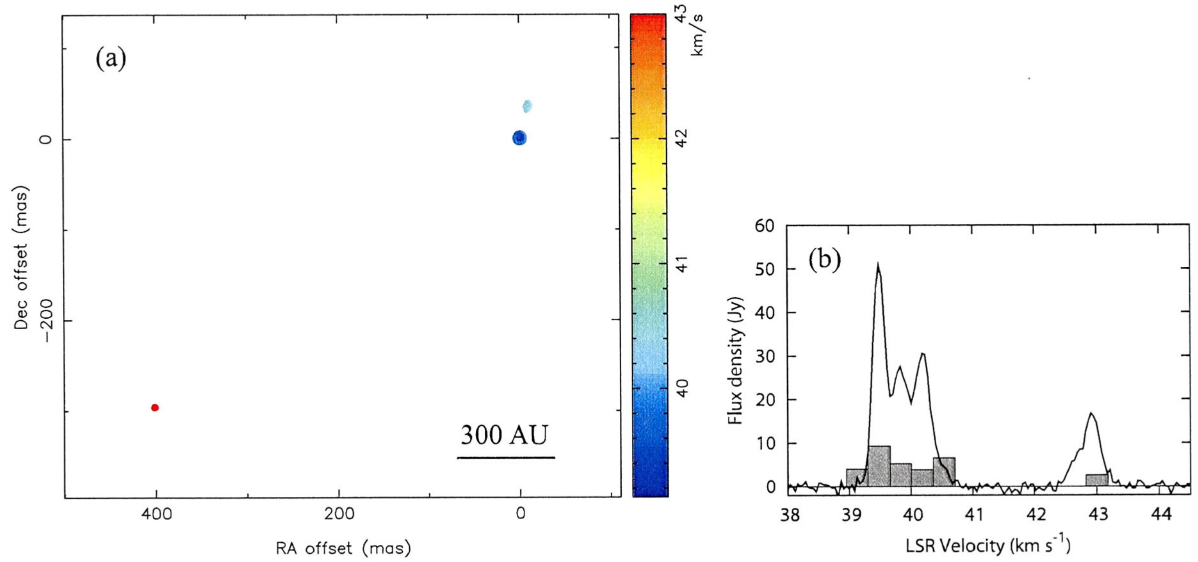

Figure 3-10: OH 43.8−0.1: (a) wide field view of 0.4″ × 0.3″ channel-velocity map. (b) CLEANed component spectrum (filled block) and total spectrum (solid curve).

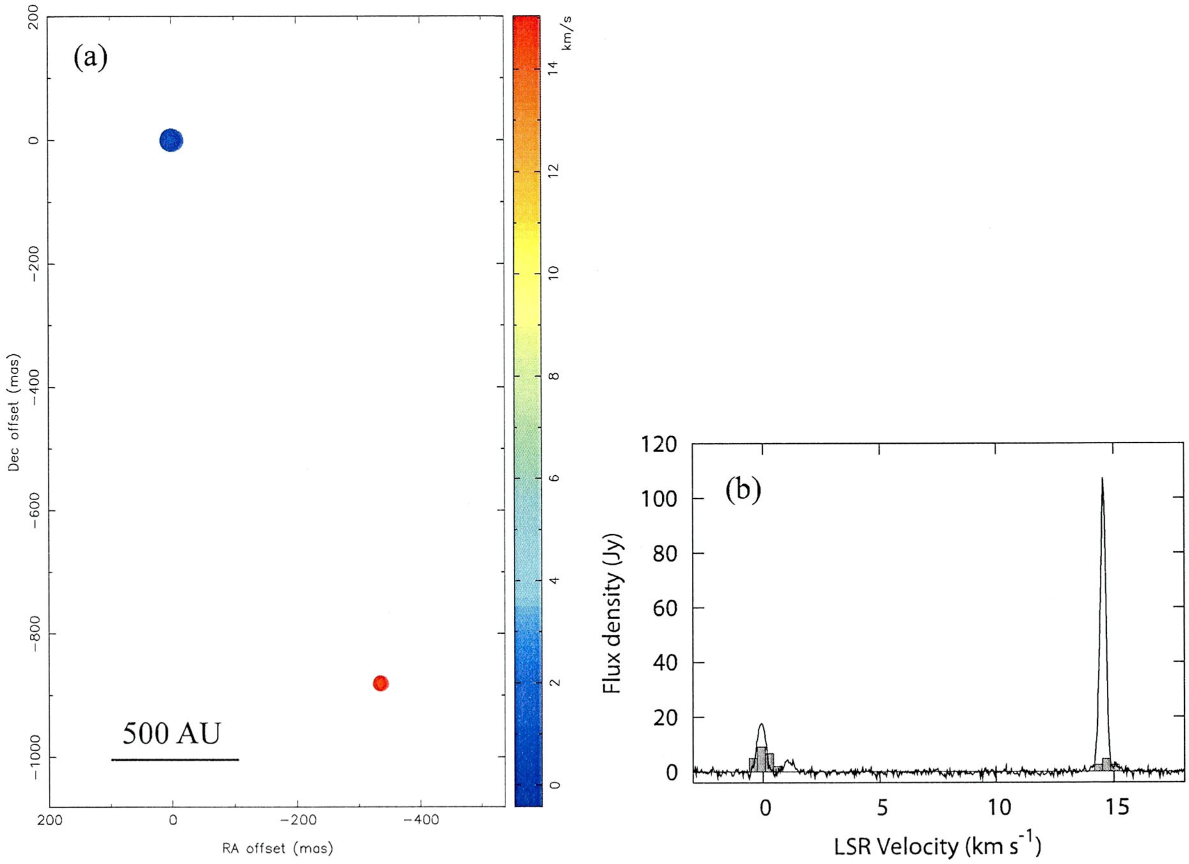

Figure 3-11: ON 1: (a) wide field view of 0.34″ × 0.88″ channel-velocity map. (b) CLEANed component spectrum (filled block) and total spectrum (solid curve).

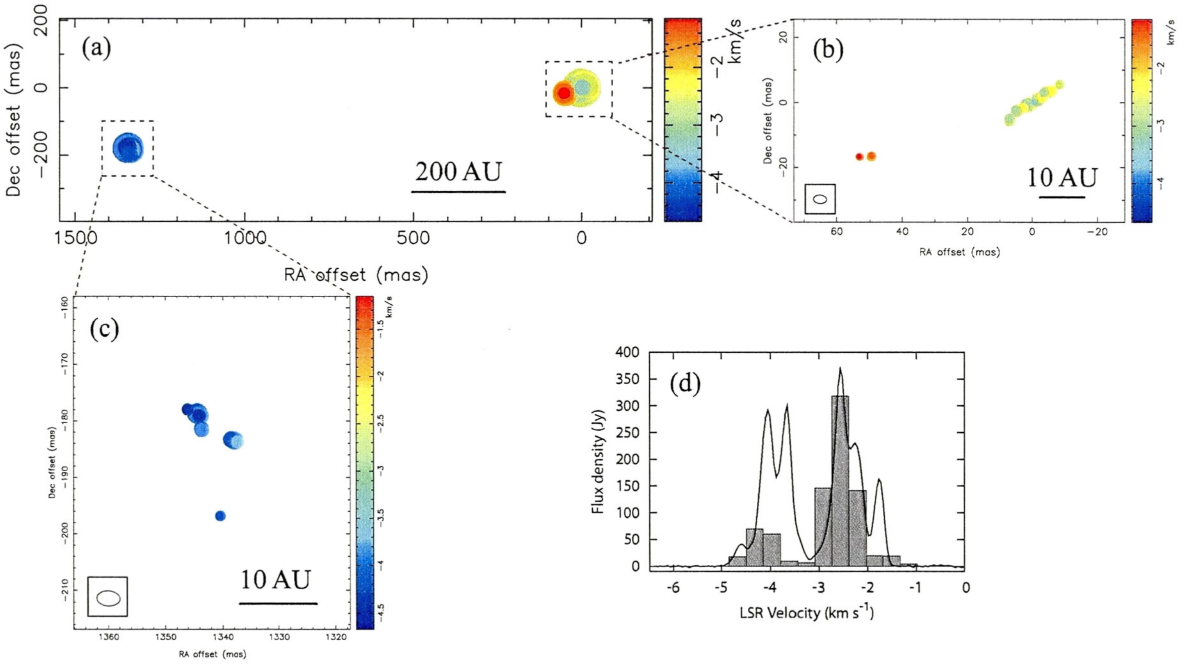

Figure 3-12: Cep A: (a) wide field view of 1.3″ × 0.18″ channel-velocity map. (b) close-up of the redshifted cluster. (c) close-up of the blueshifted cluster. (d) CLEANed component spectrum (filled block) and total spectrum (solid curve).

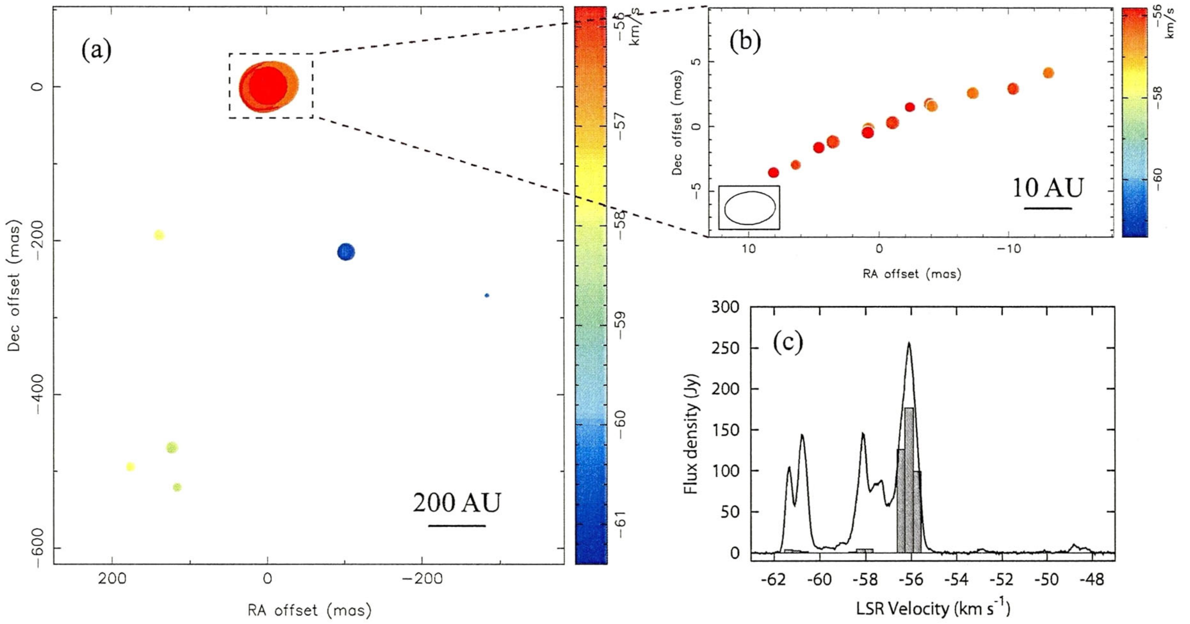

Figure 3-13: NGC 7538: (a) wide field view of 0.5″ × 0.5″ channel-velocity map. (b) close-up of the redshifted cluster. (c) CLEANed component spectrum (filled block) and total spectrum (solid curve).

Appendix D

Least-square Fit for the Rotating Disk Model with Expansion/Infall

The least-square fit using the rotating disk with expansion/infall model, which rotation $V_{\rm rot}$, expansion $V_{\rm exp}$, and systemic velocity $V_{\rm sys}$ are expressed in equation (6-1 – 6-3), is described in this appedix. The disk model was sketched in figure 6-5. The solutions for each velocity are based on the minimisation of the χ^2 function expressed as follows:

$$\chi^2 = \sum_{j=1}^{N} w_j \left((V_{xj} - V_{xj}^{\rm calc})^2 + (V_{yj} - V_{yj}^{\rm calc})^2 + (V_{zj} - V_{zj}^{\rm calc})^2 \right) \tag{4-1}$$

where N is the number of the maser spots that the internal proper motions were detected, V_{xj}, V_{yj} the tangential velocities measured as the internal proper motions for the maser spot identified as ID j, V_{zj} the radial velocity corresponding to $V_{\rm lsr}$, and w_j the weight function expressed as $1/(\sigma_{xj}^2 + \sigma_{yj}^2 + \sigma_{zj}^2)$. The factors σ_{xj}, σ_{yj} are the uncertainties of the tangential velocities, and σ_{zj} is ones of the radial velocity. The minimisation is by partial differentiation for each velocity, that is that $\partial\chi^2/\partial V_{\rm rot}$, $\partial\chi^2/\partial V_{\rm exp}$, and $\partial\chi^2/\partial V_{\rm sys}$ were estimated. These estimations lead the following expressions:

$$\begin{aligned}
V_{\rm rot} &= \frac{A^2 \cdot C + A \cdot B \cdot F - C \cdot D^2 - B \cdot D \cdot F}{A \cdot (A^2 - B^2 - D^2)} \\
V_{\rm exp} &= \frac{A^2 \cdot E - B \cdot C \cdot D - B^2 \cdot E - A \cdot D \cdot F}{A \cdot (A^2 - B^2 - D^2)} \\
V_{\rm sys} &= \frac{A \cdot F + B \cdot C - D \cdot E}{A^2 - B^2 - D^2}
\end{aligned}$$

where the factor A, B, C, D, E, and F are expressed as follows:

$$\begin{aligned}
A &= \sum_{j=1}^{N} w_j \\
B &= \sin i \sum_{j=1}^{N} w_j \cos\theta_j \\
C &= \sum_{j=1}^{N} w_j V_{xj} \sin\theta_j - \cos i \sum_{j=1}^{N} w_j V_{yj} \cos\theta_j - \sin i \sum_{j=1}^{N} w_j V_{zj} \cos\theta_j \\
D &= \sin i \sum_{j=1}^{N} w_j \sin\theta_j \\
E &= \sum_{j=1}^{N} w_j V_{xj} \cos\theta_j + \cos i \sum_{j=1}^{N} w_j V_{yj} \sin\theta_j + \sin i \sum_{j=1}^{N} w_j V_{zj} \sin\theta_j \\
F &= \sum_{j=1}^{N} w_j V_{zj} \quad .
\end{aligned}$$